

AERODYNAMIC OPTIMISATION OF A SMALL-SCALE
WIND TURBINE BLADE FOR LOW WINDSPEED CONDITIONS

Nicolette Arnalda Cencelli

*Thesis presented at the University of Stellenbosch
in partial fulfilment of the requirements for
the degree of*

Master of Science in Mechanical Engineering

Supervisors:

Prof. T.W. von Backström
T.S.A. Denton



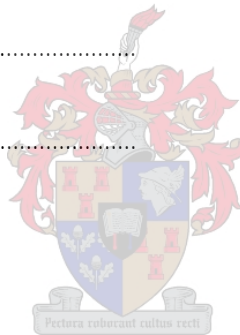
December 2006

DECLARATION

I, the undersigned, hereby declare that the work contained in this thesis is my own original work and that I have not previously in its entirety or in part submitted it at any university for a degree.

Signature:

Date:



ABSTRACT

Wind conditions in South Africa determine the need for a small-scale wind turbine to produce usable power at windspeeds below 7m/s. In this project, a range of windspeeds, within which optimal performance of the wind turbine is expected, was selected. The optimal performance was assessed in terms of the Coefficient of Power (C_p), which rates the turbine blade's ability to extract energy from the available wind stream. The optimisation methods employed allowed a means of tackling the multi-variable problem such that the aerodynamic characteristics of the blade were ideal throughout the windspeed range. The design problem was broken down into a two-dimensional optimisation of the airfoils used at the radial stations, and a three-dimensional optimisation of the geometric features of the wind rotor. By means of blending various standard airfoil profiles, a new profile was created at each radial station. XFOIL was used for the two-dimensional analysis of these airfoils. Three-dimensional optimisation involved representation of the rotor as a simplified model and use of the Blade Element Momentum (BEM) method for analysis. An existing turbine blade, on which the design specifications were modelled, was further used for comparative purposes throughout the project. The resulting blade design offers substantial improvements on the reference design. The application of optimisation methods has successfully aided the creation of a wind turbine blade with consistent peak performance over a range of design points.

OPSOMMING

Windtoestande in Suid-Afrika bepaal die behoefte aan 'n kleinskaal windturbine om bruikbare drywing te voorsien teen windsnelhede onder 7m/s. In hierdie projek is 'n bestek van windsnelhede gekies waarbinne optimale gedrag van die windturbine verwag word. Die optimale vertoning is beoordeel in terme van die Drywingskoëffisiënt (C_p), wat die turbine se vermoë aanslaan om energie uit die beskikbare windstroom te onttrek. Die toegepaste optimeringsmetodes het 'n metode beskikbaar gestel om die multi-veranderlike probleem aan te pak sodat die aerodinamiese eienskappe van die lem ideaal sou wees oor die bestek. Die ontwerpprobleem is verdeel in 'n twee-dimensionele optimering van die lemprofiele by die radiale stasies, en 'n drie-dimensionele optimering van die geometriese kenmerke van die windturbine rotor. Deur verskeie standaard lugdinamiese profiele te vermeng, is 'n nuwe profiel by elke radiale stasie geskep. XFOIL is gebruik vir die twee-dimensionele analise van hierdie lemprofiele. Drie-dimensionele optimering het die voorstelling van die rotor as 'n vereenvoudigde model gebruik, met die lem-element model vir analise. 'n Bestaande turbine lem, waaraan die ontwerp spesifikasies ontleen is, is verder dwarsdeur die projek gebruik vir vergelykende doeleindes. Die resulterende lem ontwerp bied beduidende verbeteringe teenoor die verwysingsontwerp. Die toepassing van optimeringsmetodes het die skepping van 'n windturbinelem met konsekwente piekvertoning oor 'n bestek van ontwerp punte aangehelp.

ACKNOWLEDGEMENTS

To the Lord Jesus who is above all the most faithful and most gracious

Researching a masters' thesis has been likened to navigating through a dark forest...a dark forest with a barely distinguishable pathway, with protruding roots of trees waiting to catch the fumbling foot and pungent swamps of stagnation. Nevertheless, the persistent and determined strive on for the reward of those brief clearings in the wood when the sun shines brightly through the trees and the air smacks of crystal, clear quality. Finally, upon exit of the forest, one realises that it was surely the greatest journey ever made and a part of oneself wants to remain lost within it forever.

I am grateful to Stellenbosch University for my fantastic research experience and especially to Professor Von Backström who has been a fantastic guide. Thank-you so much for your patience and encouragement.

Thank-you to Terence Denton who first suggested this project and whose expertise has been invaluable during the project. Your insight and enthusiasm has been an inspiration. Also, to Dr Harms, thank-you for spreading your passion for engineering to all your students. Many thanks to my family for the late-night phone calls and many prayers. You have been so supportive to this eternal student.

To my beautiful baby Ghia, thank-you for patiently and attentively listening while I was typing away at the last pages of this academic baby of mine...this is for you.

TABLE OF CONTENTS

DECLARATION	i
ABSTRACT	ii
OPSOMMING	iii
ACKNOWLEDGEMENTS	iv
TABLE OF CONTENTS.....	v
LIST OF FIGURES	vii
LIST OF TABLES	x
NOMENCLATURE	xi
1. INTRODUCTION.....	1
1.1 <u>Literature Review</u>	3
1.1.1 Unsteady Aerodynamics Associated with Wind Turbines.....	3
1.1.2 Optimisation within Wind Turbine and Airfoil Design	5
1.1.3 Verification of Wind Turbine Prediction Data	7
2. ROTOR AERODYNAMICS	9
2.1 <u>One Dimensional Momentum Theory</u>	9
2.2 <u>Blade Element Momentum Method</u>	13
2.2.1 Prandtl's Tip-Loss Factor	17
2.2.2 Glauert Correction for High Values of a	18
2.3 <u>Two-dimensional Stacked Design using Xfoil</u>	18
2.3.1 Xfoil Prediction of Transition	19
2.3.2 Xfoil within the Design Process.....	19
3. OPTIMISATION METHODS.....	21
3.1 <u>Gradient-Based Optimisation</u>	21
3.2 <u>Non-gradient Based Optimisation</u>	23
3.3 <u>VisualDOC Software</u>	24
4. DESIGN APPROACH.....	25
4.1 <u>Rotor Design Method</u>	25
4.1.1 Objectives and Constraints.....	27
4.1.2 Design Variables	28
4.2 <u>Profile Design Method</u>	30
4.2.1 Objectives and Constraints	32
4.2.2 Design Variables	33
5. VERIFICATION OF PROGRAM.....	35
5.1 <u>CSIR experimental data</u>	35
5.2 <u>NWU experimental data</u>	37
6. NEW BLADE OPTIMISATION	39
6.1 <u>Profile Optimisation</u>	39

6.1.1	Root profile	40
6.1.2	Mid profile.....	44
6.1.3	Semi profile	49
6.1.4	Tip profile	53
6.1.5	Discussion of Results.....	57
6.2	<u>Rotor Optimisation</u>	59
6.2.1	Weibull Weighted Designs	59
6.2.2	Analysis of Lift-to-Drag Ratios	63
6.2.3	Non-selection Profiles	69
6.3.4	Off-design Analysis.....	70
7.	CONCLUSION	73
7.1	<u>Profile Optimisation</u>	74
7.2	<u>Rotor Optimisation</u>	76
7.3	<u>Optimisation Methodology</u>	78
7.4	<u>Recommendations for Future Work</u>	78
8.	REFERENCES	80

APPENDICES

A.1	<u>Generation of New Airfoils</u>	83
A.2	<u>Base Profiles Geometric Data</u>	86
A.3	<u>Calculations</u>	88
A.3.1	Structural Verification	88
A.3.2	Weibull Wind Distribution	90
A.4	<u>Program Code</u>	91
A.4.1	BEM program	91
A.4.2	XFOIL code	94
A.5	<u>Investigation of Solution Space</u>	96
A.5.1	Pitch angle at root station	96
A.5.2	Pitch angle at mid station.....	98
A.5.3	Pitch angle at semi station.....	99
A.5.4	Pitch angle at tip station	101
A.5.5	Chord length variation	103
A.5.6	Discussion of Results	107

LIST OF FIGURES

- Figure 1.1.1: Meteorological Survey of Southern Africa
- Figure 2.1.1: Schematic of the streamlines past the rotor
- Figure 2.1.2: Circular control volume
- Figure 2.1.3: Alternative control volume
- Figure 2.2.1: The local forces on an airfoil of the blade
- Figure 2.2.2: The inflow velocities at the rotor plane
- Figure 2.2.3: Induced velocities at the rotorplane
- Figure 3.1.1: Solution Space in Gradient Optimisation
- Figure 4.1.1: Weibull weighting distribution
- Figure 4.1.2: Three-dimensional Design Approach
- Figure 4.1.3: Example of XFOIL data file
- Figure 4.1.4: Velocity diagram at a two-dimensional section of the blade
- Figure 4.2.1: Method of integration of L/D ratios
- Figure 4.2.2: Two-dimensional Design Approach
- Figure 5.1.1: C_p plot of analytical data vs. experimental data
- Figure 5.2.1: Analytically determined blade curve map for NWU blade
- Figure 5.2.2: Experimental data vs analytical data for NWU blade
- Figure 6.1.1: The optimised airfoils - top is the root and mid foils, bottom is the semi and tip
- Figure 6.1.2: Foil 1 - mh102
- Figure 6.1.3: Foil 2 - sg6043
- Figure 6.1.4: Foil 3 - ah94w301
- Figure 6.1.5: Foil 4 - fx83w227
- Figure 6.1.6: Foil 5 - rxcamtxt
- Figure 6.1.7: Foil 6 - fx77w270s
- Figure 6.1.8: Foil 7 - Somer's root foil
- Figure 6.1.9: Optimised root profile
- Figure 6.1.10: Lift coefficient vs. angle of attack
- Figure 6.1.11: L/D ratio vs. angle of attack
- Figure 6.1.12: Foil 1 - FX 84-W-175
- Figure 6.1.13: Foil 2 - NACA 4415
- Figure 6.1.14: Foil 3 - LNV 109a
- Figure 6.1.15: Foil 4 - AH 93-W-215
- Figure 6.1.16: Foil 5 - SG 6041
- Figure 6.1.17: Foil 6 - rxcamtxt
- Figure 6.1.18: Optimised mid profile
- Figure 6.1.19: L/D ratio vs. angle of attack

- Figure 6.1.20: Lift coefficient vs. angle of attack
- Figure 6.1.21: Foil 1 - FX 84-W-175
- Figure 6.1.22: Foil 2 - NACA 4415
- Figure 6.1.23: Foil 3 - E 387
- Figure 6.1.24: Foil 4 - AH 93-W-215
- Figure 6.1.25: Foil 5 - SG 6041
- Figure 6.1.26: Optimised semi profile
- Figure 6.1.27: L/D ratio vs. angle of attack
- Figure 6.1.28: Lift coefficient vs. angle of attack
- Figure 6.1.29: Foil 1 - FX 84-W-097
- Figure 6.1.30: Foil 2 - MH 106
- Figure 6.1.31: Foil 3 - NACA 654-421
- Figure 6.1.32: Foil 4 - Somer's root foil
- Figure 6.1.33: Foil 5 - FX 77-W-121
- Figure 6.1.34: Foil 6 - RAF-6D
- Figure 6.1.35: Optimised tip profile
- Figure 6.1.36: L/D ratio vs. angle of attack
- Figure 6.1.37: Lift coefficient vs. angle of attack
- Figure 6.2.1: Results from eight tasks using Weibull-weighting distribution
- Figure 6.2.2: Top five designs compared to CSIR blade
- Figure 6.2.3: Chord distributions of designs A to H, including the CSIR design
- Figure 6.2.4: Pitch distribution of designs A to E, including the CSIR design
- Figure 6.2.5: Lift-to-drag ratios for root station
- Figure 6.2.6: Lift-to-drag ratios for mid station
- Figure 6.2.7: Lift-to-drag ratios for semi station
- Figure 6.2.8: Lift-to-drag ratios for tip station
- Figure 6.2.9: Design B, root station
- Figure 6.2.10: Design H, root station
- Figure 6.2.11: Design B, mid station
- Figure 6.2.12: Design H, mid station
- Figure 6.2.13: Design B, semi station
- Figure 6.2.14: Design H, semi station
- Figure 6.2.15: Design B, tip station
- Figure 6.2.16: Design H, tip station
- Figure 6.2.17: Rootfoil - ah94w301
- Figure 6.2.18: Midfoil - naca 4415
- Figure 6.2.19: Semifoil - sg6041
- Figure 6.2.20: Tipfoil - mh106
- Figure 6.2.21: C_p distribution for designs A, B and C and designs using non-selection profiles

- Figure 6.2.22: Top five performances below the design range
- Figure 6.2.23: Top five performances above the design range
- Figure 7.1: Three-dimensional model of the optimised wind turbine blade
- Figure A.1.1: Interpolation using a blending fraction of 0.8
- Figure A.1.2: Interpolation using a blending fraction of 0.2
- Figure A.1.3: Extrapolation using a blending fraction of 1.8
- Figure A.3.1.1: I-beam model of airfoil
- Figure A.4.2.1: Typical input file for XFOIL
- Figure A.5.1.1: Three-dimensional surface plot of C_p versus windspeed and the pitch angle at 20% span
- Figure A.5.1.2: Contour plot of C_p values
- Figure A.5.1.3: The C_p objective function in relation to the pitch angle
- Figure A.5.2.1: Three-dimensional surface plot of C_p versus windspeed and the pitch angle at 50% span
- Figure A.5.2.2: Contour plot of C_p values
- Figure A.5.2.3: The C_p objective function in relation to the pitch angle
- Figure A.5.3.1: Three-dimensional surface plot of C_p versus windspeed and the pitch angle at 75% span
- Figure A.5.3.2: Contour plot of C_p values
- Figure A.5.3.3: The C_p objective function in relation to the pitch angle
- Figure A.5.4.1: Three-dimensional surface plot of C_p versus windspeed and the pitch angle at 95% span
- Figure A.5.4.2: Contour plot of C_p values
- Figure A.5.4.3: The C_p objective function in relation to the pitch angle
- Figure A.5.5.1: Chord distribution for different 'b' values along the length of the blade
- Figure A.5.5.2: Chord distribution for different 'a' values along the length of the blade
- Figure A.5.5.3: Three-dimensional surface plot of C_p versus windspeed and 'b'
- Figure A.5.5.4: Contour plot of C_p values
- Figure A.5.5.5: The C_p objective function versus 'b'
- Figure A.5.5.6: Three-dimensional surface plot of C_p versus windspeed and 'a'
- Figure A.5.5.7: Contour plot of C_p values
- Figure A.5.5.8: The C_p objective function versus 'a'

LIST OF TABLES

- Table 4.1.1: Design variables for the Rotor Optimisation
- Table 6.1.1: Aerodynamic characteristics of the base profiles and root airfoil
- Table 6.1.2: Results from five optimisation tasks
- Table 6.1.3: Initial and resultant percentage composition for each task
- Table 6.1.4: Aerodynamic characteristics of base profiles and mid airfoil
- Table 6.1.5: Results from five optimisation tasks
- Table 6.1.6: Initial and resultant percentage composition for each task
- Table 6.1.7: Aerodynamic characteristics of base profiles and semi airfoil
- Table 6.1.8: Results from five optimisation tasks
- Table 6.1.9: Initial and resultant percentage composition for each task
- Table 6.1.10: Aerodynamic characteristics of base profiles and tip airfoil
- Table 6.1.11: Results from six optimisation tasks
- Table 6.1.12: Resultant percentage composition for each task
- Table 6.2.1: Summary of Optimisation Tasks
- Table A.2.1: Root profile
- Table A.2.2: Mid profile
- Table A.2.3: Semi profile
- Table A.2.4: Tip profile
- Table A.5.1: Design variables considered in analysis

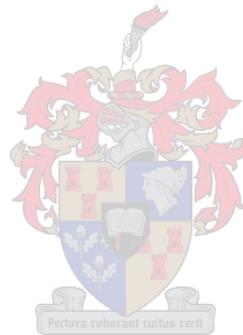


NOMENCLATURE

1-D	one-dimensional
2D	two-dimensional
3D	three-dimensional
a	axial induction factor
a'	tangential induction factor
A	area
a	magnitude variable for the chord length function
b	shape variable for the chord length function
B	number of blades
BEM	Blade Element Momentum
c	chord length
C_θ	rotational velocity in the wake of the rotor
C_d	lift coefficient
C_l	lift coefficient
C_m	nose-down pitching moment
C_{mmean}	average nose-down pitching moment
C_p	Coefficient of Power
C_{pobj}	weighted sum of the C_p values at each windspeed
C_T	Coefficient of thrust
CFD	Computational Fluid Dynamics
F	Prandtl's tip-loss factor
F_N	normal force component
F_T	tangential force component
HAWT	Horizontal Axis Wind Turbine
L/D	lift-to-drag ratio
L/D_{area}	Area beneath the L/D ratio curve
M	torque
MMFD	Modified Method of Feasible Directions
n_{crit}	transition criterion in XFOIL
p	pressure
p_o	atmospheric pressure
P	power
PSO	Particle Swarm Optimisation
r	local radius of rotor
R	full radius of rotor
rpm	revolutions per minute



SQP	Sequential Quadratic Programming
SLP	Sequential Linear Programming
T	thrust
tsr	tipspeed ratio
u	axial velocity through rotor disk
u_1	velocity in the wake
V_a	axial velocity
V_o	average windspeed
V_{rot}	rotational velocity
V_{rel}	relative velocity
w	downwash
α	angle of attack
ϕ	flow angle
ρ	density
σ	solidity
θ	pitch angle
ω	rotional speed in rad/s



1. INTRODUCTION

In recent years, an amplified global awareness has led to a reawakening of interest in renewable energy technology. In an effort to reduce the worldwide dependence on fossil fuels, cleaner power generation methods are being sought in the fields of solar, biomass, wind and wave energy. The World Wind Energy Conference held in November 2003 in Cape Town reasserted the imperative role of wind energy for future power generation, specifically in South Africa.

South Africa presents a unique wind energy situation. According to a wind resource assessment carried out by the Council for Scientific and Industrial Research (CSIR) and the Department for Minerals and Energy (DME), South Africa experiences average wind speeds in the region of 4 to 7 m/s. The best available wind resource exists on the West Coast - refer to Figure 1.1.1. Unfortunately, these wind speeds are considered quite low when compared to an international market which designs for turbine cut-in speeds higher than South Africa's highest average wind speed. Furthermore, the significant variance of the average wind speeds decreases their useful potential. This indicates the need for technology specific to the low windspeed conditions of South Africa.

South Africa's interest in wind energy has, to date, been limited to small-scale wind energy installations for battery charging purposes or private power production on smallholdings. Extensive studies into small-scale installations have been conducted by the CSIR. A large-scale project is the 3.16 MW facility initiated by Eskom as a demonstration project at Klipheuwel near Malmesbury. It is expected that research into efficient wind rotor design should present more opportunities for wind energy exploitation.

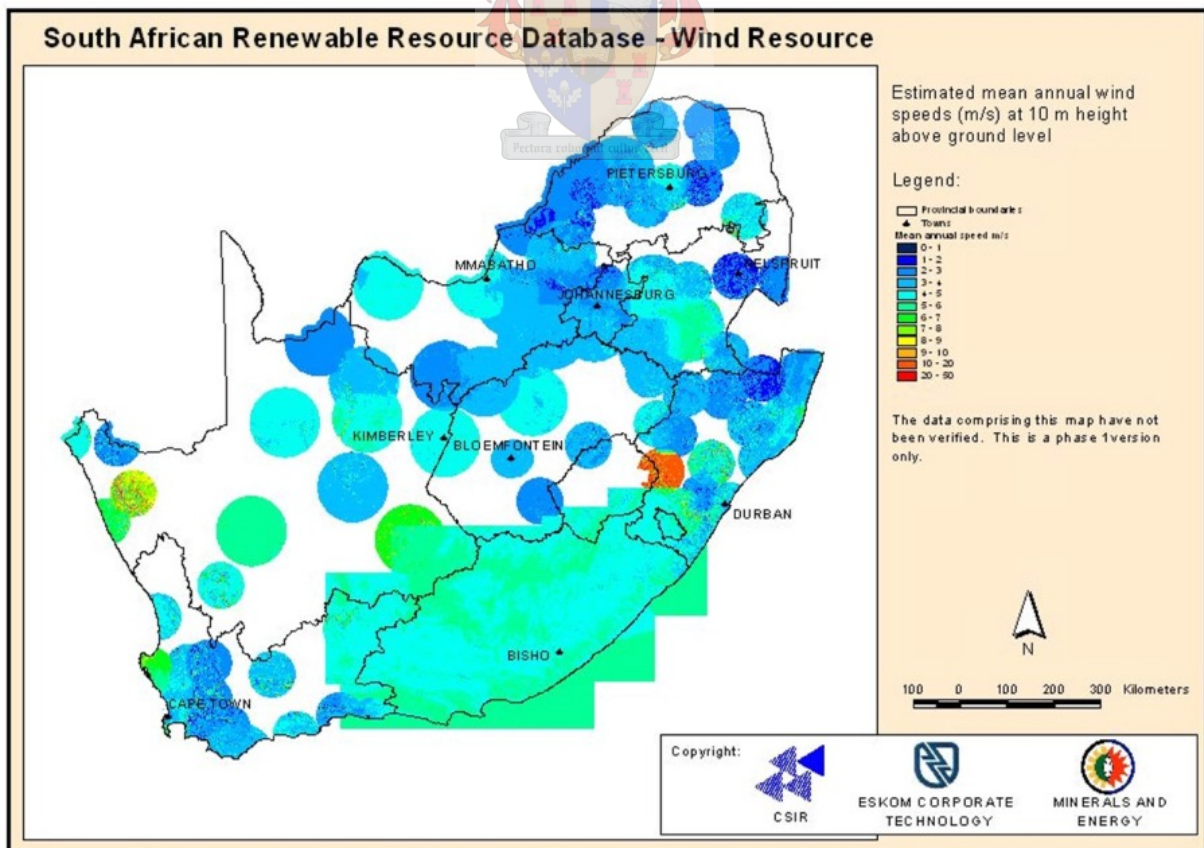


Figure 1.1.1: Meteorological Survey of Southern Africa

Aerodynamic design of Horizontal-Axis Wind Turbines (HAWTs) is characterised by several trade-off decisions. In the past, the multi-variable design problem has been solved using single design point iterative techniques with suitable prediction tools. However, the introduction of optimisation within the aerodynamics and wind turbine industry, has allowed consideration of multiple design points simultaneously. Furthermore, the fluctuating behaviour of the wind presents the challenge of designing a rotor able to produce consistent peak performance over a range of windspeeds. The optimisation methods employed in this project provide a means of balancing the trade-offs such that the most favourable blade aerodynamic characteristics can exist within a pre-selected windspeed range.

Optimal performance is assessed in terms of the Coefficient of Power (C_p). This factor rates the rotor's ability to extract energy from the available wind stream and is calculated for each windspeed within the pre-selected range. Optimisation of performance is considered from a purely aerodynamic perspective and does not give large consideration to such factors as structural integrity, or electrical power quality. Justification for this focused investigation resulted from collaboration with the CSIR. Their previous study supplied the context and application for this wind rotor investigation, taking into account those factors to be considered for a small-scale, low windspeed application (Denton, 2003). This rotor became the baseline for rating the design improvement of each optimised rotor design.

To simplify both analysis time and analysis complexity, the three-bladed wind rotor is simulated as a single blade with four radial stations. The solution strategy first regarded the two-dimensional optimisation of the airfoil profiles used at the radial stations. Thereafter, the three-dimensional (3D) geometric features of the full blade were optimised. Separate optimisation calculations were carried out for each radial station. Investigation into wind rotor design literature revealed the desirable two-dimensional aerodynamic properties. These were set as objectives for optimisation at each station. The creation of airfoil profiles was achieved by blending the co-ordinates of existing airfoil profiles. The influence of each profile became a design variable in the optimiser. This is a simple and robust approach to profile design, but was selected due to the difficulties of complex geometry creation within optimisation. Each new airfoil profile was subjected to viscous/inviscid analysis within XFOIL. This is an interactive program for the design and analysis of subsonic, isolated airfoils.

Once the four station profiles were determined, the three-dimensional geometric features of the wind turbine blade were optimised. The chord length and pitch angle distributions were analysed using the Blade Element Momentum (BEM) method programmed into a Matlab mfile.

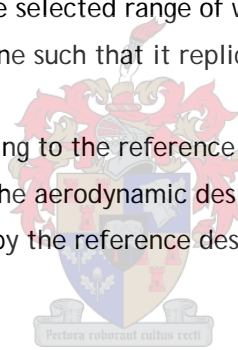
The use of a generic optimisation software package, VisualDOC, enabled experimentation with different optimisation methods. Gradient methods were favoured due to their lack of expense in function evaluations and their steady solving capabilities. The resultant blade design presented in this thesis, offers substantial improvements on the reference design. The application of optimisation methods has successfully aided the creation of a wind turbine blade with consistent peak performance over the range of design windspeeds.

The primary objective for this research is to investigate the feasibility of employing optimisation methods to design a wind turbine blade capable of effective aerodynamic performance which models the reference Weibull frequency distribution within the windspeed range of 5 to 7 m/s. The following thesis document details the procedure followed to design a wind turbine blade for optimal aerodynamic

performance at low windspeed conditions. Research is conducted into current trends of wind turbine design, the application of optimisation techniques and the difficulty of the wind rotor flowfield. The fundamentals of rotor aerodynamics are explained in Chapter 2, as well as a brief overview of the analysis program XFOIL. Chapter 3 provides an introduction to optimisation methods and the use of the optimisation software, VisualDOC. The design approach for the wind turbine is illustrated in Chapter 4 and formulates the selection of objectives and constraints, as well as the design variables used. Most of the design strategy was formulated from literature and modified according to the results from initial optimisation attempts. In Chapter 5 the BEM code and XFOIL analysis capability is verified against experimental results from two different sources. Finally, chapter 6 contains the optimisation results for each radial profile as well as the three-dimensional rotor.

Project Objectives

- Conduct the analytical design for a small-scale, stall-regulated horizontal axis wind turbine blade
- Employ optimisation theory in the design method
- Design specifically for low windspeed application (5 to 7 m/s)
- Ensure peak performance over the selected range of windspeeds
- Bias the performance of the turbine such that it replicates the Weibull probability windspeed distribution
- Rate the optimised design according to the reference design provided by the CSIR step report
- Limit the scope to consider only the aerodynamic design of the wind turbine. The electrical and structural requirements are met by the reference design.



1.1 Literature Review

1.1.1 Unsteady Aerodynamics Associated with Wind Turbines

“Implementation of design improvements within the wind turbine industry is hampered by the lack of practical prediction tools having the appropriate level of complexity.” (Bermúdez *et al.*, 2002) Wind turbine design graduated from the airfoil design industry with much of the same theory being applied. However, the flow conditions are unique. Often the assumptions made in flight aerodynamics are not applicable to wind turbine flowfields. The flowfield is three-dimensional, incompressible, unsteady, turbulent, and separated to a large extent; therefore numerical analysis is complex and costly. Most prediction tools in industry are based on suitably evolved blade element methods, with semi-empirical correlations to account for the three-dimensional effects, boundary-layer separation, and unsteady flow conditions. The benefit of these methods is that they are cost efficient, relative to the analysis time of full computational fluid dynamics (CFD). Unfortunately, their prediction of wind turbine performance has been found to be much lower than that encountered in the field (Tangler, 2002). Nevertheless, the blade element methods are widely applied in the wind turbine industry.

Prediction of wind turbine performance within the context of fluctuating wind conditions complicates the application of steady-state theory. In the Blade Element Momentum (BEM) Theory, the wind turbine blade is discretised into separate blade segments and analysed from a two-dimensional (2D) perspective. The angles of incidence and the consequent forces experienced by the wind turbine profile vary as a result of the rotation of the blade and the fluctuating wind. Not only do the forces experienced by the structure become dynamic, but also prediction methods such as BEM are compromised due to their assumptions of steady-state flow. The problem of oscillating airfoils is of particular importance for wind turbine design since airfoils spend a large amount of their time in the stall region (Bermúdez *et al.*, 2002).

The effect of turbine rotation on the boundary layer of the airfoil profile also affects the prediction of the aerodynamic forces, since rotation affects the transition to turbulence. Du and Selig (2000) pointed out the difficulty of using the BEM methods since they do not model the effect of rotation on the boundary layer of the wind turbine blade. There is an estimated 15 to 20% under-prediction of the performance. The fact that the angle of incidence is continuously varying during the rotation cycle means that the circulation around each blade element is also varying. The conservation of angular momentum requires therefore that vorticity is shed into the wake of the turbine, also continuously. There is a bound vortex around each blade element and there is a free vortex system being convected downstream with the wake (BWEA, 1982).

Yawing of the wind turbine rotor disk due to wind gusts, changes in wind direction, or passage through the wake of the cylindrical support tower causes dynamic stall to occur at the airfoil profile. Tests on pitching rectangular wings resulted in lift overshoots during the vortex formation process. A twisted blade encourages the occurrence of dynamic stall at different sections of the blade at different times, instead of along the entire blade at one time.

Furthermore, prediction of the induced velocities in the flowfield around the wind rotor is often a leading factor for under-prediction of wind rotor power production. Sørensen and Hansen (1998) investigated calculation of rotor performance using a one-bladed and a three-bladed model. Their research compared the blade forces at 5 m/s and 10 m/s. At the low speed, the induced velocities for both models were a large fraction of the undisturbed velocity. At the higher speed, the induced velocities were a smaller fraction. Naturally the three-bladed rotor experienced much greater induced velocities than the single-bladed. The under-prediction of power production was greatest at the higher windspeed and specifically for the single-bladed model.

Rotational effects on the boundary layer, induced velocity and wind rotor yaw are but a few of the operational conditions to consider when designing a wind turbine blade. Generating an accurate, analytical model is problematic when considering these operational conditions. However, simplified models for wind turbine blades have been verified as a dependable design strategy due to their common occurrence in literature. The advancement of computational tools will allow greater consideration of the unsteady aerodynamics associated with wind turbines in the future.

1.1.2 Optimisation within Wind Turbine and Airfoil Design

The success of any optimisation design is dependent on the clear definition of the design objective as well as the limitations on the solution space. Definition of the solution space is dependent on the extent of freedom of the design variables. Optimisation methodology is widely applied due to the rapid increase of multi-variable problems within engineering. The design of a wind turbine blade is such a multi-variable problem. There is growing evidence of the application of optimisation within wind turbine design projects. The tendency within literature has been to simplify design models, either using lower-order accuracy analysis techniques or limiting the degrees of freedom of the design variables (Fuglsang and Madsen, 1999; Timmer van Rooij, 2003). These measures minimise analysis time and cost. Much of the optimisation problem formulation within this project has been replicated from that which exists in literature.

The wind turbine mechanism itself comprises many different design disciplines - electrical, mechanical, structural, and economic. Many optimisation projects conduct research into one field or a combination of a few. Economic design considerations have often been applied, where the design objectives are annual energy production and cost of energy. Benini and Toffolo (2002) conducted such a multi-objective optimisation problem. In this research the wind turbine blade was modelled using a fixed airfoil family at four stations along the span. The design variables were the rated power of the turbine, the radius, as well as the chord length and pitch angle distributions. The chord length and pitch angle distributions were described using Bezier functions. BEM methods were used to calculate the aerodynamic performance of the blade. In this research, it was sufficient to use a simplified cost model based on broad assumptions. For example, it was assumed that the blades would constitute only 20% of the turbine cost and turbine cost itself had a linear relationship with weight. Nevertheless, it was interesting to note the success of a simplified optimisation model.

Giguère *et al.* (1999) used a similar multi-objective function set-up. However, the main purpose of this research was to investigate the effect of low-lift airfoils, thus defining a lower limit for airfoils for stall-regulated wind turbines. The same objectives as those used in Benini and Toffolo's research (2002) were optimised but a genetic algorithm was used instead. The chord length and pitch angle distributions were modelled at four radial stations (15% 40% 75% 95%) using a cubic spline. The rotor diameter was variable. Low-lift airfoils were found to exhibit softer stall characteristics compared to the high-lift foils. The softer stall characteristics are beneficial for extending the operating range of the airfoil. On the other hand, high-lift foils are good for the starting torque of the wind turbine and for minimizing blade solidity. This research provided a guideline for the constraints in the current work on the maximum coefficient of lift (C_L) values at the hub, mid and tip airfoils of the blade - 1.79, 1.38, 1.16 respectively.

Chaviaropoulos *et al.* (2001) demonstrated another method for the optimisation of profiles for stall-regulated Horizontal Axis Wind Turbines (HAWT's). Optimised lift and drag characteristic curves for maximum energy capture of the wind turbine blade allow the user to determine the objectives for each airfoil profile. The profiles were then optimised to match these set objectives. The profiles were designed using inverse viscous/inviscid methods and were analysed at average Reynolds numbers and a range of incidence angles. These incidence angles were representative of the range of angles the profiles would

experience during operation. Thereafter, the designed blade performance was validated using a direct BEM analysis.

The challenges of optimisation within other aerodynamics fields were researched. Optimisation methods have been applied to airfoil design using CFD. This is commonly known as computational flow optimisation (CFO). This method is extremely lengthy due to the iterative nature of CFD software and optimisation methods. Generally, the design geometry as well as the mesh of the flowfield is optimised. This leads to a vast increase in design variables for optimisation. Furthermore, the automation of CFD within an optimisation program is an intricate task. In general, better CFD results are obtained when mesh refinements are tailored to the design geometry. However, to ensure repeatability in the optimisation iteration, the mesh has to be the same for each design (Craig *et al.*, 1999).

There are different methods of describing the geometry in airfoil design. Some of these use fractional arc lengths, polynomial formulation, shape functions or conformal mapping technique. Selig and Maughmer (1992) laid out a generalised multipoint inverse airfoil design where a velocity distribution yielding the desired boundary-layer development is designed using inverse boundary-layer methods. The velocity distribution is changed according to experience and feedback from successive analyses. The airfoil design thus relies on the intuition of the programmer and does not use optimisation methods.

In his research on the pros and cons of airfoil optimisation, (Drela, 1998) allowed the airfoil shape to be described by fractional arc lengths. The airfoil shape was then optimised to fulfil a minimum drag requirement. The results yielded physically unrealisable airfoils with the occurrence of bumps on the surface of the airfoil. The optimiser created these bumps to compensate for the separation bubbles which occur along the surface. These small-scale irregularities had almost no aerodynamic penalty with the result that they were invisible to the optimiser. Furthermore, the airfoil shape had many design parameters or degrees of freedom. Thus, the method laid out in the research paper was of high computational cost. This research brought particular attention to the importance of limitations on design variables. In effect, an optimiser does not have the intuition or experience of a human programmer and will thus not recognise infeasible solutions.

A simple means of describing the airfoil geometry is laid out by (Vanderplaats, 1979). A main focus of his research was to improve the efficiency of the automated design capability. The efficiency was measured by the number of times the aerodynamics program is called for a complete analysis of the airfoil geometry. Two methods of defining the airfoil shape were attempted. Firstly, polynomials were used to describe the airfoil's upper and lower surfaces. The polynomial coefficients were the design variables. Secondly, the airfoil geometry was described in terms of generic shape functions or basis vectors. The generic shape functions were blended to produce the resultant airfoil. The blending fractions became the design variables. This second method of airfoil representation resulted in an increase in optimisation efficiency by a factor of two. Furthermore, this method proved to be robust and versatile to different optimisation techniques.

1.1.3 Verification of Wind Turbine Prediction Data

The use of lower-order accuracy analysis techniques within wind turbine design greatly simplifies the design problem, however, these techniques would be useless if they did not correlate with actual field or wind tunnel measurements. (Huyer *et al.*, 1996) pointed out the difficulty of verifying field wind turbine data with wind tunnel results and BEM methods. Apparently the complex, unsteady flowfields may be responsible for the under-prediction of wind turbine loads, and their consequent component failure. An experiment to measure actual pressure fluctuations on a wind turbine blade in the field was set up to investigate the accuracy of BEM. Surface pressure data was recorded from several pressure transducers at various spanwise locations along the blade. The sampling rate was high enough to capture detailed occurrences in the flow. The pressure data was compared to steady-state, two-dimensional wind tunnel test data to approximate the influence of unsteady effects. The wind tunnel test was set-up to replicate the aerodynamic environment of the field test, thus the average flow speeds and angles of attack encountered in the field. The peak power levels of the wind turbine were significantly greater than those predicted using two-dimensional wind tunnel data and BEM methods.

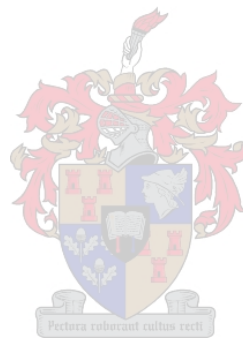
The surface pressure data demonstrated highly transient and spatially complex aerodynamic behaviour. The lift coefficient values were significantly higher than those predicted from wind tunnel test data. The actual loading and power output experienced in the field was under-predicted by BEM. For the low windspeed case, the normal force coefficients (C_n) for the field test data were 10% less than their predicted counterparts. As the windspeed increased, C_n became greater than the predicted values such that lift overshoots (into and out of tower shadow) tended to be 40% greater than the maximum predicted values. Integration of these normal force data also revealed unreliable prediction methods in terms of the magnitude of forces experienced by the wind rotor disk (Huyer *et al.*, 1996).

Since wind turbine design is often conducted analytically, it is important to consider the discrepancies between actual and analytical performance. In a study by Ronsten (1992) the static pressure measurements on a rotating blade and non-rotating blade were compared with calculations using two-dimensional analysis programs, such as XFOIL. To obtain the two-dimensional equivalent angles of incidence for the rotating blade section, the Glauert thrust model was used. The airfoil profile was then analysed within XFOIL at these angles of attack.

Good agreement was found between the lift coefficients for the rotating and the non-rotating blade at all radial stations, up to moderate angles of attack. Moderate angles of attack were considered to be 10° to 15° . The pressure distributions calculated in XFOIL and measured on the rotating blade for the wind turbine airfoil, were compared radially and at specific angles of attack. There was good agreement at most stations, except at 30% and 97% of the radius. This is where hub and tip losses would have considerable effect. The wind rotor power coefficient was calculated using a BEM program and compared to actual mechanical torque measurements. At low to medium tip speed ratio (tsr), power is under-predicted by the BEM program. At high tsr, the agreement is much better. These discrepancies can be attributed to the Glauert thrust model's under-prediction of the hub and tip losses. Furthermore, Prandtl's tip loss factor does not off-load the tip as much as is needed to draw reasonable comparison between calculation and measurements (Ronsten, 1992).

Verification of wind turbine prediction data does justify the use of BEM prediction methods which analyse the blades from a two-dimensional aerodynamic perspective. BEM does have shortcomings, such as no stall-delay model and an inadequate tip-loss model. However, its ability for robust analysis and low computational cost make it advantageous. Furthermore, assuming a two-dimensional nature for the flow over the blade seems to be an adequate assumption (Timmer and van Rooij, 1992).

In essence, the literature review provided a guideline for defining the model for use in this optimisation project. The literature review recognised those design features to be prioritised and laid out those analysis techniques which would be the most suitable. A simplified model of the wind turbine blade with four radial stations, analysed according to BEM methods with tip loss corrections, was justified. Furthermore, representation of the airfoil profiles as blended shape functions became a feasible concept. Repeatability of the analysis results was prioritised and had significant influence on the programming of XFOIL within the design process.



2 ROTOR AERODYNAMICS

Many similarities exist between wind rotor aerodynamics, and aeroplane wing aerodynamics. In fact, the same two-dimensional airfoil theory is applied to both, except that the rotational effects of the flow are accounted for when considering a wind rotor. This section illustrates two of the fundamental concepts in rotor aerodynamics - One-Dimensional Momentum Theory and Blade Element Momentum (BEM) Theory. Though this theory has been found to under-predict the power output and loading on a wind turbine, it has wide application in wind turbine design.

The vortex system of the wind turbine is similar to that of the linear, translating wing, except that the vortex sheet of trailing vortices is orientated in a helical path behind the rotor. Strong tip vortices exist at the edge of the rotor wake, while the root vortices lie in a linear path along the axis of rotation. The vortex system induces an axial and a tangential velocity component. Such induced velocity is referred to as downwash in aeroplane wing aerodynamics. The induced velocity components act in the opposite direction to the wind and the rotation of the blades. The induced velocity is represented by axial and tangential induction factors. The resultant axial and tangential velocities are displayed in equations (2.1) and (2.2).

$$V_a = (1 - a)V_o \quad (2.1)$$

$$V_{rot} = (1 + a')\omega r \quad (2.2)$$

The axial and tangential induction factors play a vital role in determining the power output from a wind turbine blade. These will be referred to in the subsequent theory.

2.1 One-Dimensional Momentum Theory

The essential function of a wind rotor is to extract mechanical energy from the kinetic energy of the wind. The derivation of how this energy is extracted is approached from a mathematical perspective, in which a few basic assumptions need to be made. In One-Dimensional Momentum Theory, the rotor is approximated as an actuator disc, and the flow assumed to be ideal. This fulfils the conditions of frictionless flow with no rotational velocity component in the wake of the rotor. The actuator disk slows the wind speed from V_o far upstream, to u at the rotor plane and u_1 in the wake. u is the axial velocity through the rotor. Refer to Figure 2.1.1. The streamlines tend to diverge when passing through the actuator disk. Energy is extracted from the wind. When examining the effect of the actuator disk on pressure, it is evident that close to the disk, there is a small pressure rise from the atmospheric pressure such that $p > p_o$, followed by a discontinuous pressure drop over the disk Δp . Downstream, the pressure recovers to atmospheric conditions.

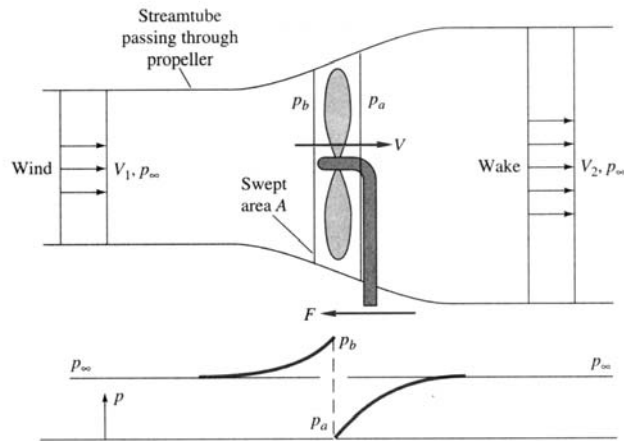


Figure 2.1.1: Schematic of the streamlines past the rotor (White, 1999)

The assumption of an ideal rotor allows for the derivation of the relationships between velocities, thrust and absorbed shaft power. Thrust is the force in the streamwise direction, which results from a pressure drop over the rotor. This force is used to break the wind speed from V_o to u_1 .

$$T = \Delta p A \tag{2.1.1}$$

where $A = \pi R^2$ is the area of the rotor. In order to define the pressure drop over the rotor, Bernoulli's equation is applied before and after the rotor disk, excluding the rotor disk though. Bernoulli's equation is valid since the flow is steady, frictionless, and incompressible and there are no external forces or heat transfer. Application to the areas before and after the rotor is demonstrated below:

$$p_o + \frac{1}{2} \rho V_o^2 = p + \frac{1}{2} \rho u^2 \tag{2.1.2}$$

$$p - \Delta p + \frac{1}{2} \rho u^2 = p_o + \frac{1}{2} \rho u_1^2 \tag{2.1.3}$$

The combination of equations (2.1.2) and (2.1.3) yields an expression for the pressure drop:

$$\Delta p = \frac{1}{2} \rho (V_o^2 - u_1^2) \tag{2.1.4}$$

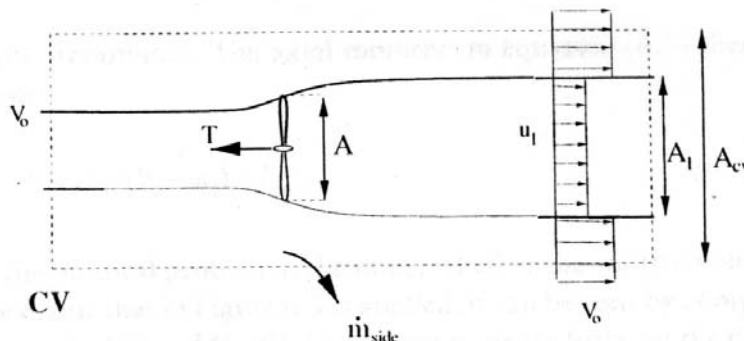


Figure 2.1.2: Circular control volume (Hansen, 2000)

The flow area around a wind turbine can be modelled as a cylindrical control volume (CV) as demonstrated in Figure 2.1.2. The axial momentum equation in integral form is applied to this control volume:

$$\frac{\partial}{\partial t} \iiint_{CV} \rho U d(vol) + \iint_{CS} U \rho \mathbf{V} \cdot d\mathbf{A} = F_{ext} + F_{pres} \quad (2.1.5)$$

F_{pres} represents the axial component of the pressure forces, while F_{ext} is the external force acting on the control volume. The first term of equation (2.1.5) is zero since the flow is assumed steady. The last term is zero since the atmospheric pressure is the same on both end planes, and acts on equal areas. The pressure forces on the lateral boundary of the control volume have no axial component. Therefore, equation (2.1.5) can be simplified:

$$\rho u_1^2 A_1 + \rho V_o^2 (A_{cv} - A_1) + \dot{m}_{side} V_o - \rho V_o^2 A_{cv} = -T \quad (2.1.6)$$

Applying the principle of the conservation of mass through the circular control volume yields an expression for \dot{m}_{side} :

$$\rho A_1 u_1 + \rho (A_{cv} - A_1) V_o + \dot{m}_{side} = \rho A_{cv} V_o \quad (2.1.7)$$

$$\dot{m}_{side} = \rho A_1 (V_o - u_1) \quad (2.1.8)$$

Furthermore, the conservation of mass derives a relationship between areas A and A_1 .

$$\dot{m} = \rho u A = \rho u_1 A_1 \quad (2.1.9)$$

From equations (2.1.8), (2.1.9) and (2.1.6) it is possible to derive an equation for the thrust:

$$T = \rho u A (V_o - u_1) = \dot{m} (V_o - u_1) \quad (2.1.10)$$

If the thrust from equation (2.1.1) is used above, and the pressure drop replaced by equation (2.1.4), then the velocity through the rotor is found to be the mean of the wind speed V_o and the velocity in the wake u_1 .

$$u = \frac{1}{2} (V_o + u_1) \quad (2.1.11)$$

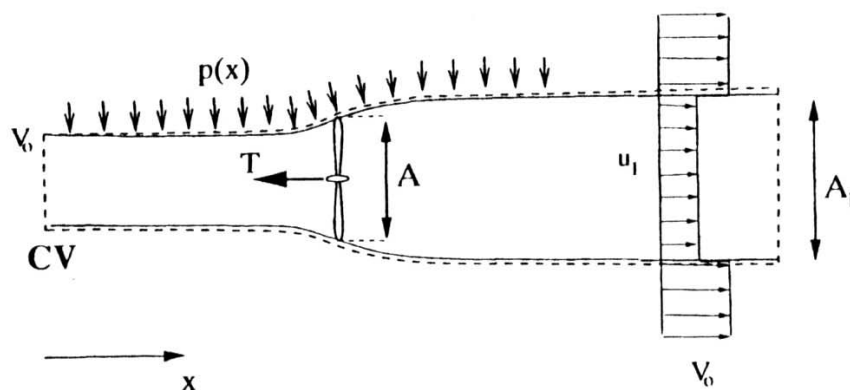


Figure 2.1.3: Alternative control volume (Hansen, 2000)

An alternative control volume can be employed to model flow around a wind turbine. This control volume follows the diverging streamlines of the flow around the wind turbine. Thus, there is no mass flow

through the lateral boundary of the control volume. The pressure forces on the lateral boundary are unknown and thus also the net pressure contribution, F_{pres} . Consequently, the axial momentum equation (2.1.5) becomes:

$$T = \rho u A (V_o - u_1) + F_{pres} \quad (2.1.12)$$

By comparing equation (2.1.12) with (2.1.10), it can be concluded that the net pressure force on the control volume on the streamlines must be zero.

Using the alternative control volume of Figure 2.1.3, it is possible to derive the shaft power P from the wind turbine. The integral energy equation is applied. Since the flow is frictionless, it can be assumed that there is no change in the internal energy from inlet to outlet.

$$P = \dot{m} \left(\frac{1}{2} V_o^2 + \frac{p_o}{\rho} - \frac{1}{2} u_1^2 - \frac{p_o}{\rho} \right) \quad (2.1.13)$$

Since $\dot{m} = \rho u A$, the equation for P becomes:

$$P = \frac{1}{2} \rho u A (V_o^2 - u_1^2) \quad (2.1.14)$$

Due to the extraction of energy from the flow stream, and the physical obstruction of the wind rotor disk, the velocity through the rotor is retarded. The retardation of the axial flow through the rotor disk is expressed in terms of the axial induction factor in equation (2.1). The axial induction factor is used to find the relationship between the upstream velocity, velocity through the disk and downstream velocity.

$$u = (1 - a) V_o \quad (2.1.15)$$

$$u_1 = (1 - 2a) V_o \quad (2.1.16)$$

Substitution of these velocity relations into the expressions for power (equ. 2.1.14) and thrust (equ. 2.1.10) yields the following:

$$P = 2 \rho V_o^3 a (1 - a)^2 A \quad (2.1.17)$$

$$T = 2 a \rho V_o^2 (1 - a) A \quad (2.1.18)$$

The basic function of a wind turbine is to convert the kinetic energy of the wind into mechanical energy. The efficiency of this energy extraction can be rated relative to the available power in the wind.

$$P_{avail} = \frac{1}{2} \dot{m} V_o^2 = \frac{1}{2} \rho V_o^3 A \quad (2.1.19)$$

where A is the area of the rotor disk. The shaft power is then set in comparison to this available power. This provides a dimensionless coefficient of power C_p , which is a measure of the performance of the wind turbine.

$$C_p = \frac{P}{\frac{1}{2} \rho V_o^3 A} \quad (2.1.20)$$

Similarly, an expression for the coefficient of thrust C_T can be obtained.

$$C_T = \frac{T}{\frac{1}{2} \rho V_o^2 A} \quad (2.1.21)$$

To find the above coefficients in terms of the axial induction factor, equations (2.1.17) and (2.1.18) are substituted.

$$C_p = 4a(1-a)^2 \quad (2.1.22)$$

$$C_T = 4a(1-a) \quad (2.1.23)$$

C_p is represented in terms of only one variable in the form of a cubic equation. It is thus possible to find an optimum for C_p by differentiating the equation with respect to a :

$$\frac{dC_p}{da} = 4(1-a)(1-3a) \quad (2.1.24)$$

A maximum C_p value of 16/27 is achieved by choosing a equal to 1/3. This is known as the Betz limit. Considering the assumptions of frictionless, stationary flow, this is the maximum possible C_p . Under this condition, the flow velocity at the rotor disk is 2/3 of the windspeed, and the wake velocity is 1/3 of the windspeed.

2.2 Blade Element Momentum Method

In one-dimensional momentum theory, the actual geometry of the rotor is not considered. The BEM method couples the global momentum theory with the local event occurring at the blade element. The following lays out the classical BEM model as derived by Glauert (Hansen, 2000). The stream tube from one-dimensional theory (Figure 2.1.3) is discretised into N annular elements of height dr . R is the full radius of the stream tube at the rotor disk and r is the local radius. The lateral boundaries of these elements are formed of streamlines. Therefore there is no flow across annular elements. Assumptions for the annular elements were as follows:

1. Each radial element is independent from the next.
2. Force from the blades acting on the flow is constant in each annular element. This corresponds to a rotor with an infinite number of blades. It is consequently assumed that the induced velocity is constant in the azimuthal direction (the direction of rotation for the wind turbine) and is only a function of radius.

In the one-dimensional theory, the pressure distribution along the streamlines did not have a resultant axial force component. Thus the axial momentum equation yields the thrust from the rotor disc. In this case, the control volume is the annular element with a cross-sectional area of $2\pi r dr$:

$$dT = \dot{m}(V_o - u_1) = 2\pi r \rho u (V_o - u_1) dr \quad (2.2.1)$$

The torque dM on an annular element is found from the integral moment of momentum equation applied to the control volume. The rotational velocity upstream of the rotor is set to zero and to C_θ in the wake.

$$dM = \dot{m} r C_\theta = 2\pi r^2 \rho u C_\theta dr \quad (2.2.2)$$

From Euler's turbine equation, it is known that:

$$dP = \dot{m} \omega r C_\theta = \omega dM \quad (2.2.3)$$

The thrust and torque are rewritten using the axial and tangential induction factor relations of equations (2.1) and (2.2).

$$dT = 4\pi r \rho V_o^2 a(1-a)dr \quad (2.2.4)$$

$$dM = 4\pi r^3 \rho V_o \omega(1-a)a' dr \quad (2.2.5)$$

The thrust and torque have been derived from the momentum relations applied to the discretised annular elements. The thrust and torque can be further derived from the local conditions occurring at the blade, using airfoil aerodynamics.

In Figure 2.2.1 the airfoil profile at a cross-section of a wind turbine blade is displayed. V_{rel} is the windspeed relative to the airfoil at a flow angle ϕ . R is the resultant aerodynamic force made up of the lifting force L and the drag force D . The lifting force is perpendicular to V_{rel} and the drag force is parallel. With the orientation and magnitude of the oncoming wind vector known, the coefficients of lift (C_l) and drag (C_d) can be calculated according to standard two-dimensional aerodynamic theory.

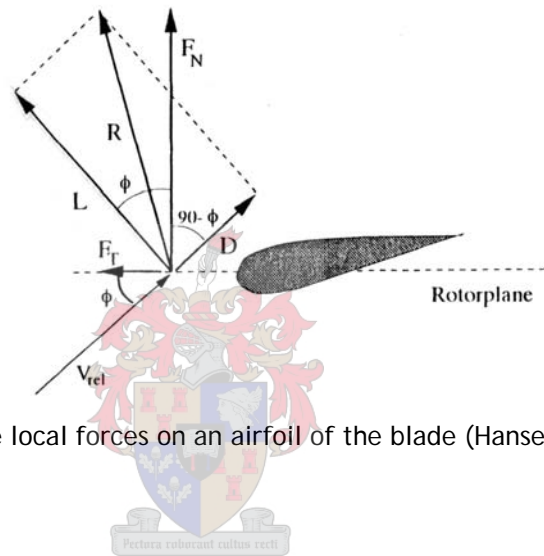


Figure 2.2.1: The local forces on an airfoil of the blade (Hansen, 2000)

$$L = \frac{1}{2} \rho V_{rel}^2 c C_l \quad (2.2.6)$$

$$D = \frac{1}{2} \rho V_{rel}^2 c C_d \quad (2.2.7)$$

The lift and drag forces are projected onto the normal and tangential directions of the rotorplane to construct the normal and tangential components of R .

$$F_N = L \cos \phi + D \sin \phi \quad (2.2.8)$$

$$F_T = L \sin \phi - D \cos \phi \quad (2.2.9)$$

The normal and tangential forces are normalised with respect to $\frac{1}{2} \rho V_{rel}^2 c$

$$C_n = \frac{F_N}{\frac{1}{2} \rho V_{rel}^2 c} \quad (2.2.10)$$

$$C_t = \frac{F_T}{\frac{1}{2} \rho V_{rel}^2 c} \quad (2.2.11)$$

$$C_n = C_l \cos \phi + C_d \sin \phi \quad (2.2.12)$$

$$C_t = C_l \sin \phi - C_d \cos \phi \quad (2.2.13)$$

F_N and F_T are forces per unit length or unit radius in this case. It is these forces which provide the torque and thrust for an element of the blade. The forces are multiplied by the number of blades, B .

$$dT = BF_N dr \quad (2.2.14)$$

$$dM = rBF_T dr \quad (2.2.15)$$

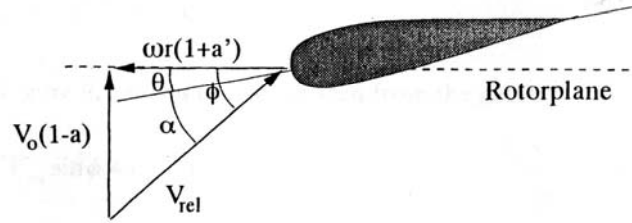


Figure 2.2.2: The inflow velocities at the rotor plane (Hansen, 2000)

Figure 2.2.2 demonstrates a windspeed vector breakdown at the element airfoil. ϕ is the local flow angle, θ is the pitch angle and α is the angle of attack "seen" by the profile. The pitch angle is the angle set as constant between the chord line and rotorplane. Using the above Figure, it is possible to derive an expression for V_{rel} for substitution into equations (2.2.10) and (2.2.11).

$$V_{rel} \sin \phi = V_o(1-a) \quad (2.2.16)$$

$$V_{rel} \cos \phi = \omega r(1+a') \quad (2.2.17)$$

If equation (2.2.10) is used to express F_N , and equation (2.2.16) for V_{rel} , then (2.2.14) becomes:

$$dT = \frac{1}{2} \rho B \frac{V_o^2(1-a)^2}{\sin^2 \phi} cC_n dr \quad (2.2.18)$$

In a similar way, equation (2.2.11) is used to express F_T , and both equations (2.2.16) and (2.2.17) for V_{rel} . Thus (2.2.15) becomes:

$$dM = \frac{1}{2} \rho B \frac{V_o(1-a)\omega r(1+a')}{\sin \phi \cos \phi} cC_t r dr \quad (2.2.19)$$

At this point there are two different expressions for the thrust and torque, obtained according to different means. Should these be equated to each other it is possible to find an expression for the axial and tangential induction factors. Firstly though, a mathematical expression for the solidity is obtained. Solidity is that fraction of the annular area occupied by the blades and is dependent on the radius:

$$\sigma(r) = \frac{c(r)B}{2\pi r} \quad (2.2.20)$$

If the two equations (2.2.4) and (2.2.18) for dT are made equal and the solidity expression substituted, an expression for the axial induction factor is obtained:

$$a = \frac{1}{[(4 \sin^2 \phi / \sigma C_n) + 1]} \quad (2.2.21)$$

If the two equations (2.2.5) and (2.2.19) for dM are made equal and the solidity expression substituted, an expression for the axial induction factor is obtained:

$$a' = \frac{1}{[(4 \sin \phi \cos \phi / \sigma C_t) - 1]} \quad (2.2.22)$$

Accurate prediction of the power output of a wind turbine is dependent on the iterative calculation of the induction factors. The induction factors are estimated before the flow conditions at the airfoil can be calculated. This estimation of the induction factors is verified by recalculating them after the aerodynamic forces have been calculated. It is impossible to know the degree of retardation of the flow before the forces have been calculated and vice versa. Due to the inter-dependence of these values, iteration is necessary. The iteration process is carried out in the following manner:

- Step 1 Initialise a and a'
- Step 2 Calculate the flow angle at the airfoil profile
- Step 3 Calculate the local angle of attack from $\alpha = \phi - \theta$
- Step 4 Compute $C_l(\alpha)$ and $C_d(\alpha)$
- Step 5 Calculate C_n and C_t from equations (2.2.12) and (2.2.13)
- Step 6 Recalculate a and a' from equations (2.2.21) and (2.2.22)
- Step 7 If a and a' have changed by more than a certain tolerance, then the calculation process should be repeated from step 2.
- Step 8 Calculate the normal and tangential forces on the blade segment, and the resultant thrust and torque, equations (2.2.18) and (2.2.19).

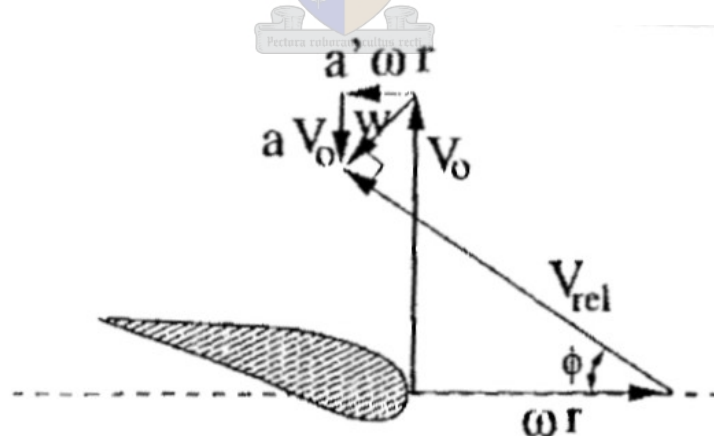


Figure 2.2.3: Induced velocities at the rotorplane (Hansen, 2000)

In Figure 2.2.3 it is possible to note the relation between the induced velocity and the components of the windspeed. V_{rel} is the relative velocity seen by the airfoil. This is a combination of the axial velocity $(1-a)V_0$ and the tangential velocity $(1+a')\omega r$. w is the downwash which is presumed to be perpendicular to the relative velocity, however, this assumption is only valid for angles of attack below

stall. Nevertheless, the above Figure allows a suitable means to estimate the initial induction factor values. The following equations are derived directly from Figure 2.2.3.

$$\tan\phi = \frac{(1-a)V_0}{(1+a')\omega r} \quad (2.2.23)$$

$$\tan\phi = \frac{a'\omega r}{aV_0} \quad (2.2.24)$$

If $x = \frac{\omega r}{V_0}$ denotes the ratio between the local rotational speed and wind speed, the following equation is derived from equations (2.2.23) and (2.2.24):

$$x^2 a'(1+a) = a(1-a) \quad (2.2.25)$$

Equation (2.2.25) provides a useful relation between the axial and tangential induction factors.

2.2.1 Prandtl's Tip-Loss Factor

There are two assumptions necessary for the application of BEM theory. The first is radial independence of the annular elements, and the second is that the force from the blades acting on the flow is constant in each annular element. Certainly, these assumptions are not entirely true. Prandtl's tip-loss factor is an empirical relation which corrects for the second assumption.

According to Glauert theory, the optimum blade is found when its circulation distribution remains uniform along its length. Thus vorticity may only be shed at the root and the tip. Prandtl theorized that the optimum propeller sheds a helical vortex sheet which moves as a rigid body while it is convected away from rotor. The tip-loss factor models these vortex sheets as a series of parallel planes with uniform spacing:

$$F = \frac{2}{\pi} \arccos(e^{-f}) \quad (2.2.1.1)$$

$$f = \frac{B}{2} \frac{R-r}{r \sin\phi} \quad (2.2.1.2)$$

Thus, the tip-loss factor approaches zero near the tip. The thrust and torque also decrease near the tip.

Equations (2.2.4), (2.2.5), (2.2.21) and (2.2.22) are modified to include the tip-loss factor:

$$dT = 4\pi r \rho V_0^2 a(1-a)Fdr \quad (2.2.1.3)$$

$$dM = 4\pi r^3 \rho V_0 \omega (1-a)a'Fdr \quad (2.2.1.4)$$

$$a = \frac{1}{[(4F \sin^2 \phi / \sigma C_n) + 1]} \quad (2.2.1.5)$$

$$a' = \frac{1}{[(4F \sin \phi \cos \phi / \sigma C_t) - 1]} \quad (2.2.1.6)$$

2.2.2 Glauert Correction for High Values of a

When the axial induction factor, a , is higher than a value of 0.4 the simple momentum theory breaks down. At low windspeeds, a high thrust coefficient, C_T , and thus a high axial induction factor exists for a wind turbine. Increases in the C_T lead to increases in the expansion of the wake. There is a resultant velocity jump between the upstream and downstream conditions ($V_o - u_i$). The free shear layer at the edge of the wake becomes unstable and eddies form, which transport momentum from the outer flow into the wake. This is known as the turbulent wake state. Different empirical evaluations of the thrust coefficient have been made to fit experimental measurements, thus compensating for the breakdown of simple momentum theory (Hansen, 2000).

$$C_T = 4aF(1-a) \quad \text{if} \quad a \leq a_c \quad (2.2.2.1)$$

$$C_T = 4F[a_c^2 + (1-2a_c)a] \quad \text{if} \quad a > a_c \quad (2.2.2.2)$$

$(a_c \approx 0.2)$

In the event of high values of a , equation (2.2.1.5) is calculated as follows:

If $a > a_c$:

$$a = \frac{1}{2} [2 + K(1-2a_c) - \sqrt{(K(1-2a_c) + 2)^2 + 4(Ka_c^2 - 1)}] \quad (2.2.2.3)$$

where:

$$K = \frac{4F \sin^2 \phi}{\sigma C_n} \quad (2.2.2.4)$$

2.3 Two-dimensional Stacked Design using XFOIL

The two-dimensional stacked design concept is introduced as a practical tool for determining the performance of a wind turbine while at the same time limiting computational expenditure. The stacked design concept divides the full three-dimensional blade into discontinuous sections or stations. The airfoil cross-sections of these stations are analysed according to standard aerodynamic principles. Thereafter, the full three-dimensional performance is calculated according to BEM methods. XFOIL has proven to be a useful tool for analysis of airfoil sections within the wind turbine industry and flight aerodynamics. Mark Drela wrote the first version of the code in 1986 (Drela, 2001). XFOIL version 6.94 was used in this study. Included in this section is a brief description of the programming ideology behind XFOIL.

XFOIL is an interactive program for the design and analysis of subsonic, isolated airfoils. The XFOIL code couples a two-dimensional panel method for inviscid analysis with an integral boundary-layer method to obtain a viscous solution. There are also options for airfoil design or redesign by a conformal-mapping method or user-specification of certain geometric parameters.

The inviscid formulation is a linear-vorticity stream function panel method. The airfoil contour and wake trajectory are discretised into straight panels. Each airfoil panel has a linear vorticity distribution, and each airfoil and wake panel also has a constant source strength associated with it. The source

strengths are later related to quantities that define the viscous layer for the boundary-layer method, thus linking the inviscid/viscous analysis method. The total velocity at each point on the airfoil surface and wake is obtained from the panel solution with the Karman-Tsien compressibility correction added. This correction provides good prediction up to sonic conditions but the theory breaks down in supersonic flow. Accuracy degrades in the transonic region. The reason for this phenomenon is that the wake trajectory for the viscous calculation is taken from the inviscid solution at the specified angle of attack. Strictly speaking, viscous effects tend to decrease the lift and change the wake trajectory. However, this correction to the trajectory is not performed since this would result in longer calculation times. The effect of the approximation on the overall accuracy is small, and is felt mainly near or past stall. Considering that wind turbine airfoils should spend much time at or near stall for maximum efficiency (Huyer, 1996), the inaccuracy of XFOIL within this flow regime meant that it would not have been the most suitable analysis program. However, XFOIL was readily available, highly versatile and has been proven in other wind turbine projects where the discrepancies were quantified (Ronsten, 1992; Timmer and van Rooij, 1992; Timmer and van Rooij, 2003; Bosman, 2003).

2.3.1 XFOIL Prediction of Transition

Transition in XFOIL is triggered by one of two ways: forced transition or free transition. Prediction of forced transition occurs when a trip or the trailing edge of the airfoil is encountered. The user sets the trip position. The occurrence of free transition is predicted using the simplified envelope e^n method. The e^n method is only appropriate for predicting transition in situations where the growth of two-dimensional Tollmien-Schlichting waves via linear instability is the dominant transition initiating mechanism. For the growth of the Tollmien-Schlichting waves to be considered linearly unstable, it must be assumed that each disturbance is much smaller than the original wave.

The e^n method is always active within XFOIL and relies on a user-specified n_{crit} parameter. The choice of n_{crit} is dependent on the ambient disturbance level in which the airfoil operates. An n_{crit} value equal to nine is taken as an indication of the disturbance encountered within the average wind tunnel. A value lower than nine indicates a higher disturbance level, as in the case of a dirty wind tunnel. Values higher than nine are indicative of more uniform flow such as in the case of gliders.

When considering how the transition criterion applies to a wind turbine blade, it is important to note that each blade is rotating in a fluctuating windstream. Thus, the flow as seen by the blade experiences high levels of disturbance. Reference to other wind turbine airfoil design projects using XFOIL suggests the use of an n_{crit} parameter in the range of four to six (Bosman, 2003). The best correlation between experimental results for the RAF-6D profile used in the CSIR project and calculated results within XFOIL was obtained for an n_{crit} of 6.

2.3.2 XFOIL within the Design Process

The optimisation design process is automated and run through a number of iterations to obtain the optimal solution. In this design of an optimal airfoil the optimiser, VisualDOC, is configured to run XFOIL

and the associated calculation programs. The optimiser prompts XFOIL by conveying a text-based input file and reading the text-based output file generated by XFOIL. The input file contains the information necessary for definition of the airfoil and the conditions for analysis. This input file is modified by the optimiser upon each successive iteration. XFOIL then generates the new airfoil and analyses it, as specified in the input file. XFOIL exports an output file containing the aerodynamic characteristics of the airfoil. These characteristics are then post-processed and the adequacy of the airfoil in fulfilling the design objective is rated. Essentially, the optimiser views XFOIL as a black box which is given an input, and expected to produce an output. If there is a convergence error within XFOIL, this is only discovered when the output file is empty. Though this is not a difficult eventuality to plan for in the program, XFOIL has been known to become unstable when fed a bizarre airfoil. In this case, XFOIL tends to hang in midair and has to be manually shut down. This results in a collapse of the optimisation iteration and it must be initiated again.

XFOIL has been used in the past for analysis of wind turbine blades. In a study conducted by Ronsten (1992) static pressure measurements on a rotating blade and a non-rotating blade were compared with calculations using two-dimensional analysis methods, such as XFOIL. Certain stations along the length of the blade were selected and their experimental measurements compared with predicted results. The lift coefficients calculated in XFOIL proved to have a good correlation with the actual values from the local stations on the non-rotating blade. However, this correlation existed only up to moderate angles of attack, between 10° and 15° . In the case of the rotating blade, there was good agreement at most radial stations except those at 30% and 97% of the rotor radius. These discrepancies can be attributed to the method of calculation of the relevant angles of attack. For the rotating blade, it is difficult to determine the correct two-dimensional angles (Ronsten, 1992).

The Delft University used XFOIL to design efficient airfoils for the specific application of wind turbines (Timmer and van Rooij, 2003). Their correlation between XFOIL and wind tunnel results demonstrated that XFOIL over-predicts the maximum lift coefficient, $C_{l_{max}}$, of the profile. Furthermore, XFOIL had convergence problems in the region of stall. There was an attempt to modify XFOIL to account for rotational effects. This resulted in the program RFOIL. The results from RFOIL proved to follow experimental results quite well, with an improved prediction of $C_{l_{max}}$. Unfortunately, the drag remained under-predicted and the lift gradient relative to the angle of attack was too steep. Thus, though RFOIL offered an improvement on the predictions of XFOIL, it could still not adequately represent the true three-dimensional characteristics of a wind turbine.

Accurate prediction is of course an essential feature of the analysis program. However, in the case of optimisation, each design is improved relative to the initial design. Optimisation of this improvement is the end result of the design problem. As long as the shortcomings of the analysis program are fairly constant, this allows the user to overlook the analysis errors and instead focus on the consistency and computational economy afforded by the program.

The definition of optimisation is an act, process, or methodology of making something (a design, system, or decision) as fully perfect, functional, or effective as possible. The degree of perfection of the solution is dependent on the optimisation search procedure as well as the definition of the boundaries of the search or solution space. Optimisation methods employed in engineering problems involve the application of mathematical functions to conduct a methodical search of a solution space. Optimisation is most useful in those applications where the solution space cannot be easily characterised or trended. This most notably occurs in multiple, inter-dependent design variable engineering problems.

Essentially, the goal of the design problem is represented by a mathematical objective function. The objective function is dependent on certain design variables. The solution space is that region of feasible solutions for the design problem, and is described by the bounds on the design variables and objective. The optimum value for the objective function is not known *a priori*, thus different search methods are employed. These fall under the categories of gradient-based, non-gradient based and response surface approximation. Three gradient-based methods and one non-gradient based method has been used in this design project. The theory of these methods is introduced in the following sections.

3.1 Gradient-Based Optimisation

Gradient-based methods search for the optimum solution by defining a search vector indicating the direction of the most feasible location of the optimum. As in basic calculus, the gradient of a function can indicate whether the function is growing or diminishing. In the same manner, the search vector is defined by the partial derivative of the objective function. The gradients indicate the trend of growth of the function. The local optimum along that search vector becomes the launching pad from which to devise a new search vector and a new local optimum. Eventually, the local optima converge to a global optimum.

The basic concepts of gradient-based optimisation are as follows:

- Any design will have an objective function or multiple objective functions. These are described by $F(\mathbf{X})$ where X_i , $i=1$ to N are the design variables.
- The goal for the design is to minimise the objective function. If the intention is maximisation of the function, then $-F(\mathbf{X})$ is minimised.
- If no limits are imposed on the values of X_i or $F(\mathbf{X})$ such that the design is considered acceptable, the design is said to be unconstrained.
- The constrained problem will have limitations on the design variables and/or the objective function.

Thus:

Design variable bounds: $X_i^L \leq X_i \leq X_i^U$

Inequality constraint: $g_j(\mathbf{X}) \leq 0 \quad j = 1, M$

Equality constraint: $h_k(\mathbf{X}) = 0 \quad k = 1, L$

With the objective and various constraints described by these functions, the solution space is ready for exploration. There are a number of methods used to explore the design space, such as linear programming or the method of defining a search vector. The second is explained here.

The steepest descent method is the fastest method of finding the minimum and is described in this section. Thus, the search vector is defined in the direction of the steepest gradient.

$$\nabla F(X) = \begin{Bmatrix} \frac{F(X + \partial X_1) - F(X)}{\partial X_1} \\ \frac{F(X + \partial X_2) - F(X)}{\partial X_2} \\ \dots \\ \frac{F(X + \partial X_N) - F(X)}{\partial X_N} \end{Bmatrix} \quad (3.1.1)$$

Equation (3.1.1) is the partial derivative of the objective function. This is a vector direction. Called a search direction since it defines the direction to move to search the solution space. To move in the steepest descent direction, the search vector is defined as $S = -\nabla F(X)$. As mentioned, a local optimum will first be found along this linear search path.

A step taken in this direction is a scalar parameter labelled α . The starting position or initial design variable is X^0 . Therefore progression is marked by the following expression:

$$X^q = X^{q-1} + \alpha^* S^q \quad (3.1.2)$$

where q is the iteration number.

α^* is the optimum step size taken along the search direction.

Once the local optimum is found, a new search direction is calculated and the process begins again.

From basic calculus it is known that the optimum of $F(X)$ will occur where the derivatives are zero. In essence, this is the Kuhn-Tucker condition which indicates when an optimisation search is complete.

$$\nabla F(X^*) + \sum_{j=1}^m \lambda_j \nabla g_j(X^*) + \sum_{k=1}^l \lambda_{m+k} \nabla h_k(X^*) = 0 \quad (3.1.3)$$

λ is known as a Lagrange multiplier. These constants are given a particular value at the beginning of the optimisation process. If a constraint is not violated, then the corresponding Lagrange multiplier equals zero. However, if the constraint is violated, the Lagrange multiplier assumes its initial value and equation (3.1.3) is penalised according to the degree set by the Lagrange multiplier. The vector summation of equation (3.1.3) is visually displayed in Figure 3.1.1.

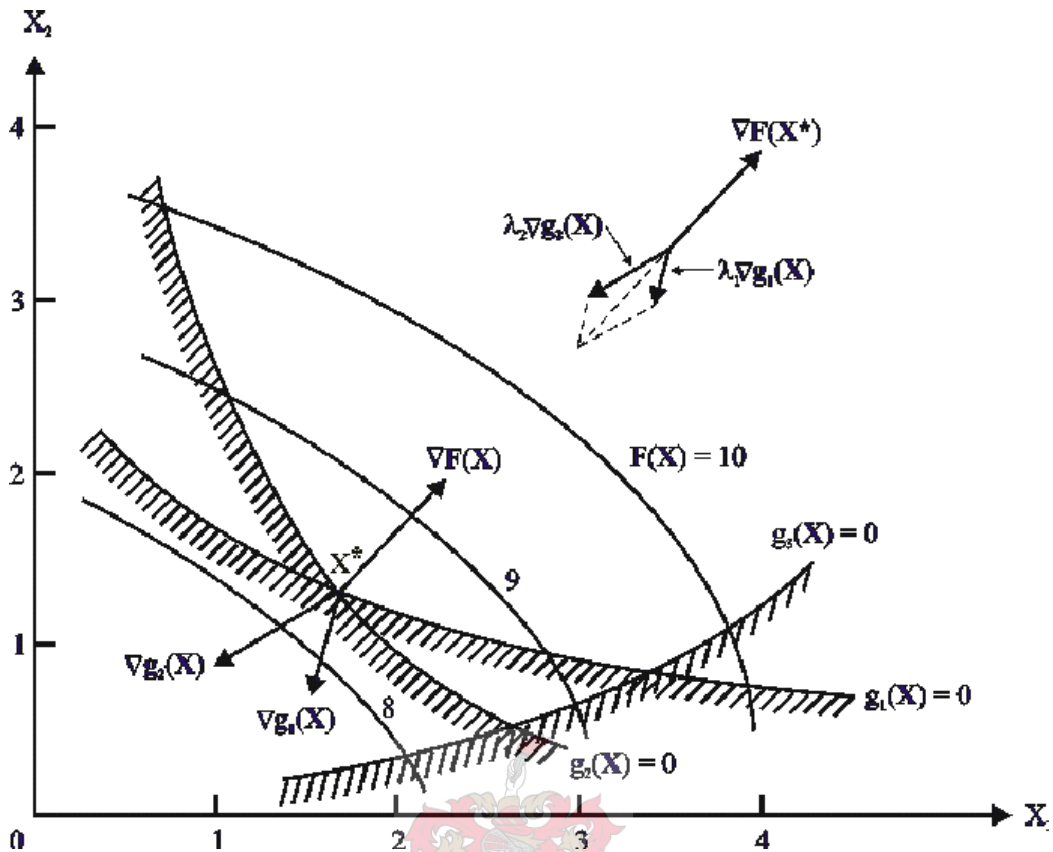


Figure 3.1.1: Solution Space in Gradient Optimisation (Vanderplaats, 2001)

The methods used for constrained functions in this project were Sequential Linear Programming (SLP), Modified Method of Feasible Directions (MMFD) and Sequential Quadratic Programming (SQP). SLP forms a linear approximation of the design problem and its constraints. The objective functions and constraints are linearised via a first-order Taylor series expansion. In order to find the optimum solution within this design space, linear programming methods are used. With the MMFD method, the search direction is first generated and then a one-dimensional search is performed to find the local optimum. Only first-order gradient information is used. Using SQP, a second-order Taylor series expansion is used for the approximation of the objective functions, and the first-order for the constraints.

In all of these methods, the approximations are repeatedly checked to be true. Depending on the deviation between the approximation and the actual, the approximation is adjusted accordingly.

3.2 Non-gradient Based Optimisation

Non-gradient based optimisation employs the use of probabilistic search algorithms within a design problem solution space. Often, these algorithms mimic natural phenomena. These algorithms are easy to program, are more likely to find the global optimum and are excellent at solving design problems with discrete design variables or severe numerical noise.

The Particle Swarm Optimisation (PSO) method is a simplified social model based on swarming theory (Venter and Sobieszczanski-Sobieski, 2002). PSO is based on the phenomenon of a school of fish adapting to its environment in the swarm:

$$\mathbf{x}_{q+1}^i = \mathbf{x}_q^i + \mathbf{v}_{q+1}^i \Delta t \quad (3.2.1)$$

\mathbf{x}^i marks the position of the particle or design solution, q is the iteration number, \mathbf{V}^j the velocity vector and Δt the incremental movement size. Upon initialisation of optimisation, the particles are randomly distributed over the solution space. The velocity vector is defined as follows:

$$\mathbf{v}_{q+1}^i = w\mathbf{v}_q^i + c_1 r_1 \frac{\mathbf{p}^i - \mathbf{x}_q^i}{\Delta t} + c_2 r_2 \frac{\mathbf{p}_q^g - \mathbf{x}_q^i}{\Delta t} \quad (3.2.2)$$

r_1 and r_2 are random numbers between 0 and 1. \mathbf{P}^i is the best position found by particle i . \mathbf{P}_q^g is the best position found by collective swarm at iteration q . W is the inertia of the particle. C_1 and C_2 are two trust parameters.

The inertia of the particle controls the degree of exploration of the algorithm. Larger values of inertia result in more global behaviour of the particle, while smaller values encourage local behaviour. The two trust parameters indicate how much confidence the particle has in either itself or the swarm. C_1 indicates confidence in self, C_2 indicates confidence in the swarm. This is evident by their placing within equation (3.2.2). Selecting a C_1 value greater than C_2 leads to greater trust in the particle self. In this optimisation project, this meant that the design was more likely to converge to a local optimum. As regards the inertia parameter, tasks with lower inertia values also tended to exhibit more local convergence behaviour.

3.3 VisualDOC Software

The VisualDOC software is an optimisation tool designed by the Vanderplaats R&D organisation. It was a program designed to be compatible with any analysis and implement mathematical optimisation algorithms in any design problem. Essentially, there are five major parts to the VisualDOC software: the database, the design modules, graphical user interface (GUI), applications programming interface (API), and the response program interface. The database provides the primary communication between the components, the GUI allows the user involvement in the programming process, the API handles the communication between the application process and the design modules contain the programming of the optimisation algorithms.

4 DESIGN APPROACH

In this project, a wind turbine blade design has been supplied by the CSIR (Denton, 2003) and the ambition has been to improve on this design's performance using optimisation techniques. Improvement on the existing design was rated in terms of the Coefficient of Power (C_p) produced by the wind rotor. Additionally, the wind rotor would be designed to follow a performance curve within a windspeed range. The performance curve was modelled to replicate the reference Weibull windspeed distribution such that the average performance over the range of windspeeds would be optimised, while still allowing higher than average performance at those windspeeds which occur more frequently.

To simplify analysis time and complexity, the three-bladed wind rotor was simulated as a single blade with four radial stations. Such a simplification of the wind rotor model was deemed to provide sufficient accuracy after comparison with experimental results from the CSIR reference design (Chapter 5). The solution strategy first regarded the two-dimensional optimisation of the airfoil profiles used at the radial stations. Thereafter, the three-dimensional geometric features of the full blade, such as chord length and pitch angle distribution, were optimised. Four airfoil profiles were optimised at the radial stations. These were selected along the rotor radius: the root station at 20% radius, mid station at 50%, semi at 75% and tip at 95%.

The following chapter sets out the method used for optimisation of the full wind rotor and each of the four airfoil profiles. The methodology followed was adapted from wind rotor and optimisation designs found in literature. The methodology was further dictated by the constraints of the resources available.

4.1 Rotor Design Method

As mentioned, the wind rotor is approximated as a simplified model so as to streamline the optimisation process. The model was simplified by choosing some geometric characteristics of the rotor as constants and others as design variables. A constant rotor radius and constant rotational speed are selected according to the reference design. A design windspeed range is selected between 5 and 7 m/s. Four airfoil profiles are optimised at four separate radial stations along the blade. The chord length and pitch angle distributions along the blade become the design variables for the wind rotor optimisation. These rotor design variables are modulated to achieve the peak aerodynamic performance possible for the rotor in the design windspeed range. The Coefficient of Power (C_p), derived in Chapter 2.1, measures this aerodynamic performance at a single windspeed. However, the rotor performance over the design windspeed range is quantified by the measure C_{pobj} , which equals the weighted sum of the C_p at each windspeed. Thus the problem is formulated with a single design objective. The weighting applied to the C_p distribution is deduced from the reference Weibull wind distribution. The Weibull distribution is used in meteorological surveys to predict the probability of certain windspeeds occurring and was applied to the design windspeed range - 5 to 7 m/s. Calculation of this distribution's applicability to South African wind conditions is contained within appendix A.3.2. The resultant weighting of this distribution relative to the windspeed range is shown in Figure 4.1.1.

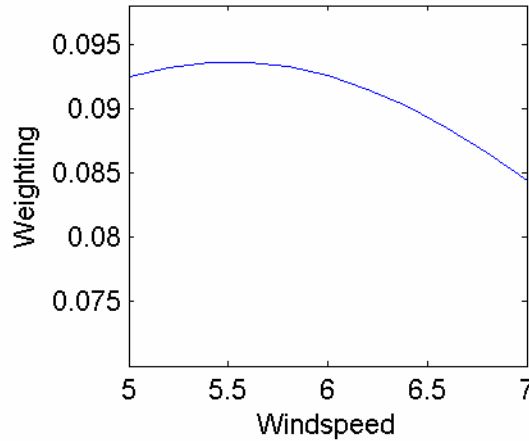


Figure 4.1.1: Weibull weighting distribution

A schematic of the three-dimensional rotor design approach is displayed in Figure 4.1.2. The optimiser, VisualDOC, initialises the first set of design variables - chord length and pitch angle distribution. These values are read into a program in Matlab. The angles of attack and Reynolds numbers for the specific design variables are calculated. The corresponding two-dimensional aerodynamic characteristics are interpolated from data files for the optimised root, mid, semi and tip profiles (these data files are constructed beforehand using XFOIL). The Matlab program uses BEM theory to calculate the resultant rotor power output (C_p) and the optimisation objective function ($C_{p,obj}$). The resultant values are calculated via iteration within the BEM program to ensure that the correct values for the axial and tangential induction factors are found.¹ VisualDOC then imports the calculated objectives and constraints, rates them and adjusts the design variables for use in the next iteration. Setting up of the next iteration's design variables is dependent on the optimisation method selected.

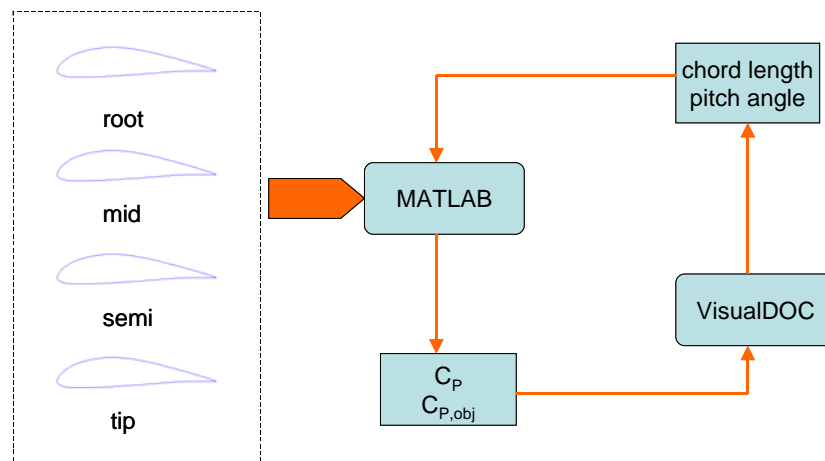


Figure 4.1.2: Three-dimensional Design Approach

¹ As discussed in section 2.2, the BEM theory provides an initial analytical assumption for the degree of retardation of the wind, i.e. the axial and tangential induction factors. This assumption can only be verified once the coefficient of thrust has been calculated. The full BEM calculation is conducted four times so that eventually the tolerance between the initial induction factors and actual induction factors is less than 0.5%.

The optimised airfoil profiles are analysed within XFOIL to produce a range of aerodynamic data files. Each data file contains the angles of attack and corresponding lift and drag coefficients. The range of data covers those Reynolds numbers and angles of attack expected to occur in the wind rotor's operational regime. The BEM program interpolates the aerodynamic data from this data set. An example of such interpolation is shown in Figure 4.1.3. The lift and drag coefficients for an angle of attack of 5.682° are required. As can be seen, these are interpolated from the information at angles of attack of 5° and 6°.

```

XFOIL          Version 6.94
Calculated polar for: midfoilRE350000 Type1

Reynolds number fixed      Mach number fixed
xtrf = 1.000 (top)         1.000 (bottom)
Mach = 0.000              Re = 0.350 e 6      Ncrit = 6.000

alpha      CL      CD
-----
4          0.8955   0.01144
4.5       0.948    0.01173
5         1.0013   0.01211
5.5       1.0542   0.01245
          5.682   1.0732   0.01256
6         1.1065   0.01276
6.5       1.1585   0.01309

```

Figure 4.1.3: Example of XFOIL data file

4.1.1 Objectives and Constraints

In order to obtain peak performance for the wind rotor, it is necessary to obtain high C_p values over the range of windspeeds. According to one-dimensional momentum theory, the closer this value approaches the Betz limit of 16/27, the better the wind rotor is able to extract useful power from the wind. Generally, wind turbines are designed for peak performance at one windspeed. Given the windspeed range of 5 to 7 m/s, the optimiser strives to maximise the C_p values at each stage of the range. The C_p values are summated according to the Weibull weighting to form a single objective. Thus the wind rotor should have peak performance at those windspeeds which occur most often, and less than peak performance at windspeeds which occur less often. The C_{pobj} function is calculated as follows:

The windspeed range is discretised into an eleven-element vector:

$$V_o(1:11) = [5; 5.2; 5.4 \dots 6.8; 7]$$

The Weibull weighting is similarly discretised:

$$f_w(1:11) = [0.0925; 0.932; 0.0936 \dots 0.0866; 0.0844]$$

The aerodynamic performance is calculated according to BEM methods at each windspeed:

$$C_p(1:11) = [0.5290; 0.5317; 0.5341 \dots] \text{ for example}$$

The objective function is calculated as:

$$C_{Pobj} = \sum_{n=1}^{n=11} f_{W,n} C_{P,n} \quad (4.1.1)$$

Furthermore, a constraint on the bound circulation is imposed. The reason being that efficient rotor performance occurs when the circulation over the blade is kept constant (BWEA, 1982). If the bound circulation around each blade element varies considerably, the conservation of angular momentum requires that the vorticity be shed into the wake of the turbine. The resultant expansion in the wake causes reduced airflow through the rotor, and thus lower values of C_p due to reduced airflow through the rotor (BWEA, 1982). The circulation at each radial station was calculated according to equation (4.1.2). ωr is the rotational speed at the radial station. C_l is the local lift coefficient and c is the chord length.

$$circ = \frac{1}{2} \omega r C_l c \quad (4.1.2)$$

The statistical variance of the circulation among the four stations is calculated with each program iteration, and this value constrained to an upper limit of one. Conducting "dummy" optimisation designs and comparing the variance of the resultant designs ascertained this constraint value.

4.1.2 Design Variables

Table 4.1.1 provides a summary of the design variables used during the rotor optimisation design problem. The following section provides motivation for the choice of design variables and constants. Firstly, the rotor radius was selected to be the same as the reference design (Denton, 2003). The power available to be produced by a wind rotor increases proportionally at $V_o^3 R^2$, where V_o is the windspeed and R is the rotor radius. This indicates that the greater the frontal area of the wind rotor, the greater the available power to be extracted from the wind. Thus, given the objective of maximising this power output, the optimiser will undoubtedly attempt to extend the radius of the turbine until some or other limitation has been reached.

Table 4.1.1: Design variables for the Rotor Optimisation

Design Variable		Value	
		min	max
Radius	[m]	3.7	
Rotational speed	[rpm]	80	
Windspeed	[m/s]	5	7
Chord distribution	[m]	0.2	0.8
Pitch angle	[°]		
	root (20%)	13	25
	mid (50%)	-5	11
	semi (75%)	-8	7
	tip (95%)	-11	5

Limitations imposed upon the size of the rotor are due to consideration of either material or manufacturing costs, as well as the overall weight of the rotor and nacelle structure. Since the conclusion of employing a variable radius in the optimisation model is obvious, it is best to optimise for a wind rotor of constant diameter.

The rotational speed of the wind rotor was kept constant and matched the design point rpm for the reference design (Denton, 2003). However, it is most likely that a wind rotor of this size would be connected to a variable speed alternator or DC generator. The reference wind rotor was designed with an optimal tip speed ratio of 6, occurring at a windspeed of 5.5 m/s. This corresponds to 85.17 rpm. The rotational speed for the optimised wind rotor was set at 80 rpm.

Typically, the chord lengths in wind turbine designs tend to taper off from root to tip. This trend takes into consideration structural load and flow conditions over the wind turbine blade (Jackson and Migliore, 1986). Efficient rotor performance occurs when the circulation over the blade is kept constant (BWEA, 1982) and circulation is directly proportional to the product of chord length, lift coefficient and radius (refer to equation 4.1.2). Thus as the radius along the blade increases, the chord length must decrease to maintain constant circulation. Furthermore, the bending moment on the blade decreases from root to tip. A greater chord length directly affects the airfoil profile thickness and provides greater resistance to this bending moment at the root than at the tip.

In this design project, the chord distribution varies exponentially along the length of the blade. Function representation simplifies the number of design variables in the optimisation and furthermore, the exponential trend was deemed the most indicative of existing wind turbine chord length distributions. The chord length is defined by the following function:

$$\text{chord} = a\left(\frac{r}{R}\right)^b \quad (4.1.3)$$

r/R describes the radial position along the length of the blade. Variable a influences the magnitude of the chord length, whereas b defines the shape along the length of the blade. As displayed in table 4.1.1, there are constraints on the minimum and maximum values for the chord length. These constraints ensure a realistic blade design and add to the structural integrity of the wind turbine blade.

The pitch angle or twist distribution determines the angle at which the airfoil profile “sees” the wind. The local angle of attack at a radial point is the difference between the flow angle of the apparent windspeed and the pitch angle. See Figure 4.1.4. As the rotational speed increases from root to tip of a blade, the flow angle decreases. Assuming that the airfoil profiles used at the radial stations experience their peak L/D ratios in a similar angle of attack range, the typical fixed-pitch wind turbine blade will have a pitch angle distribution which is greater at the root of the blade and smaller near the tip (Jackson and Migliore, 1986). The minimum and maximum pitch angle limitations imposed at each radial station ensure that the angles of attack for the root and mid stations fall between 0 and 20°. The angles of attack for the semi and tip stations are designed to fall between 0 and 15°. Knowing the extents of the windspeed range, the rpm and using a sample airfoil, it is possible to estimate the range of flow angles and thus angles of attack to be encountered at each radial station. It can be estimated that stall will occur in the region of 11 to 20° angles of attack. Of course, this is completely dependent on the design

airfoil, but setting an upper limit on the angles of attack ensures that the wind turbine airfoils are not tested too far into the stall region.

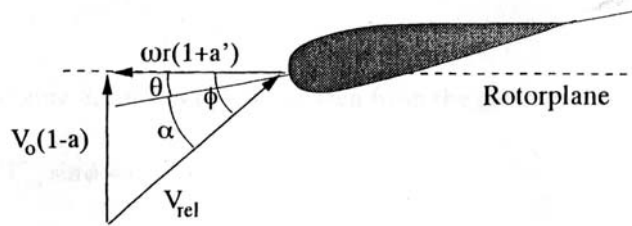


Figure 4.1.4: Velocity diagram at a two-dimensional section of the blade (Hansen, 2000)

4.2 Profile Design Method

The global objective of producing peak C_p values over a broad windspeed range has to be translated into sub-objectives for the design of each airfoil profile. Investigation into wind rotor design literature reveals those aerodynamic properties of airfoils which are beneficial for the overall performance of the wind rotor blade. These properties are set as sub-objectives for optimisation at each radial station. The creation of airfoil profiles was achieved by blending the co-ordinates of base airfoil profiles, thus the influence of each base profile became a design variable in the optimiser. This is a more simple and robust approach for profile design, but was selected to ensure profile generation within XFOIL for each design iteration as well as analysis repeatability in VisualDOC.

The CSIR wind turbine blade used a single airfoil, the RAF-6D, at all radial positions along its span. The CSIR blade was designed with a single operating point in mind for which the RAF-6D catered well. However, for the optimised wind rotor blade different airfoils at the radial positions cater for different operating conditions within the windspeed range. In order to meet the objective of a broad operating range, the airfoil profiles were required to produce high lift-to-drag ratios (L/D ratios) over the corresponding angle of attack range. The L/D ratios are integrated over the angle of attack range to form

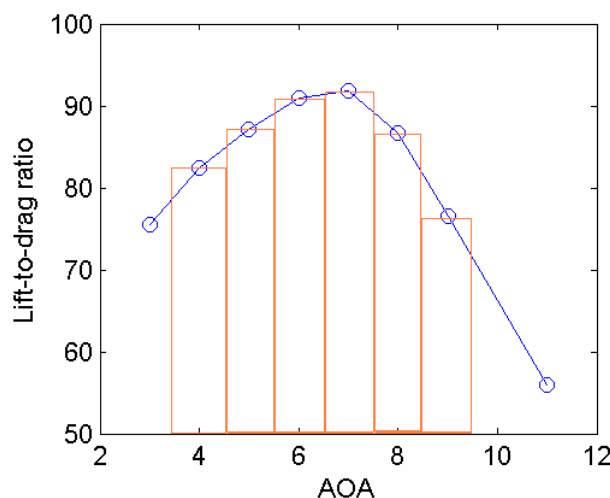


Figure 4.2.1: Method of integration of L/D ratios

a single function, L/D_{area} . This function is maximised within the optimiser. Figure 4.2.1 demonstrates the integration method for derivation of L/D_{area} .

The L/D_{area} function can be maximised in two ways - either by an average high L/D ratio value across the operating spectrum, or by a significant peak which drops away rapidly. However, conducting a number of simplistic optimisation runs with the sole objective of designing an airfoil with a maximum L/D_{area} tended to favour a broad and flat L/D ratio versus angle of attack curve. An airfoil with a peaky L/D ratio profile was not experienced to yield a greater L/D_{area} value. This would only occur if the peak L/D ratio values were radically higher than the average L/D ratio's obtained.

Figure 4.2.2 is a schematic of the basic design method followed for profile design. Firstly, the design method begins with the initialisation of the design variables, variables a_1 to a_5 . These design variables set the percentage influence of each of the five base profiles selected for optimisation. These variables are imported into XFOIL which then combines the five coordinate files and generates a new airfoil. The new airfoil is analysed according to a Reynolds number and angle of attack range, specific to the root, mid, semi or tip stations. The post-analysis aerodynamic characteristics are exported from XFOIL. The L/D ratios and L/D_{area} objective values are calculated within Matlab. The optimiser, VisualDOC, then compares these aerodynamic characteristics to the objectives and constraints set up for the design problem. Depending on the results, the optimiser adjusts the design variables for use in the next iteration.

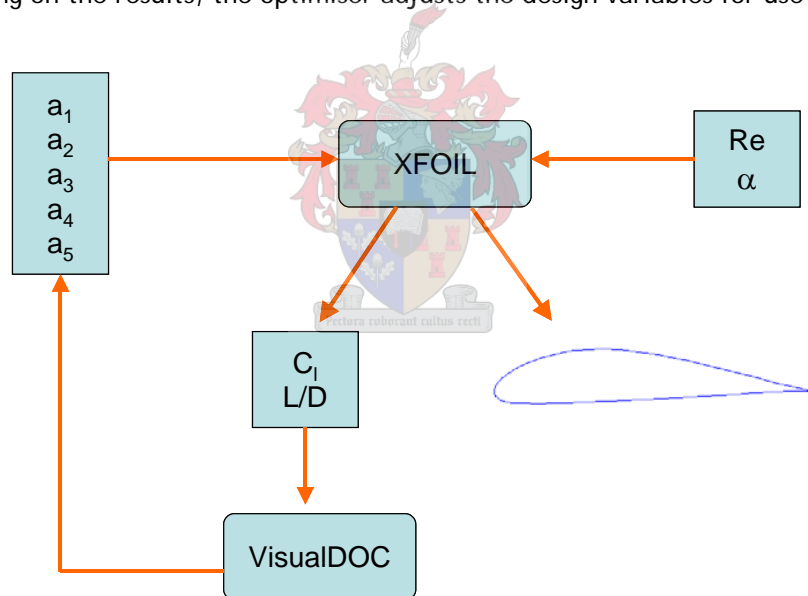


Figure 4.2.2: Two-dimensional Design Approach

The above design method is automated. The three software programs - XFOIL, VisualDOC and Matlab - communicate with each other via text files. The program XFOIL is an iterative analysis program which may or may not converge to a solution or not produce the full range of results necessary for analysis. To combat this problem, there is a binary design variable set up which allows either a pass or fail depending on the quality of results within XFOIL. If a fail response is issued, that iteration is passed and discounted.

4.2.1 Objectives and Constraints

Since the end result of the profile design is to create an airfoil family for efficient wind rotor operation, it is beneficial to ensure that the airfoil characteristics are compatible with one another. This entails setting like-minded objectives and constraints for each airfoil optimised. Essentially, this involves ensuring that there is smooth transition of flow conditions from one station to the next. These flow conditions are mostly influenced by the chord length and pitch angle distribution of the wind rotor, however a further step would be to promote uniform circulation along the length of the blade. Uniform circulation is brought in as a constraint at the rotor design stage, but is further advanced by considering it at the profile design stage. This is achieved by constraining the maximum lift coefficients at each station. Knowing the radial positions and an approximation of the chord lengths at each station allows one to set a value for these constraints, according to equation (4.1.2). Thus the root station $C_{l_{max}}$ is constrained to 1.8, the mid and semi stations constrained to 1.4 and the tip station to 1.2 (Chaviaropoulos *et al.*, 2001).

Root profile

The position of the root profile is at 20% of the blade length. The Reynolds number at which the profile optimisation is conducted is 300,000. This was calculated using the upper limit for the chord length distribution (0.8 m) and the relative velocity seen by the blade at this station. The design range for the angles of attack are 10 - 25°. During start-up conditions of the wind rotor, the rotational velocity is low. Consequently, the relative wind velocity seen by the rotor occurs at larger flow angles. Since the blade elements along the length of the blade are designed for operation at lower flow angles, most of the blade tends to be in near-stall or the high-lift/high-drag performance region. The unique design objective for the root station is to be the main power-producing section of the blade under start-up conditions since it has the smallest angles of attack of all the stations under start-up conditions. The angle of attack range to be used during profile optimisation is selected in the region of 10 - 25°. The maximum lift coefficient $C_{l_{max}}$ is constrained to be less than 1.8 to match the constraint of circulation over the blade.

The base profiles used as design variables in the optimisation are selected to have an average thickness-to-chord ratio of 20%. Thicker airfoils tend to be high-lift airfoils as well as benefiting the structural integrity of the blade. The root section bears most of the structural load exerted on the wind turbine blade. However, the structural calculations contained in appendix A.3 indicate that a thickness-to-chord ratio of 4.6% is sufficient to meet the load conditions on a wind rotor of this size. For this reason, the design constraints on the root profile thickness were not strict.

Mid and Semi profiles

The mid profile is positioned at 50% of the blade radius and the semi profile is positioned at 75%. These profiles are optimised at Reynolds numbers of 350,000 and 380,000 respectively. These Reynolds numbers are calculated in consideration of the expected chord lengths and relative velocities experienced at these stations. The design range for the angles of attack for both profiles is 1 - 15°. This range is broad

and assumed to be representative of the pre-stall region for the profile. The mid profile and the semi profile are the main power-producing regions of the wind rotor blade. These two stations are not affected by hub and tip losses and furthermore have the advantage of an extended torque arm, relative to the root station. Ideally it was set out to generate laminar airfoils which experience slow transition to stall (Jackson and Migliore, 1986) and exhibit high L/D ratios (Spera, 1995). This would increase the operating region of the blade. The design objective for the mid and semi stations is to achieve high L/D ratios over the operating region of the wind rotor. The variable L/D_{area} must be maximised for the angles of attack from 1 to 15°. The maximum lift coefficient is constrained to 1.4.

To further ensure peak rotor performance over a range of windspeeds, the mid and semi profiles need to experience slow transition to stall. Airfoils in stall exhibit strong nose-down pitching moments (Huyer *et al.*, 1996). Since the pitching moment (C_m) is readily available in the output file from XFOIL, it was decided to place a constraint on this aerodynamic property. The mean of the C_m values (C_{mmean}) for angles of attack 1 to 15° was calculated and the absolute value of the result constrained to 0.08. Airfoils known to exhibit the characteristic of slow transition to stall were analysed. It was found that in general their C_{mmean} values are in the region of 0.05. Thus the constraint of 0.08 was declared adequate.

Tip profile

The tip profile is located at 95% span of the wind rotor blade. The remaining 5% of the blade is used for rounding off the blade and it is assumed that the blade tapers to zero thickness. The Reynolds number for optimisation is 400,000. This location of the blade receives particular attention due to its role during stall regulation. In the event of windspeeds much greater than 7 m/s, the wind rotor no longer operates within its design windspeed range. The relative velocities and flow angles are much larger than seen at lower windspeeds. Though turbine runaway is an obvious concern for a stall-regulated turbine, this is unlikely to occur at this windspeed. However, it is ideal to impose stall-regulation measures above this windspeed. To design for stall regulation, the C_{lmax} of the tip profile is constrained to 1.2 and the angle of attack at which the C_{lmax} occurs is also constrained to be less than 13°. These constraints aim to produce an airfoil profile which produces a lift-to-drag ratio characteristic which is useful within a small angle of attack range (1 to 10°) but rapidly drops off as the angles of attack become larger and thus has a breaking effect on the entire rotor. To promote rapid transition to stall the mean nose-down pitching moment constraint is increased to 0.1 where it does not have much influence on the optimisation process.

4.2.2 Design Variables

The strategy for new airfoil generation is a compromise between minimising computational cost and producing accurate, measurable results. Computational cost is directly related to the number of times the aerodynamics program is called for analysis, i.e. the number of function evaluations. To minimise computational cost, a simplified model for rapid generation and rapid analysis of airfoils was created. The number of design variables describing the airfoil was limited. Previous airfoil optimisation research demonstrated the difficulty of airfoil optimisation when the model had been given too many degrees of

freedom (Drela, 2002). The results yielded physically unrealisable airfoils with small-scale irregularities which had no aerodynamic penalty visible to the optimiser. A more simple and robust approach for profile design was selected due to the difficulties of complex geometry creation within optimisation.

The creation of new airfoils is achieved by blending the co-ordinates of base airfoil profiles and the influence of each base profile becomes a design variable in the optimiser. This method was employed by (Vanderplaats, 1979). The airfoil shape at each station is described by the following function:

$$Y = a_1Y^1 + a_2Y^2 + \dots + a_nY^n \quad (4.2.1)$$

Y is a vector containing upper and lower coordinates. The Y^n define shape functions which represent the base airfoil profiles. a_1, \dots, a_n apply different weightings to the shape functions such that the summation results in the coordinates of one profile.

The base profiles were selected from a sample of airfoils which are widely used within the wind turbine industry. The sample of widely used airfoils was analysed at a reference Reynolds number and the resultant objective and constraint values calculated. The sample of profiles could thus be rated in order of compatibility with the specific requirements at each radial station. The top-ranking profiles were selected to form part of the set of base profiles for optimisation at each radial station. Five base profiles were used at each station. Usually three or four were selected for their performance criteria; however, the remaining would be selected for their exceptional geometry. Experience gained thus far has revealed that sample diversity within optimisation often breeds the best design.

Blending a number of airfoils grants the user the assurance that the design will be physically realisable. Furthermore, this method is repeatable and thus forms a basis for comparison with the other similarly generated airfoils. XFOIL has an interpolation function which blends the coordinates of the airfoils. More details of this interpolation function are contained in appendix A.1.



5 VERIFICATION OF PROGRAM

The BEM theory laid out in chapter 2.2 has been programmed in a Matlab mfile and included into the automated design process. The BEM program code is displayed in appendix A.4. This method of coding was specifically selected to ease the optimisation process. However, the BEM program results must be verified to ensure that the final design is feasible in reality, outside of the computational world. Verification is achieved by comparing the BEM power output calculations with experimental measurements for an existing wind turbine blade. These experimental measurements are obtained by testing the wind turbine in a wind tunnel.

Two verification sources were chosen - the Council for Scientific and Industrial Research (CSIR) and North-West University (NWU). Both organisations designed their own small-scale, stall-regulated wind turbines and tested the final product in a wind tunnel. With permission, these experimental results were obtained as well as the design specifications of the respective wind turbine blade. With this information, it was possible to analyse both wind turbines using the BEM program and compare the results to the available wind tunnel test data.

5.1 CSIR experimental data

The CSIR used a scaled model of their wind turbine in a 7.5 m by 6.5 m cross-section wind tunnel. The model used had a radius of 1.205 m, as opposed to the actual turbine which had a radius of 3.7 m. The verification and experimental results were non-dimensionalised for comparative purposes. The turbine hub was positioned at the wind-tunnel centreline and faced directly into the wind. The windspeed and rotational speed of the wind rotor was measured, as well as the power output, via a torque transducer. These readings were used to calculate the coefficient of power (C_p) values of the wind rotor, relative to the tip-speed ratio. The wind-tunnel walls have an effect on the performance of the wind turbine in the wind-tunnel. The wind-tunnel velocity is artificially increased by the presence of the model. To account for this, a velocity correction is calculated and accounted for in the measurements (Denton, 2003).

The CSIR wind turbine was analysed at the four radial stations - root, mid, semi, tip. The measured windspeeds and rotational speed, as well as the chord length and pitch angle distributions were imported into the BEM program. Before the verification exercise, the RAF-6D airfoil was analysed in XFOIL to create a database of aerodynamic characteristics to be used in the BEM program. It should be noted that the BEM program was set up to analyse the experimental data in exactly the same manner that it analysed the optimisation rotors.

In Figure 5.1.1, C_p versus tip-speed ratio (λ) is plotted for the experimental data and three sets of analytical data - iter 2, iter 3, iter 4. These indicate how many times the solution was iterated within the BEM program. "iter 2" indicates two iterations, and so on. Recall from the BEM theory that it is necessary to iterate the solution to obtain the correct value for the induction factors. These are assumed in the first iteration.

As is evident in Figure 5.1.1, as the number of iterations of the solution increases, the analytical results approach the experimental results. "iter 2" only correlates with the experimental data between X of 5 and 6. "iter 4" preserves an average accuracy of 1.913% between X of 6 and 7. As X drops lower than 6, the discrepancy between experimental and analytical rises to 4.63% and finally to approximately 10%. As X increases from 7 to 9, the discrepancy increases first 3.52% and then rapidly to 30%. After this point there is very little correlation between the experimental and analytical data. This is probably because the rotor is experiencing stall or close to stall conditions (as noted by the decreasing C_p values). XFOIL is known to be less accurate under these conditions. Furthermore, the effects of Coriolis' and centrifugal forces are more prominent at higher tip speed ratios, and an accurate model for these was not employed.

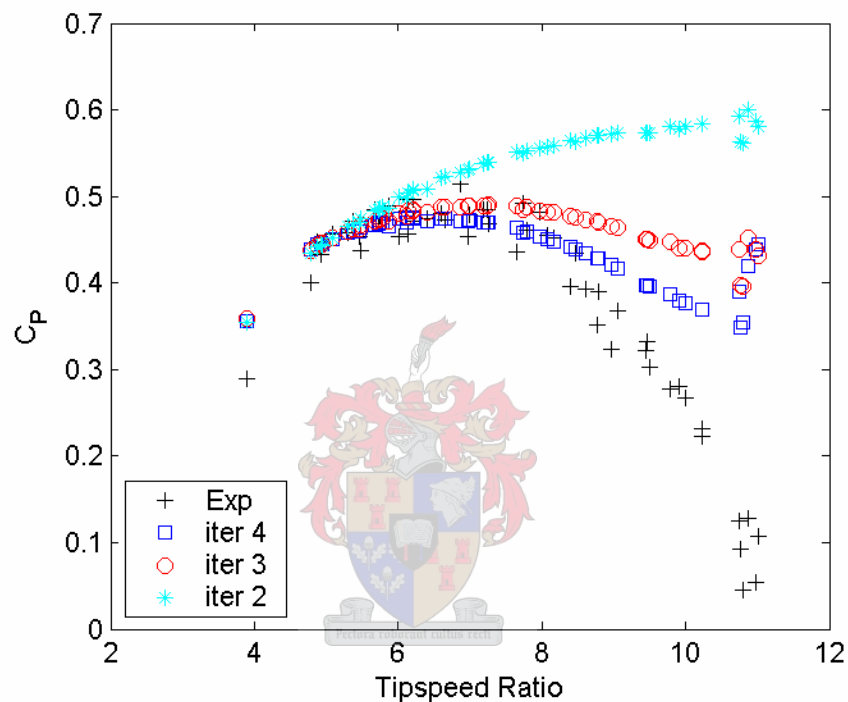


Figure 5.1.1: C_p plot of analytical data vs. experimental data

In the CSIR report, the experimental results were compared using their own analytical model. Their analytical results showed a similar trend to the results represented here, since both were based on the BEM theory. The analytically predicted and the measured results correlated well between X equal to 5.5 and 6.5. Outside of this region, the predicted data was greater than the measured. Their own code tended to over-predict the C_p values by similar margins (Denton, 2003).

The discrepancy between analytical and experimental results can be further attributed to errors in wind-tunnel speed measurements, and the manufacture of the actual blade. The blade is not completely rigid, thus aeroelastic effects cause bending and twisting of the blade as it experiences loading. Though not excessive, this can result in flow conditions other than those predicted by the mathematically accurate model.

5.2 NWU experimental data

The North West University (NWU) also designed and tested a small-scale wind turbine blade. Their original blade was small enough to undergo wind-tunnel testing without having to scale the model down. They rigged their three-bladed rotor to an alternator, measured the windspeeds and power produced. The experimental data provided was taken over four discontinuous days (Bosman, 2003).

Unfortunately, no rpm or torque readings were taken during the experiment. In order to determine the power produced analytically, it is necessary to know the rpm corresponding with the instantaneous windspeed reading. It was possible to interpolate the rpm readings from an analytically determined blade curve map (Figure 5.2.1). Using a power value generated at a known windspeed, the rpm reading could be read from the blade curves. However, this immediately brings the order of accuracy of this verification exercise down. Naturally, the wind rotor does not quite respond to the windspeeds predicted in the blade curve map. Unfortunately, this was the only source of rotational speed information. Thus, the measured windspeeds and interpolated rotational speeds were imported into the BEM program and the experimental and analytical power output compared (Figure 5.2.2).

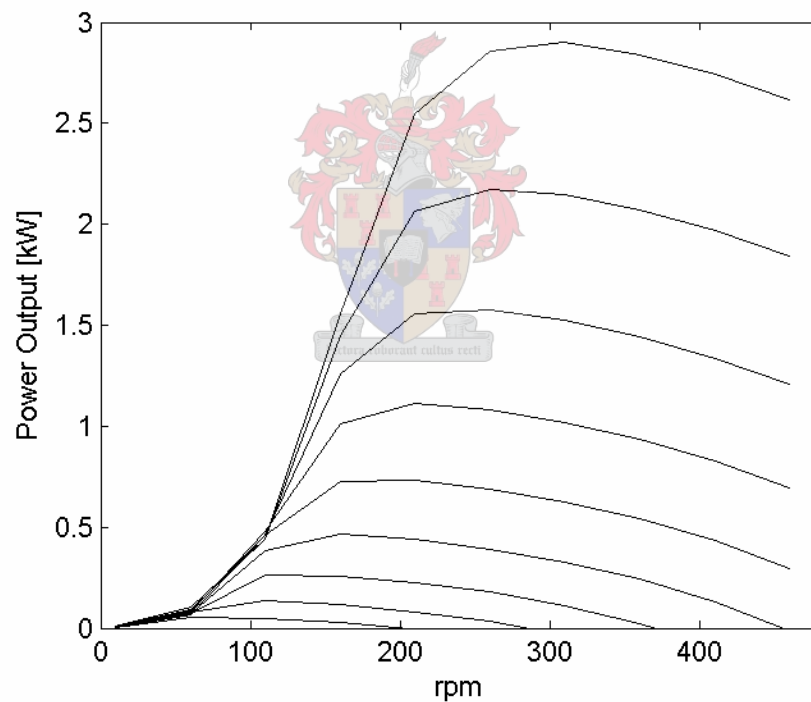


Figure 5.2.1: Analytically determined blade curve map for NWU blade

The experimental power output was measured using an alternator. The power output versus windspeed is plotted in Figure 5.2.2. As expected, there is considerable fluctuation in the experimental readings compared to the single-line readings of the analytical BEM code. Good correlation between experimental and analytical data exists at windspeeds below 6 m/s. The correlation discrepancy is approximately 4% between 4 and 5 m/s. This rises to 14% between 5 and 7 m/s. Thereafter, the analytical over-prediction is quite large.

The discrepancy between the experimental and analytical data can be largely attributed to the inaccurate means of obtaining rpm readings. Furthermore, the theory employed in the BEM code does not accurately model hub and tip losses. Nevertheless, for there to be good correlation, the average difference need only be less than the standard deviation in the experimental data. This is indeed the case up to about 6 m/s.

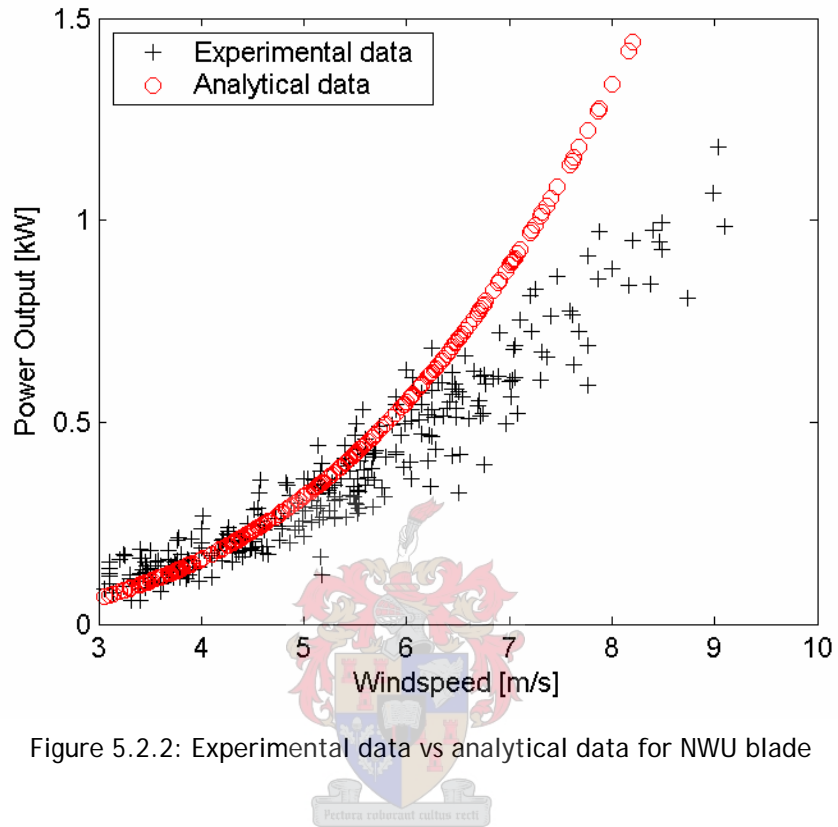


Figure 5.2.2: Experimental data vs analytical data for NWU blade

6 NEW BLADE OPTIMISATION

6.1 Profile Optimisation

Before commencing design of the three-dimensional geometry of the wind rotor, the airfoil profiles at each of the four stations along the wind rotor blade - root, mid, semi, tip - were developed. These airfoils were designed using optimisation methods and the two-dimensional analysis program XFOIL. The optimisation program, VisualDOC, was used to drive XFOIL to create airfoil profiles with optimum characteristics. The aerodynamic characteristics of importance were the maximum coefficient of lift (C_{lmax}), the angle of attack where C_{lmax} occurs, and the summated lift-to-drag ratio (L/D_{area}). These aerodynamics characteristics were set as the objectives and/or constraints for the optimisation of the airfoils.

The optimised airfoils at each radial station were blended from the coordinates of a set of base airfoil profiles. These base profiles were selected from a larger sample of airfoils which have wide application within the wind turbine industry. They were selected to match the objectives and constraints set for each blade section.

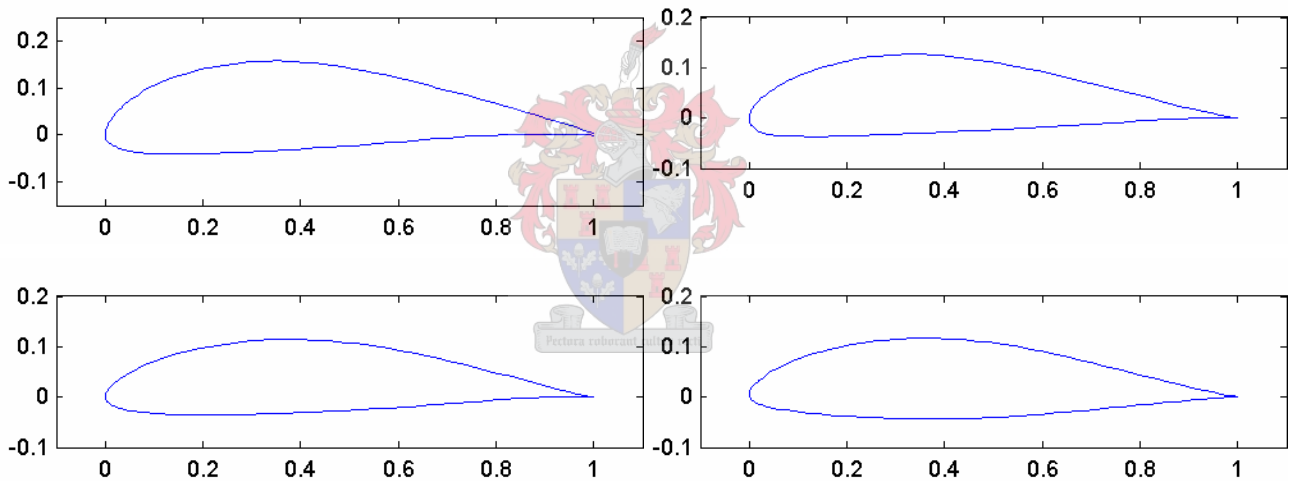


Figure 6.1.1: The optimised airfoils - at the top are the root and mid foils, bottom are the semi and tip

The final airfoil designs had different C_{lmax} constraints for each station, which decreased from root to tip. Consequently, the maximum camber of each optimised airfoil decreases from root to tip. The high-lift root profile is 50 to 60% thicker than the other optimised profiles. The mid profile has a rounded nose for efficient operation over a range of angles of attack. Though the semi profile was also designed with this requirement, this design has a sharper nose. As expected, the tip airfoil has a sharp nose for rapid transition to stall.

The following sections present the optimisation results for the profiles at four stations of the wind rotor blade. Appendix A.2 contains information on the geometric characteristics (such as maximum thickness and leading edge radius) of the base profiles for all the stations.

6.1.1 Root Profile

The root station was chosen to be the main power-producing section of the blade under start-up conditions, since it has the smallest angles of attack of all the stations under these conditions. Thus it was necessary to generate high lift coefficients at angles of attack in the transition-to-stall region. The original objective was to maximise the L/D ratios over the design range of angles of attack, however the resultant optimised root foils yielded low values of C_{lmax} . The design objective was thus changed to maximise the peak lift coefficient for the profile.

- Position of profile is at 20% of blade radius
- Reynolds number: 300,000
- Design range for angles of attack: 10 - 25°
- Objective of optimisation:
Maximise C_{lmax}
- Constraints:
Maximum lift coefficient, $C_{lmax} < 1.8$

The base profiles are displayed in Figures 6.1.2 to 6.1.8 and the resultant profile in Figure 6.1.9. A comparison between the base profile aerodynamic characteristics and those of the optimised foil are displayed in table 6.1.1. To be noted is that the optimised airfoil outperforms the base profiles in terms of the objective.

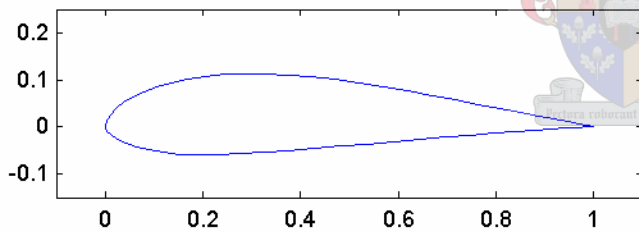


Figure 6.1.2: Foil 1 - mh102

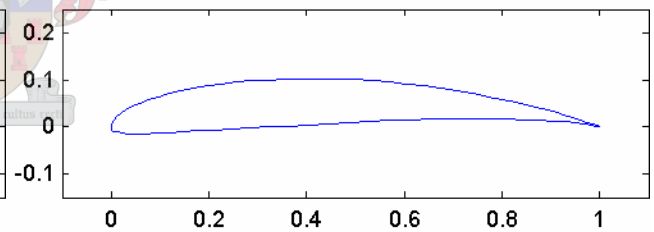


Figure 6.1.3: Foil 2 - sg6043

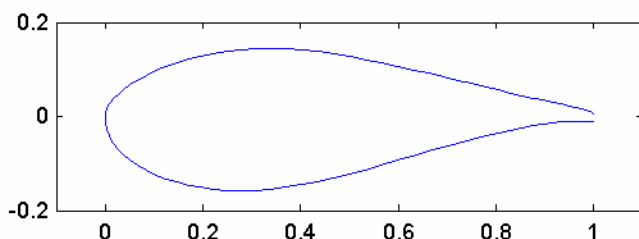


Figure 6.1.4: Foil 3 - ah94w301

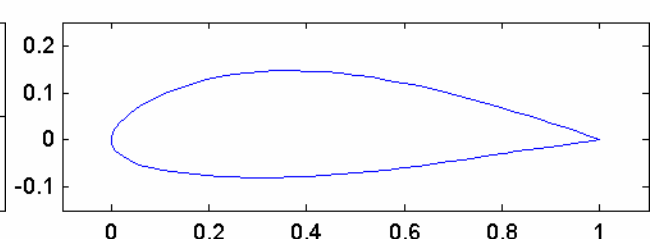


Figure 6.1.5: Foil 4 - fx83w227

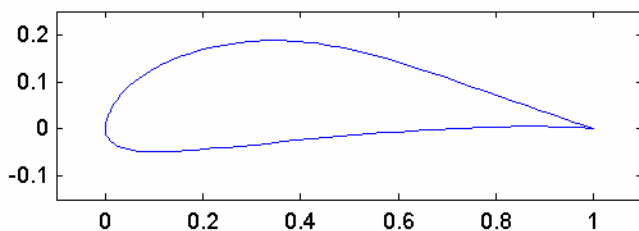


Figure 6.1.6: Foil 5 - rxcamxtx

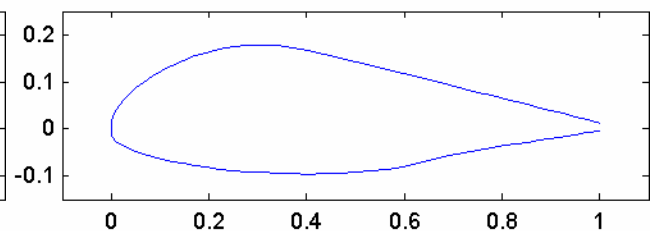


Figure 6.1.7: Foil 6 - fx77w270s

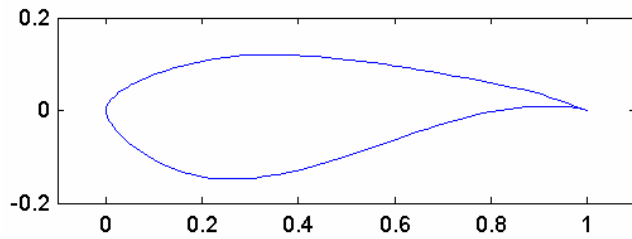


Figure 6.1.8: Foil 7 - Somer's root foil

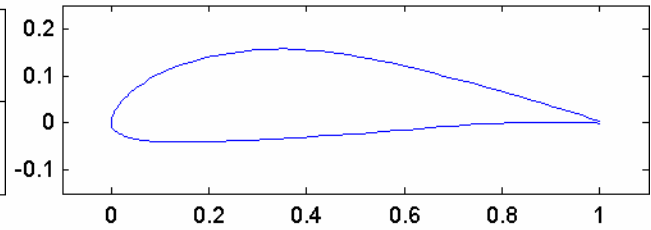


Figure 6.1.9: Optimised root profile

Table 6.1.1: Aerodynamic characteristics of the base profiles and root airfoil

Profile	C_{lmax}	@ α	L/D_{area}	L/D_{max}	@ α
		[°]			[°]
foil 1	1.4416	14	139.0013	78.8367	8
foil 2	1.6583	16	123.5816	113.3957	4
foil 3	1.4518	14	116.6781	59.9377	9
foil 4	1.3361	16	144.1236	61.2254	8
foil 5	1.6260	25	133.9174	69.4222	5
foil 6	1.3003	11	61.2802	40.8514	11
foil 7	1.2838	25	98.4928	62.8127	9
optim foil	1.7690	13	151.6311	78.3169	10

Though seven airfoils were chosen as the sample base for design of the root profile, the optimiser was programmed to use only five base profiles in each optimisation task. Badly performing profiles would be replaced with others from the sample base. Initial examination of Figures 6.1.2 to 6.1.9 reveals that the base profiles are quite diverse in shape. Though some shapes are similar, there are considerable differences in the camber and airfoil contours. These base profiles were selected for their high C_{lmax} ; however, foils 6 and 7 were selected to add geometric diversity to the sample base. At first examination, the optimised root airfoil seems similar to foil 5. However, the optimised foil is thinner, with a lower camber and has a sharper nose. In fact, the final airfoil composition included 33% of foil 2, 46% of foil 5 and 21% of foil 6.

There are five successful optimisation tasks discussed in this section. The details of the optimisation methods used, number of analysis calls and analysis times are displayed in table 6.1.2. Tasks 1 to 4 made use of the gradient optimisation method, SQP. This is a robust optimisation tool which allows an accurate investigation of the solution space within a relatively short number of iterations. Task 5 used the non-gradient method, PSO. The analysis time for this task was much greater than the SQP tasks. Though a more thorough technique, it does not always yield the better solution, as is evident here. The profile created in task 4 using the SQP method proved to be the best profile of all the tasks, yielding the highest C_{lmax} and the second highest L/D_{area} . Task 1 was set up with the original objective of optimising L/D_{area} and consequently creates an airfoil with the highest L/D_{area} value. However, the L/D_{area} is only marginally higher than those values obtained in tasks 2 to 5, which were optimised for maximum lift coefficient. The objective values from tasks 2 to 5 are very similar even though different design variables and optimisation methods were used.

Table 6.1.2: Results from five optimisation tasks

Task no	C_{lmax}	@aoa [°]	L/D _{area}	Optimisation Method		ana calls	ana time
Task 1	1.4884	19	154.6814	SQP	rel step 0.1	59	31.7 min
Task 2	1.7592	12	149.0293	SQP	rel step 0.05	52	29.5 min
Task 3	1.7682	13	147.8942	SQP	rel step 0.05	32	17.5 min
Task 4	1.7690	13	151.6311	SQP	rel step 0.05	59	33.1 min
Task 5	1.7679	13	151.3352	PSO	C1 1.5, C2 2.5	1500	13hr 26.6 min

Table 6.1.3: Initial and resultant percentage composition for each task

Task no	foil 1	foil 2	foil 3	foil 4	foil 5	foil 6	foil 7
Task 1	0.200	0.400	0.160	0.022	0.218	-	-
Task 2	0.200	0.400	0.160	-	0.218	0.022	-
Task 3	0.150	0.128	0.361	-	0.181	0.181	-
Task 4	-	0.128	-	0.361	0.181	0.181	0.150
Task 5	-	-	-	-	-	-	-
Task 1	0.528	0.017	0	0.052	0.402	-	-
Task 2	0	0.295	0	-	0.689	0.016	-
Task 3	0	0.396	0	-	0.349	0.254	-
Task 4	-	0.328	-	0	0.461	0.211	0
Task 5	-	0.318	-	0	0.535	0.147	0

In table 6.1.3, the base profile combinations and their percentage of the final airfoil for each task are presented. The initial percentage compositions are also included. The blanks indicate which foils were not used for the corresponding optimisation task. The initial percentages for task 5 are all shown as blank since the PSO method does not start from an initial position within the solution space but instead takes random samples.

Examining the final percentage compositions, it is clear that the most influential or most used airfoils are foils 2 and 5. These featured predominantly in tasks 2 to 5, even when their initial percentage values were low (such as task 3). Foils 1 and 5 mostly influence the final airfoil in task 1, however this task had a different objective and is thus difficult to compare with the other tasks. Foils 2 and 5 were selected due to their good aerodynamic characteristics. Their C_{lmax} values are in the region of 1.6 while the rest of the base foils are in region of 1.3 to 1.4. Naturally, the camber of these foils is also the highest of the sample base. In both tasks 2 and 3, the influence of foils 1 and 3 are lowered to zero. Consequently, in tasks 4 and 5 the non-performing foils 1 and 3 were replaced with foils 4 and 7. The influence of these foils was also reduced to zero. The aerodynamic characteristics of these four foils are not particularly bad, and yet the optimiser drives their influence to zero. In fact, foil 6 which features in tasks 3, 4 and 5 has a low C_{lmax} and the lowest L/D_{area} value. Examining the geometric features of these foils (Appendix A.2), foil 6 has a reasonably high camber which occurs further forward along the X axis of the foil than the others. Given the optimisation objective of maximising C_{lmax} , the lower-cambered foils 1, 3, 4, 7 were systematically isolated from the various optimisation tasks.

Tasks 4 and 5 used different optimisation methods to one another, but resulted in similar design variables. This is an indication of a good solution. Foil 5 again took up the highest percentage of the final airfoil, along with 30% granted from foil 2. The optimiser tended to lend the majority of the influence in the final airfoil from three design variables, as opposed to five.

Figures 6.1.10 and 6.1.11 plot the lift coefficients and L/D ratios for each of the design tasks and provide confirmation of the most successful optimisation task. The trend of the lift coefficient vs. angle of attack is similar across tasks 2 to 5. These all achieved their C_{lmax} values at angles of attack of 12° to 13° . Though task 2 seems to yield a favourable lift coefficient trend, examination of Figure 6.1.11 shows that its L/D ratios are not as favourable.

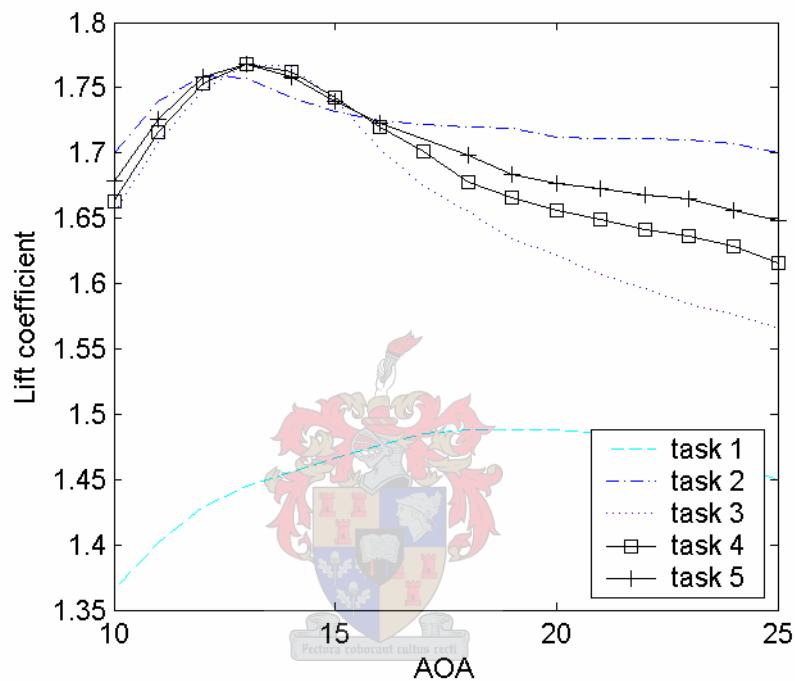


Figure 6.1.10: Lift coefficient vs. angle of attack

The objective for task 1 was to optimise the L/D_{area} . As can be seen in Figure 6.1.11, the L/D ratio versus angle of attack curve for task 1 is only slightly different than that achieved by the other tasks. However, according to Figure 6.1.10, task 1 achieves much less favourable lift coefficients. It is not evident why the original objective of optimising L/D_{area} did not work. Possibly the gradient methods employed had too small a search step size to be able to see the benefit of a higher lift coefficient airfoil to the L/D_{area} value. Further investigation of the solution space revealed an area of airfoils with C_{lmax} in the region of 1.65 but with L/D_{area} values in the region of 122 - lower than the L/D_{area} value obtained in task 1. The optimiser would surely have encountered this minimum solution area and then decided to rather launch a search path in the other direction. Nevertheless, tweaking of the optimisation parameters did successfully produce a root profile to match the desired objectives.

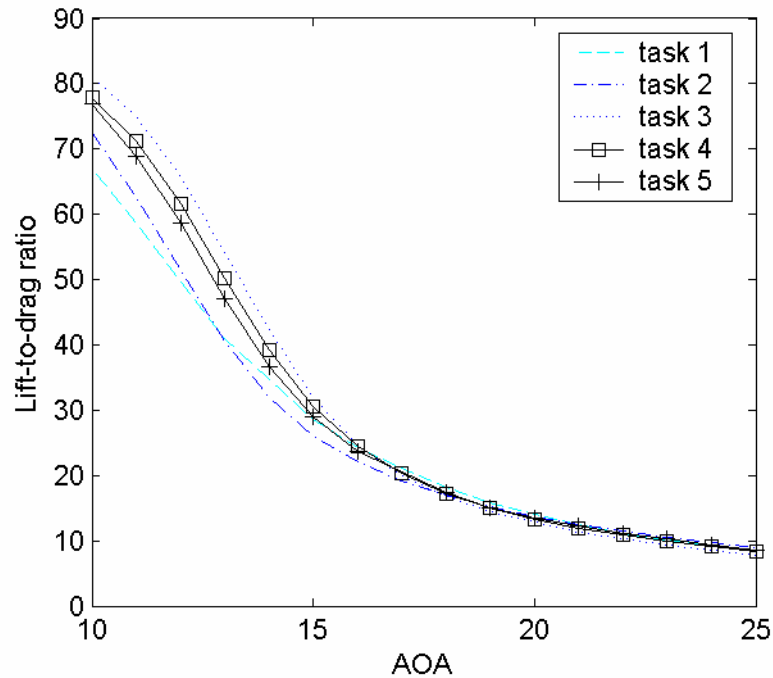


Figure 6.1.11: L/D ratio vs. angle of attack

6.1.2 Mid Profile

Along with the semi station, the mid station represents the main power-producing region of the wind rotor blade and thus it is important that the airfoils at these locations experience slow transition to stall. The design goal for both these stations was to achieve high L/D ratios over a broad operating region. The base profiles were selected to have maximum L/D_{area} values, provided that they met the C_{lmax} constraint. The base profiles selected for optimisation and the optimised mid profile are displayed in Figures 6.1.12 to 6.1.18 and their characteristics are contained in table 6.1.4. Foils 3 and 6 were chosen for their geometric diversity.

- Position of mid profile is at 50% of blade radius
- Reynolds number: 350,000
- Design range for angles of incidence: 1 - 15°
- Objective of optimisation:
Maximise integral of lift-to-drag ratios for range of angles of incidence

$$obj = \int_{\alpha_0}^{\alpha_1} \frac{C_l}{C_d} d\alpha \quad \begin{array}{l} \alpha_0 = 1^\circ \\ \alpha_1 = 15^\circ \end{array}$$

- Constraints:
Maximum lift coefficient, $C_{lmax} < 1.4$
Mean nose-down pitching moment, $C_{mmean} < |0.08|$

At first glance, the optimised mid profile seems unique to the other base foils. It has a similar nose to foil 2, a concave trailing pressure surface indicative of foil 3 and perhaps influence from foil 1 as

regards the lower surface. In truth, the percentage breakdown of the optimised mid profile is 48% of foil 1, 27.5% of foil 3 and 22.5% of foil 5. There is zero influence from foil 2 and almost zero from foil 4.

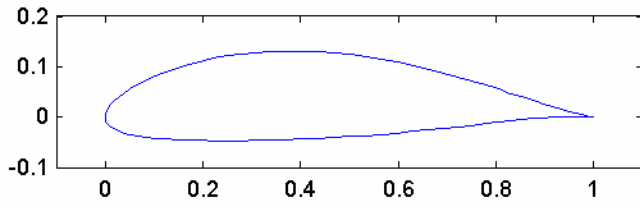


Figure 6.1.12: Foil 1 - fx84w175

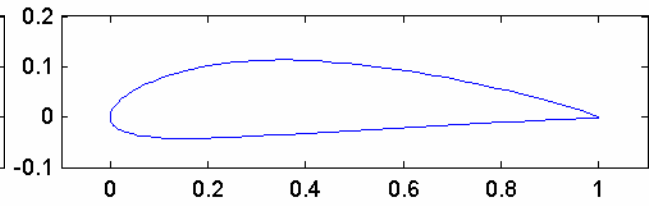


Figure 6.1.13: Foil 2 - naca 4415

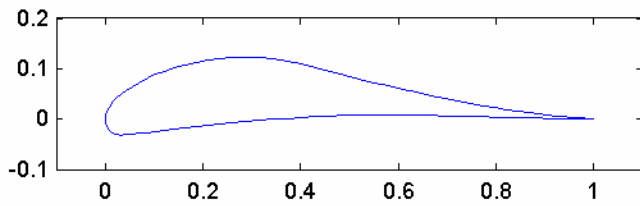


Figure 6.1.14: Foil 3 - Inv109a

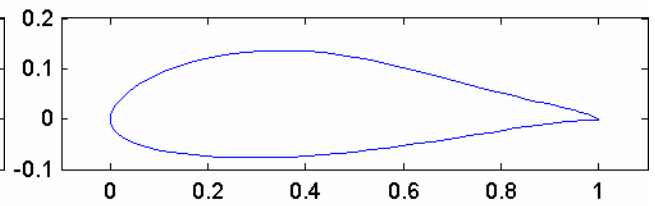


Figure 6.1.15: Foil 4 - ah93w215

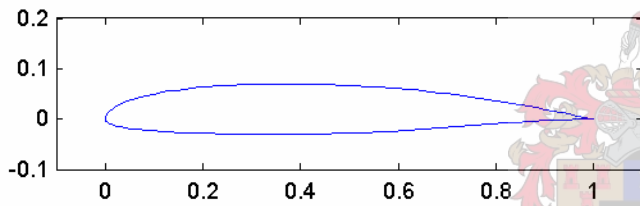


Figure 6.1.16: Foil 5 - sg6041

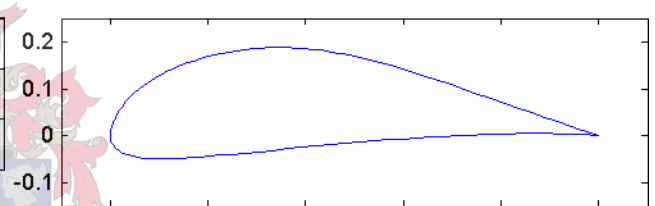


Figure 6.1.17: Foil 6 - rxcamxtx

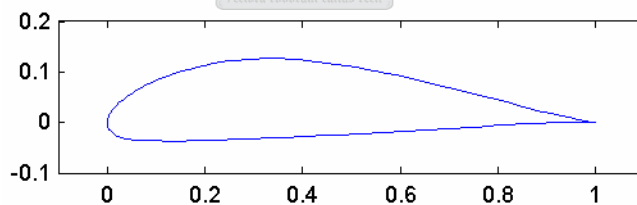


Figure 6.1.18: Optimised mid profile

Table 6.1.4: Aerodynamic characteristics of base profiles and mid airfoil

Profile	L/D_{area}	C_{lmax}	@ α_{oa} [°]	C_{mmean}	L/D_{max}	@ α_{oa} [°]
foil 1	939.618	1.366	12	0.082	90.998	7
foil 2	976.121	1.486	14	0.087	89.569	7
foil 3	936.470	1.738	13	0.049	93.674	11
foil 4	790.508	1.326	15	0.041	76.786	9
foil 5	816.210	1.324	15	0.041	73.420	3
foil 6	782.682	1.538	12	0.121	76.837	5
optim foil	988.316	1.399	12	0.066	95.288	9

The design problem was solved using different optimisation methods as well as various initial design variables. Two gradient methods and a non-gradient method were employed. The results of six successful tasks, as well as task details, are presented in table 6.1.5. The resultant airfoil compositions are displayed in table 6.1.6. The objective values and final airfoil compositions are quite varied across optimisation tasks 1 to 5. The MMFD method of task 4 yielded the lowest objective results while the PSO method yielded the highest. MMFD does not model the solution space as accurately as the SQP method. Consider task 2 which used the SQP method and had fewer analysis calls than the MMFD, however it obtained a better objective. PSO conducts many iterations of the solution - 1850 iterations as opposed to approximately 50 of the SQP method. For the range of base profiles selected, the optimiser struggled to keep the mid profiles' C_{lmax} values below the constraint of 1.4. The gradient methods had too large a tolerance set on the constraint boundaries, thus only the PSO method converged to a solution closer to the constraint boundary.

Table 6.1.5: Results from five optimisation tasks

Task no	L/D _{area}	C _{lmax}	C _{mmean}	Optimisation Method	ana calls	ana time
Task 1	984.621	1.414	0.070	SQP rel step 0.1	54	30.0 min
Task 2	954.095	1.438	0.072	SQP rel step 0.01	24	13.1 min
Task 3	936.613	1.420	0.070	SQP rel step 0.1	71	39.3 min
Task 4	903.248	1.432	0.057	MMFD rel step 0.1	41	23.9 min
Task 5	988.316	1.399	0.066	PSO C1 2, C2 2.5	1850	17hr 7 min
Task 6	979.900	1.401	0.075	PSO C1 2, C2 2.5	1433	12hr 42 min

Table 6.1.6: Initial and resultant percentage composition for each task

Task no	foil 1	foil 2	foil 3	foil 4	foil 5	foil 6
Task 1	0.100	0.090	0.081	0.073	0.656	-
Task 2	0.100	0.360	0.054	0.243	0.243	-
Task 3	0.019	0.482	0.224	0.000	0.275	-
Task 4	0.100	0.090	0.081	0.073	0.656	-
Task 5	-	-	-	-	-	-
Task 6	-	-	-	-	-	-
Task 1	0.556	0.020	0.203	0.111	0.109	-
Task 2	0.100	0.369	0.053	0.239	0.239	-
Task 3	0.057	0.339	0.006	0.380	0.218	-
Task 4	0.100	0.090	0.089	0.072	0.649	-
Task 5	0.482	0.000	0.275	0.019	0.224	-
Task 6	0.661	0.000	0.000	-	0.177	0.163

Examining the results in table 6.1.5, there is essentially only correlation between the tasks 1, 5 and 6. Task 2 used a much smaller relative step size and converged to a solution quite rapidly. This is probably a local optimum. Task 4 used the MMFD method which has not yielded favourable results in this solution space. Task 3 on the other hand had the same set-up as task 1 except for the initial percentages

of the base foils. Task 3 yields very different results though and seems to be placed at another local optimum in the solution space. Tasks 1, 5 and 6 point to a more likely global optimum.

The optimisation tasks 1 and 5 achieved the highest objective values. Both these tasks allow significant contribution from foils 1 and 3. Foil 1 is quite bulky, with its position of maximum thickness occurring further back along the chord than most of the other base profiles. Aerodynamically, the foil produces a high L/D_{area} value and still adheres to the C_{lmax} constraint. Foil 3 has a high value for maximum camber, as well as a large leading edge radius. The leading edge radius ensures a large operating range for the airfoil. Foil 3 also has a high L/D_{area} value but its C_{lmax} is much greater than the constraint. Another role bearer in tasks 1 and 5 is foil 5. Foil 5 is the thinnest airfoil and has a low pitching moment, thus promoting slow transition to stall.

Task 6 achieved the third highest objective value. This task used the PSO method but exchanged the non-performing foil 4 for foil 6. Given different design variables to work with, it chose to ignore foils 2 and 3, and lay a higher emphasis on foil 1 and the new foil 6. Foil 6 has the largest value for maximum camber and leading edge radius.

Foils 2 and 4 were not strong features in the optimisation tasks. This is evident by examining the lack of movement from the initial to final percentage of the foil in table 6.1.6. This is especially odd in the case of foil 2 which possesses the most favourable aerodynamic features for the mid profile station of all the base profiles. In fact, a comparison of the geometric features of the optimised profile and foil 2 (Appendix A.2) suggest that the optimised foil is built to replicate foil 2. Though given a variety of initial percentages, foil 2 was simply not recognised by the optimiser as a suitable design variable. It should be recalled that the coordinates of each airfoil are blended according to the percentage set by the optimiser. Those geometric characteristics of foil 2 which lend it such an aerodynamic advantage, are possibly diminished when the foil's coordinates are reduced by a percentage, and blended with other foils with more radical features (higher camber, greater thickness etc.).

Figure 6.1.19 plots the L/D ratios of the airfoils from each task. Task 5 yields good L/D ratios at angles of attack of 5° to 10° . This is where the mid profile is expected to experience most of its wind conditions. The other tasks show maximum L/D ratios at different angles of attack and these curves tend to taper off more quickly at the higher end of the angle of attack range. Referring to Figure 6.1.20, the optimised airfoil of task 5 can be seen to adhere to the C_{lmax} constraint quite well. Though the lift coefficients are not as high as tasks 1 and 4, this is not a concern as task 5 outperforms these tasks with better L/D ratios.

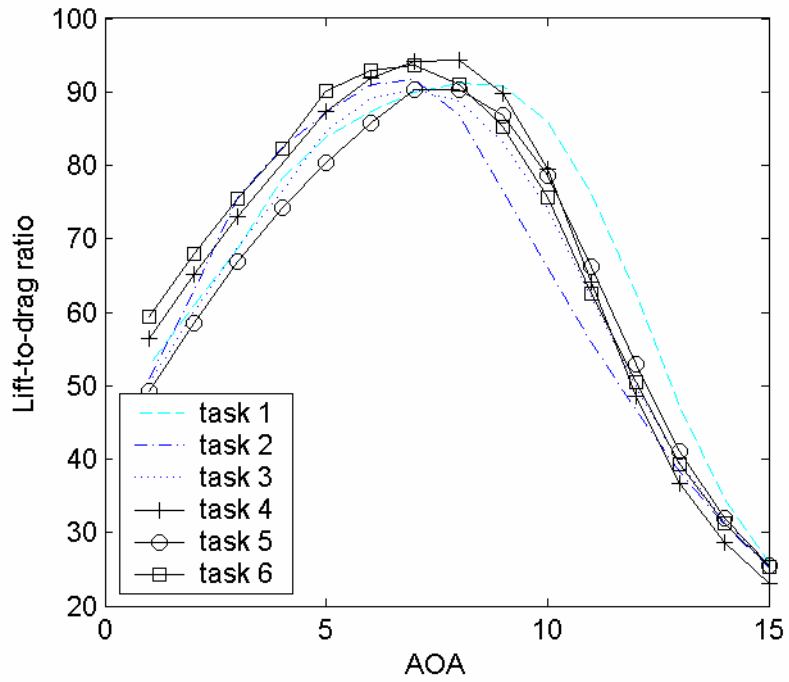


Figure 6.1.19: L/D ratio vs. angle of attack

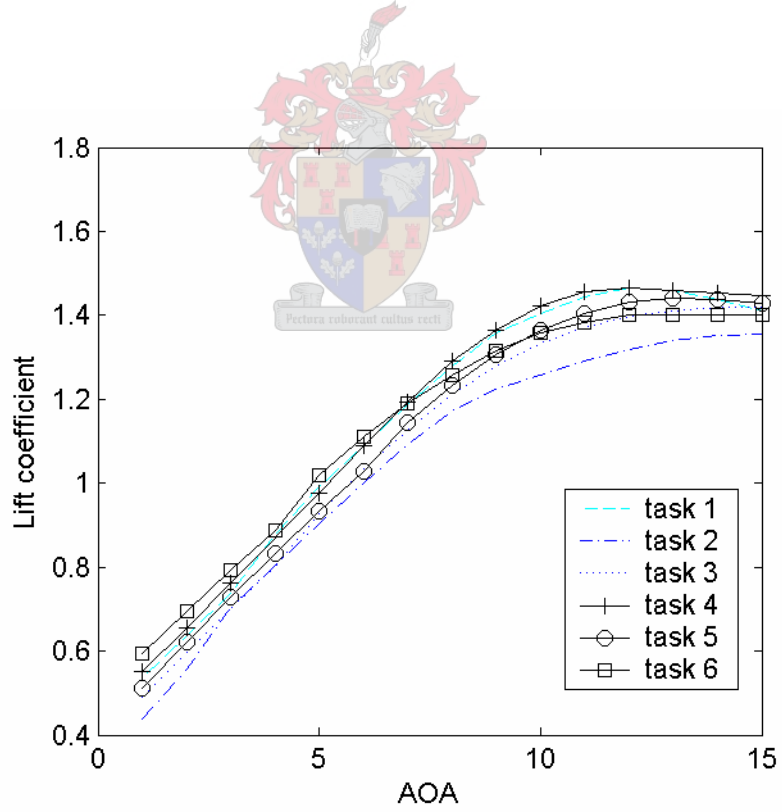


Figure 6.1.20: Lift coefficient vs. angle of attack

6.1.3 Semi Profile

The optimisation problem for the semi profile is an extension of the mid profile optimisation problem. The two stations have the same optimisation objective and constraints. The two design problems also use the same base profiles except for the exchange of the LNV 109a (mid profile's foil 3) with the E387 (semi profile's foil 3); and the absence of the rxcamtx (mid profile's foil 6). The base profiles selected for optimisation are displayed in Figures 6.1.21 to 6.1.25 and the optimised profile in Figure 6.1.26. Their aerodynamic characteristics displayed in table 6.1.7.

- Position of profile is at 75% of blade radius
- Reynolds number: 380,000
- Design range for angles of attack: 1 - 15°
- Objective of optimisation:
Maximise integral of lift-to-drag ratios for range of angles of incidence

$$\text{obj} = \int_{\alpha_0}^{\alpha_1} \frac{C_l}{C_d} d\alpha \quad \begin{array}{l} \alpha_0 = 1^\circ \\ \alpha_1 = 15^\circ \end{array}$$

- Constraints:
Maximum lift coefficient, $C_{l_{\max}} < 1.4$
Mean nose-down pitching moment, $C_{m_{\text{mean}}} < |0.08|$

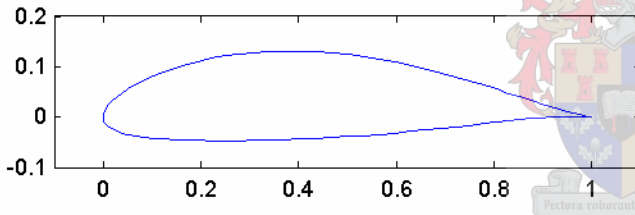


Figure 6.1.21: Foil 1 - fx84w175

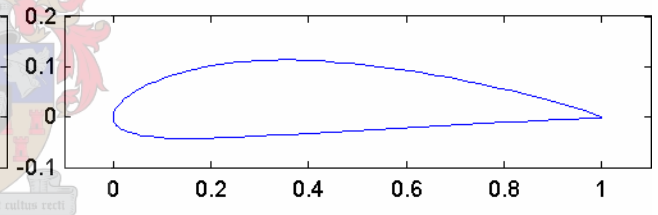


Figure 6.1.22: Foil 2 - naca 4415

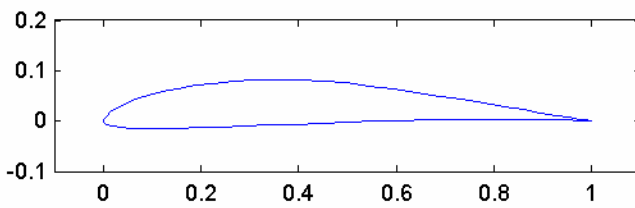


Figure 6.1.23: Foil 3 - e387

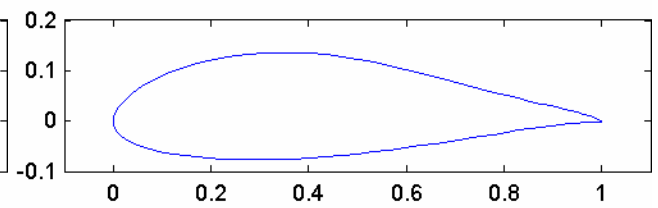


Figure 6.1.24: Foil 4 - ah93w215

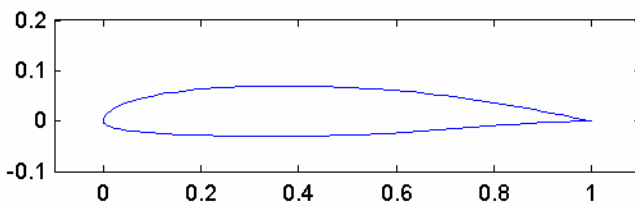


Figure 6.1.25: Foil 5 - sg6041

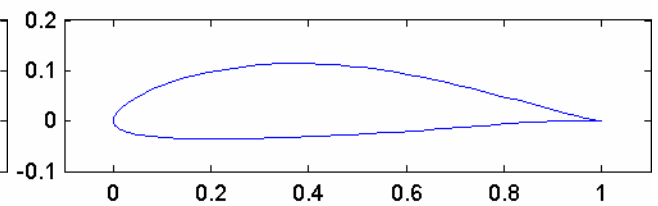


Figure 6.1.26: Optimised semi profile

The optimised semi foil looks very similar to foil 1; however, the underside of the airfoil is reminiscent of foil 5. Speculations aside, the optimised foil constitutes 66% of foil 1 and 34% of foil 3. This percentage is very similar to the final mid profile which also had a large percentage (48%) of its composition from foil 1 (FX 84-W-175) and its third foil (LNV 109a). Geometrically, foil 3 is quite thin with a sharp leading edge and trailing edge. Combining this feature with the bulkiness of foil 1 provided the desired optimised airfoil. Both the mid and semi optimisation tasks attribute a significant percentage of their final airfoils to foil 1 and the base profiles selected for their geometric diversity (in this case, foil 3).

Table 6.1.7: Aerodynamic characteristics of base profiles and semi airfoil

Profile	L/D_{area}	C_{lmax}	@ α [°]	C_{mmean}	L/D_{max}	@ α [°]
foil 1	939.60	1.366	12.0	0.082	91.00	7.0
foil 2	976.10	1.486	14.0	0.087	89.57	7.0
foil 3	838.90	1.316	13.0	0.068	99.83	5.0
foil 4	790.50	1.326	15.0	0.041	76.79	9.0
foil 5	816.20	1.324	15.0	0.041	73.42	3.0
optim foil	1010.80	1.366	15.0	0.083	103.16	7.0

The results from five successful optimisation tasks are presented in table 6.1.8. For the semi profile design problem, there were four SQP and one PSO optimisation tasks. The L/D_{area} values for the various tasks were all within 0.4% of one another, however, task 5 achieved the highest objective and was thus chosen as the most successful optimisation task. The C_{lmax} constraint of 1.4 is over and under-stepped quite widely, more so than in the case of the mid profile. The constraint tolerance remained the same from the mid profile optimisation tasks to the semi profile optimisation tasks. This distance from the constraint boundary must be due to the addition of the new airfoil. The C_{mmean} values for these tasks are much closer to the constraint of 0.08 than in the case of the mid profile. This constraint was often too tight for the semi profile optimisation. Generating a suitable airfoil below this constraint caused the optimiser to work harder - this noted from the longer analysis times and more analysis calls.

Table 6.1.8: Results from five optimisation tasks

Task no	L/D_{area}	C_{lmax}	$C_{m mean}$	Optimisation Method	ana	ana time
					calls	
Task 1	1003.59	1.440	0.087	SQP	rel step 0.2	115 60.9 min
Task 2	1002.82	1.363	0.081	SQP	rel step 0.1	73 39.5 min
Task 3	999.89	1.435	0.078	SQP	rel step 0.1	67 49.3 min
Task 4	1000.73	1.363	0.081	SQP	rel step 0.05	102 52.4 min
Task 5	1010.75	1.366	0.083	PSO	C1 2, C2 2.5	2475 22hr 11 min

The initial and resultant design variable values are contained in table 6.1.9. As previously mentioned, PSO does not have an initial position in the solution space. The optimisation results from tasks 2, 4 and 5 were very similar. Their resultant percentage compositions are also in close agreement. Foils 1

and 3 were clearly the most influential base foils. The final airfoils from tasks 2, 4 and 5 had on average 33% contribution from foil 3 and 65% from foil 1. The three tasks used different optimisation methods and initial conditions, but managed to converge to the same solution. This provides confirmation of the final solution. As known from the mid profile optimisation, foil 1 produces a high L/D_{area} value and still adheres to the C_{lmax} constraint. Furthermore, it has high values for maximum thickness and maximum camber. Foil 3 is certainly the thinnest airfoil, with a low maximum camber and small leading edge radius. Furthermore, its aerodynamic characteristics are not exceptional. Nevertheless, the combination of these two foils is chosen as the preferred blend in three different tasks.

Table 6.1.9: Initial and resultant percentage composition for each task

Task no	foil 1	foil 2	foil 3	foil 4	foil 5
Task 1	0.648	0.180	0.100	0.007	0.065
Task 2	0.032	0.240	0.600	0.038	0.090
Task 3	0.032	0.038	0.090	0.240	0.600
Task 4	0.032	0.038	0.090	0.240	0.600
Task 5	-	-	-	-	-
Task 1	0.577	0.035	0.273	0.106	0.009
Task 2	0.654	0.007	0.337	0.002	0.000
Task 3	0.022	0.268	0.452	0.258	0.000
Task 4	0.650	0.014	0.317	0.005	0.014
Task 5	0.655	0.005	0.339	0.000	0.000

Tasks 3 and 4 used the same initial variables and optimisation method, however, task 3 used a larger step size than task 4 and produced significantly different compositions in their final airfoils. This can only be attributed to the presence of a local maximum in the solution space. Task 3 is the only task that gives significant influence to foils 2 and 4. These foils were also not instrumental during the mid profile optimisation. Though it is obvious why foil 4 is unsuccessful - it is a bulky airfoil with minimal camber and consequent low aerodynamic performance - the same can not be said of foil 2 which has already been identified as a prime candidate for the objectives of the mid and semi profile optimisations. At this point it becomes clear that the method of blending introduces an unforeseen factor in the optimisation process. The geometric features that allow foil 2 to produce good aerodynamic performance do not survive the blending process. Instead, it is those foils which are thicker or thinner or have a more exceptional geometry which prove to be successful in the optimisation process.

Figure 6.1.27 plots the L/D ratios for all the tasks vs. angle of attack. The trend for all the optimisation tasks is almost identical. Most tasks achieve a maximum L/D ratio at 7° . Examination of the lift coefficients in Figure 6.1.28 allows better insight into the differences between the tasks. Tasks 1 and 3 reach a higher C_{lmax} at a lower angle of attack than task 5. Task 5 is more conservative in regard to its C_{lmax} constraint.

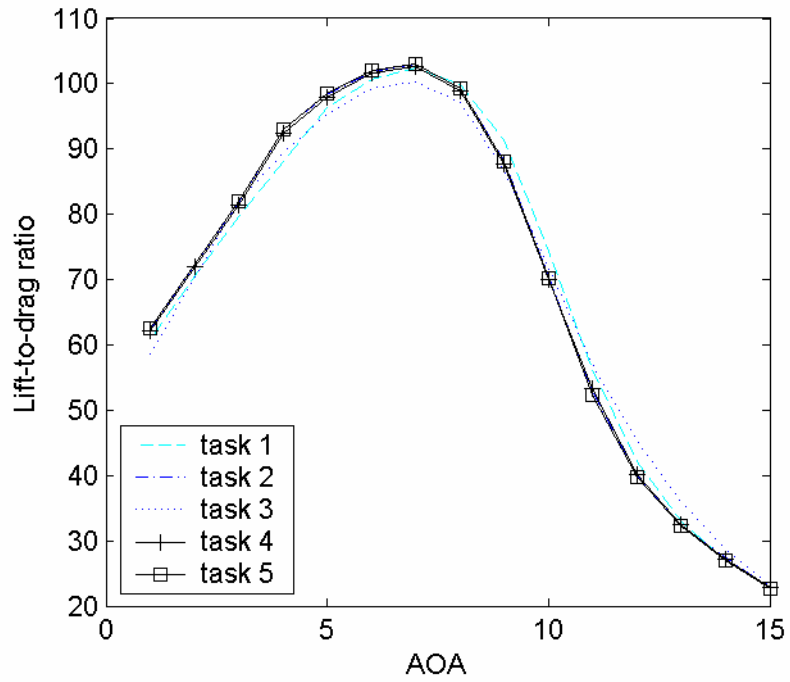


Figure 6.1.27: L/D ratio vs. angle of attack

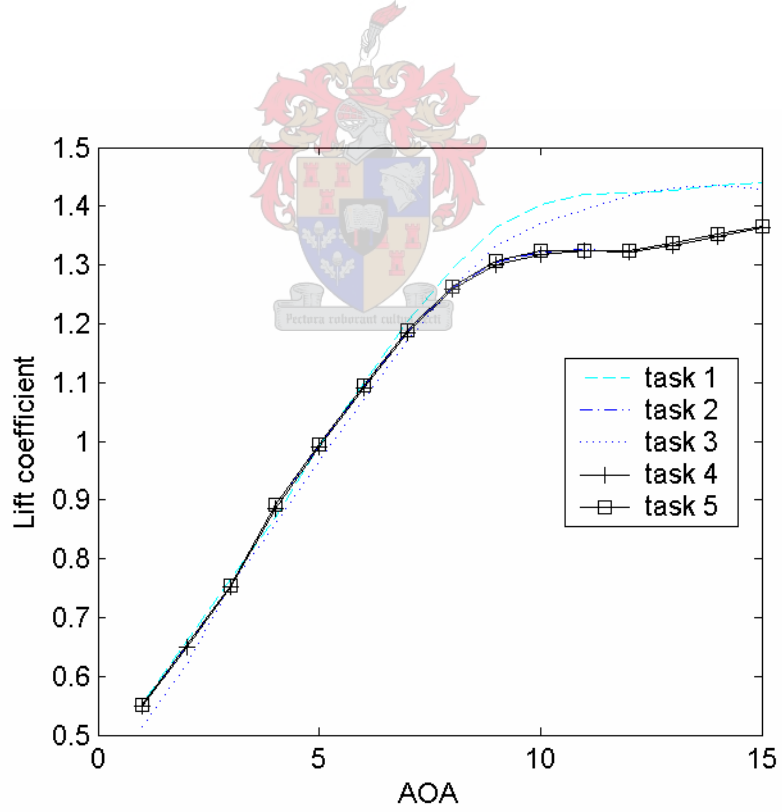


Figure 6.1.28: Lift coefficient vs. angle of attack

6.1.4 Tip Profile

The tip profile is selected to design for stall regulation. The design objective was to maximise the lift-to-drag ratios over a narrow range of angles of attack and encourage transition to stall beyond this range. The base profiles are plotted in Figures 6.1.29 to 6.1.34 and the optimised tip profile in Figure 6.1.35. Their aerodynamic characteristics are displayed in table 6.1.10.

- Position of profile is at 95% of blade radius
- Reynolds number: 400,000
- Design range for angles of incidence: 1 - 10°
- Objective of optimisation:
Maximise integral of lift-to-drag ratios for range of angles of incidence

$$\text{obj} = \int_{\alpha_0}^{\alpha_1} \frac{C_l}{C_d} d\alpha \quad \begin{array}{l} \alpha_0 = 1^\circ \\ \alpha_1 = 10^\circ \end{array}$$

- Constraints:
Maximum lift coefficient, $C_{l_{\max}} < 1.2$
Location of $C_{l_{\max}}$ constrained to $\alpha < 13^\circ$
Mean nose-down pitching moment, $C_{m,\text{mean}} < 0.1$

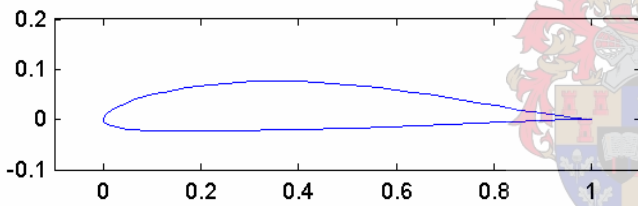


Figure 6.1.29: Foil 1 - fx84w097

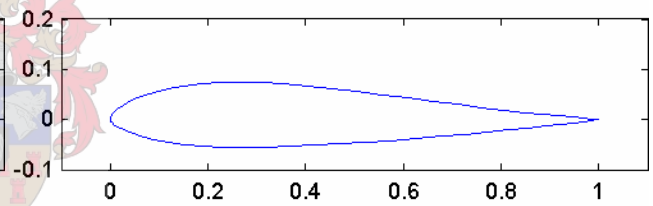


Figure 6.1.30: Foil 2 - mh106

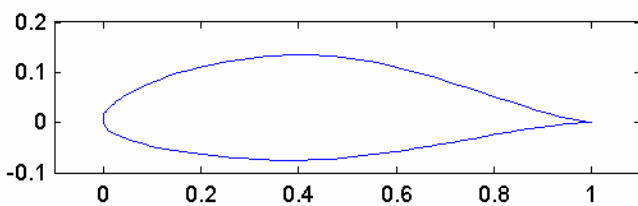


Figure 6.1.31: Foil 3 - naca 654-421

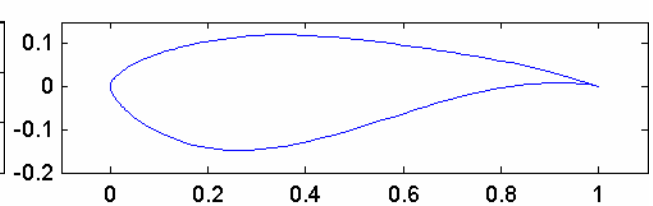


Figure 6.1.32: Foil 4 - Somer's root foil

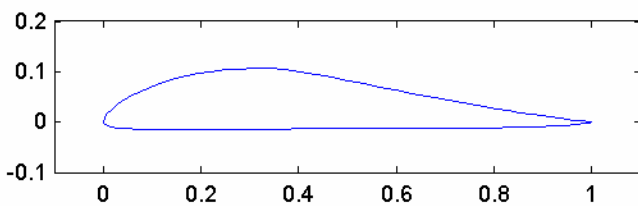


Figure 6.1.33: Foil 5 - fx77w121

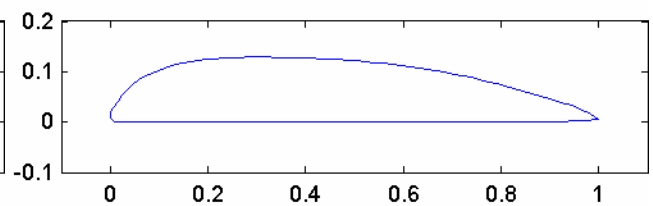


Figure 6.1.34: Foil 6 - raf-6D

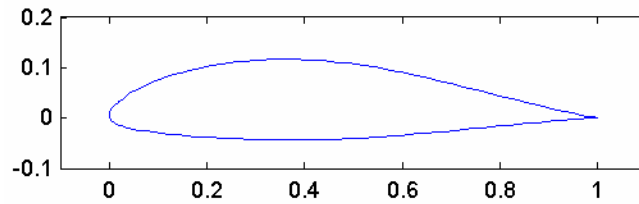


Figure 6.1.35: Optimised tip profile

Table 6.1.10: Aerodynamic characteristics of base profiles and tip airfoil

Profile	L/D _{area}	C _{lmax}	@ <i>aoa</i> [°]	C _{m mean}	L/D _{max}	@ <i>aoa</i> [°]
foil 1	659.721	1.279	13	0.068	92.877	5
foil 2	522.325	1.186	12	0.000	78.040	7
foil 3	573.059	1.135	20	0.034	81.756	7
foil 4	491.904	1.275	20	0.107	69.870	9
foil 5	626.170	1.217	7	0.050	102.717	7
foil 6	603.420	1.555	11	0.102	73.331	5
optim foil	717.030	1.187	10	0.029	98.499	7

Similar to the design problem of the root station, the tip station base profile shapes are quite varied. These foils were selected on the condition that they met the C_{lmax} constraint and then according to the summated lift-to-drag ratios over the angle of attack 1 to 10° range. Foils 1, 4 and 6 were added for diversity. The geometry of the optimised tip foil is similar to that of foil 3. The nose is sharper and in general the foil is thinner. In fact, the optimised tip profile constitutes the following: 15% of foil 1, 49% of foil 3, 26% of foils 5, and 10% of foil 6. Base foils 3 and 5 adequately fulfil the C_{lmax} constraint, while maintaining high values of L/D_{area} . Foils 1 and 6 did not maintain the C_{lmax} constraint, but did have a high average of L/D ratios in the angle of attack range. A further advantage of foils 3 and 5 was that their positions of maximum camber and maximum thickness occur further back along the chord than the other base foils. This has the effect of extending the upper airfoil surface on the leading side of the airfoil. At increased velocities and angles of attack this assists in boundary layer separation and hence stall.

There are six successful optimisation tasks presented in this section, refer to table 6.1.11. Due to the necessity of ensuring stall regulation, close adherence to the C_{lmax} constraint was necessary. Tasks 5 and 6 produced airfoils which did not overstep this constraint or that on the angle of attack location of C_{lmax} . Though task 4 also yielded an excellent candidate for the tip profile, the C_{lmax} occurs at a higher than desirable angle of attack. Tasks 1 to 3 were not deemed to be competitive due to their over-stepping of the constraints. Both tasks 5 and 6 made use of the PSO optimisation method. Task 6 was set up with twice the inertia parameter used in task 5. Greater inertia had the effect of slowing the optimisation progress, resulting in an increased number of iterations and investigation into particular niches of the solution space. The respective base foil percentages of each task are displayed in table 6.1.12.

Table 6.1.11: Results from six optimisation tasks

Task no	L/D _{area}	C _{lmax}	@aoa [°]	Optimisation Method	
Task 1	725.026	1.212	15	SQP	rel step 0.2
Task 2	726.158	1.212	9	SQP	rel step 0.1
Task 3	718.852	1.208	14	SQP	rel step 0.1
Task 4	733.311	1.207	15	SQP	rel step 0.05
Task 5	715.653	1.196	9	PSO	C1 1.5, C2 2.5
Task 6	717.030	1.187	10	PSO	C1 1.5, C2 2.5

Table 6.1.12: Resultant percentage composition for each task

Task no	foil 1	foil 2	foil 3	foil 4	foil 5	foil 6
Task 1	0.355	0.000	0.192	0.000	0.453	-
Task 2	0.249	0.000	0.282	0.000	0.469	-
Task 3	0.280	0.029	0.206	0.026	0.459	-
Task 4	0.245	0.019	0.383	-	0.213	0.141
Task 5	0.120	0.000	0.497	-	0.292	0.091
Task 6	0.151	0.000	0.489	-	0.260	0.100

The results from tasks 1 to 3 yielded airfoils with similar foil compositions. Foil 4 is a consistent low-performer, thus this foil was interchanged with foil 6 which has higher values for L/D_{area} and C_{lmax}. With the addition of the higher-cambered foil 6, foil 5 had a reduced percentage of the final optimised foils with an increase in foil 3's. Foils 3 and 5 featured in all of the optimisation tasks since their L/D_{area} and constraint values are suitable. Base foils 2 and 4 were not significantly considered in any of the optimisation tasks. These foils had the lowest values for the objective.

Figure 6.1.36 displays the L/D ratios of the various tasks' optimum profiles against angle of attack. These L/D ratios follow more or less the same trend. Below an angle of attack of 7°, there is differentiation in the tasks. Here it is evident that task 4 has the highest L/D ratios which explains its high objective value. However, it is clear that the tip profile has been designed to operate at angles of attack below 10°. In Figure 6.1.37, the lift coefficients for each task are plotted against the angle of attack. All the tasks manage to peak before an angle of attack of 10° and maintain a plateau of C_l equal to 1.2. For the objective of stall regulation, it would be better to see the C_l values drop away after attaining 1.2, however this was unfortunately not described in the objectives and constraints for the optimisation problem.

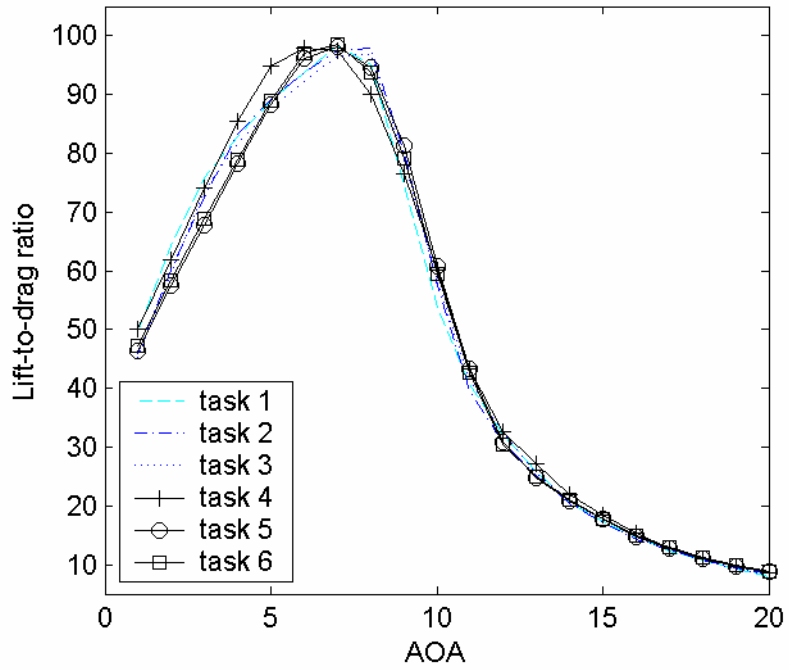


Figure 6.1.36: L/D ratio vs. angle of attack

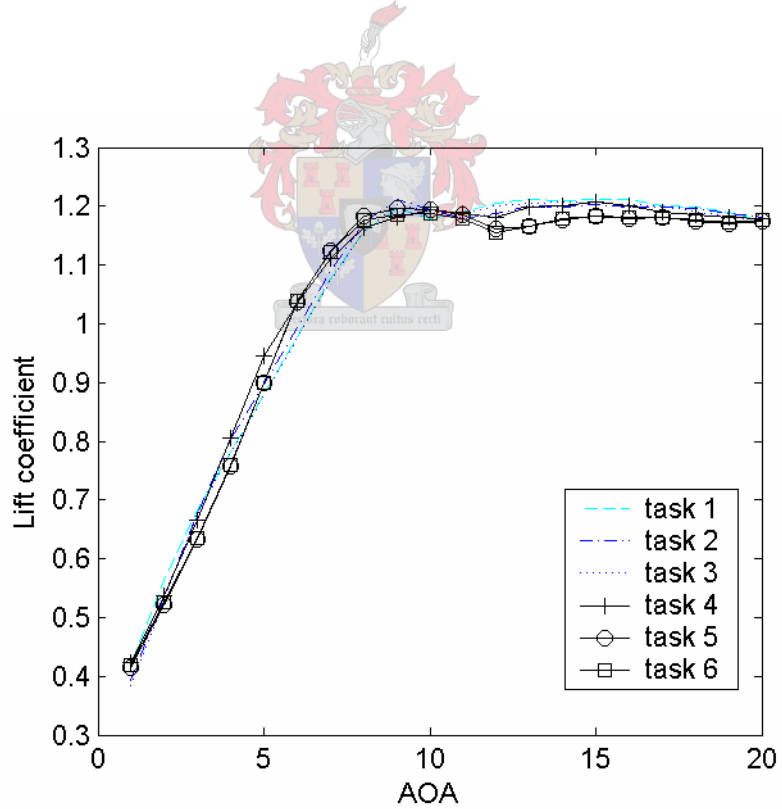


Figure 6.1.37: Lift coefficient vs. angle of attack

6.1.5 Discussion of Results

Four optimisation design problems have been presented in this section. The successful optimisation tasks, as well as the geometric and aerodynamic characteristics of their final airfoils have been presented. Naturally there were additional optimisation tasks whose results were less satisfactory. These failed tasks provided valuable insight into features of the solution space for each optimisation problem, further aiding selection of suitable optimisation methods.

Post-analysis of the optimisation results has sought to gain insight into the practical application of the mathematical optimisation methods to the design problem. This is achieved by examining the design variables (the base profiles) and their resultant weightings in the different optimisation tasks. Generally speaking, the base profile with adequate compliance to the objectives and constraints would have significant influence in the final optimised airfoil. However, often the lesser suitable base profiles would constitute a large portion of the final airfoil. These profiles would have lower objective values, or would over-step the constraints. Also, these profiles had radical geometric features and were only included to add diversity to the sample base of profiles. In particular foil 2, included in the mid and semi optimisation problems, was the prime aerodynamic candidate for contribution to the final optimised profiles. However, foil 2 received zero or close to zero contribution in nearly all the optimisation tasks in both problems. This brought the realisation that the method of blending airfoils brings an unforeseen factor into the optimisation process.

The aerodynamic performance of an airfoil is dependent on the combination of the geometric features of that airfoil. Should a base profile with favourable aerodynamic characteristics be blended with another profile of favourable characteristics, the resultant airfoil may not have a summation of the characteristics. This resultant airfoil may appear completely different and thus adopt entirely unique aerodynamic characteristics. However, an airfoil blended from two base airfoils with exaggerated geometric features relative to one another (i.e. one has a much bigger maximum camber than the other) is more likely to maintain its parents' aerodynamic characteristics.

In the case of the mid and semi optimisation problems, foil 2 did not have any exaggerated geometric features relative to the sample base profiles and was excluded. The resultant airfoils for all the optimisation tasks were a combination of a bulky base profile (foil 1) with a high maximum camber, and a thinner profile with a lower maximum camber. The optimiser thus manipulated these profiles to obtain the final airfoil. In contrast, the root and tip optimisation problems did favour the base profiles with the most aerodynamic advantage. Examination of the base profiles selected for these problems reveals that they were quite different from each other, both in aerodynamic characteristics and geometric shape. The mid and semi optimisation problems would have benefited from a more distinct sample of base profiles.

A number of disadvantages of the blending method have become evident. Firstly, the optimiser is not able to segregate the good and bad characteristics of a base profile, and then only use the good. For example, given a particular base profile which has a suitable nose and leading edge; however, its trailing edge angle is far too thick for the application. Ideally, one should grant a higher weighting to the leading edge and a lower weighting to the trailing edge before blending this profile with another. Instead the optimiser compromises on the weighting fraction or mixes the foil with one that has a particularly thin

trailing edge. If basis shapes, such as triangles, had been used, it may have been easier to maintain the airfoil changes to a single location instead of affecting the whole airfoil. However, these basis shapes could not be programmed within the geometry creation facility of XFOIL.

Another disadvantage of this design method has resulted in a lack of uniqueness of the final product. Most of the optimised airfoils have allowed a significant percentage from only three base foils. The weightings of the last two base foils in a set were reduced to nearly zero. Even when these zero-performers were interchanged, the resultant set would still depend heavily on the influence from only three airfoils. Allowing a significant percentage from five base profiles has the effect that the distinctive features of these foils become phased out, unless they are extremely exaggerated in the original state. Recall that specific profiles were included to add diversity to the set of base profiles. More often than not, these diversity profiles contributed significant percentage to the optimised station airfoils.

As mentioned, the set of base profiles used in the optimisation design problems were selected from a sample of airfoils widely used in the wind turbine industry. However, this manual selection already had a drastic effect on the efficiency of the optimiser by reducing the pool from which base profiles were selected. Although profiles from other application fields were included in the brief analysis, greater experience in the aerodynamics industry may have pointed to better applicable foils.

Nevertheless, the optimiser has succeeded in blending the base profiles to yield four airfoils which outperform their constituent parts. Examination of the graphical plots of the lift coefficients and lift-to-drag ratios at each station are confirmation of this.



6.2 Rotor Optimisation

6.2.1 Weibull-weighted Designs

This section presents the results from the wind rotor optimisation. The goal for the optimiser was to find the rotor configuration that yielded the most suitable design for the conditions specified. The airfoil profiles have already been optimised separately in the previous section, thus the optimiser could adjust only the chord and pitch distributions to obtain optimal rotor performance. This performance is quantified by the measure C_{Pobj} , which equals the weighted sum of the Coefficient of Power (C_p) at each windspeed.

Table 6.2.1 is a summary of the ten optimisation tasks successfully performed. Each task has a design number, ranging from A to L. The task description details the type of optimisation method implemented, while the third column lists the objective values for each design. These objective values were each designated a relative difference to the C_{Pobj} value of the CSIR design. The percentage values allow for effective comparison. Designs A to H employed the Weibull weighting distribution. Designs K and L experimented with different airfoil profiles for each station, still with the application of the Weibull weighting to obtain the objective value.

Table 6.2.1: Summary of Optimisation Tasks

Des no.	Task description	CP obj	%
CSIR		0.483	
Weibull weighting			
A	PSO C1 1.4, C2 1.5	0.535	10.923
B	SQP rel step 0.1	0.535	10.834
C	SLP rel step 0.1	0.528	9.518
D	SQP rel step 0.15	0.526	8.967
E	SQP rel step 0.05	0.525	8.811
F	SQP rel step 0.1	0.523	8.468
G	SQP rel step 0.05	0.518	7.354
H	SLP rel step 0.05	0.516	6.917
Non-selection profiles, Weibull weighting			
K	SQP rel step 0.05	0.523	8.323
L	SQP rel step 0.1	0.508	5.267

The optimisation methods used were as follows: PSO - Particle Swarm Optimisation, SQP - Sequential Quadratic Programming, SLP - Sequential Linear Programming. It should be recalled that the non-gradient method PSO is in fact quite an expensive optimisation method, due to the number of function evaluations and lengthy analysis time. However, the solution space for the rotor optimisation is such that the SQP method is more than adequate to identify the optimum. In this case, it is design B.

Figure 6.2.1 compares the Coefficient of Power (C_p) distributions for the Weibull-weighted designs. The influence of the Weibull weighting is evident, since most of the designs maintain high C_p values between 5 and 6 m/s, where after they drop off steadily. This trend is best represented by designs

A and B, which maintain a high average value of C_p while simultaneously managing to follow the trend of the Weibull distribution. Obvious exceptions to this trend are designs F, G and H. These designs furthermore achieved the lowest C_{pobj} values.

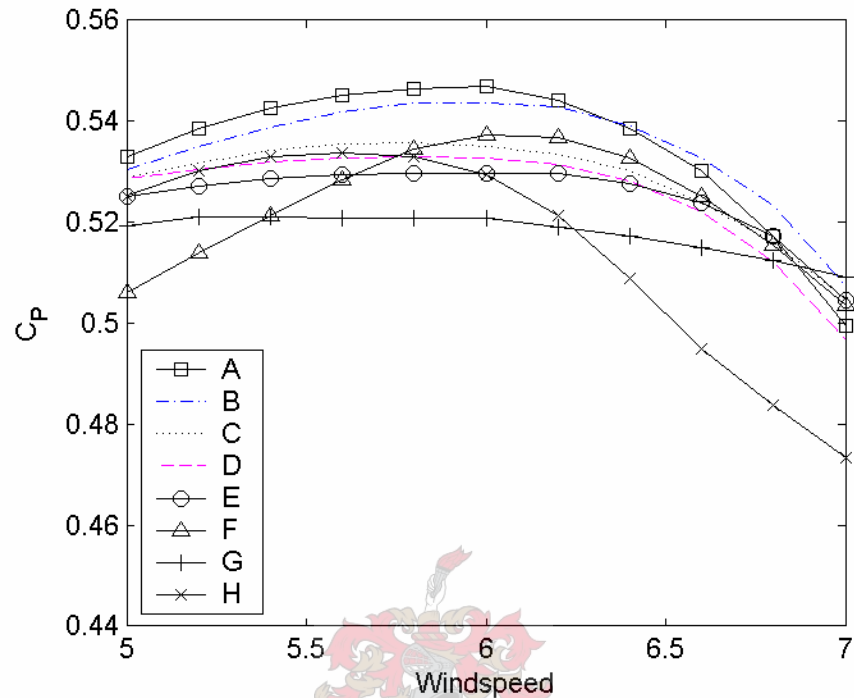


Figure 6.2.1: Results from eight tasks using Weibull-weighting distribution

Further investigation into the set-up of the optimisation tasks for designs F, G and H, explains their deviation from the norm. Design F did not have the same constant circulation constraint as imposed on the other design tasks. Studies have shown this to be a most favourable characteristic of a successful rotor. As regards design G, its deviation can be most adequately assessed when comparing it to design E. Designs G and E had the same task details, except that design G had different initial conditions to E. These initial conditions gave design E the advantage over G. The relative step size for optimisation tasks E and G is clearly not large enough to bridge over a local minimum. A similar scenario is painted when comparing designs C and H. Both designs employed the SLP optimisation method, which is considered to be the most basic gradient method. They used the same initial design variables, however, design C has twice the relative step size of H and far outperforms this design. Furthermore, design task H made use of only nine iterations, while design task C had thirty-five. Clearly a larger relative step size is more beneficial for the solution space of this optimisation problem.

Figure 6.2.2 allows closer inspection of the top five designs, A to E. These are plotted together with the results from the rotor designed by the CSIR, which has been used throughout this project for comparative purposes. Designs A to E present a remarkable improvement on the CSIR rotor, and are on average only 10% lower than the Betz limit of 0.5926. Referring to table 6.2.1, recall that designs A to E produced target values (C_{pobj}) with an improvement of 9 to 11% over the CSIR design. Referring to Figure

6.2.2, it is further evident that the overall performances of the optimised designs are indeed better over the range of windspeeds.

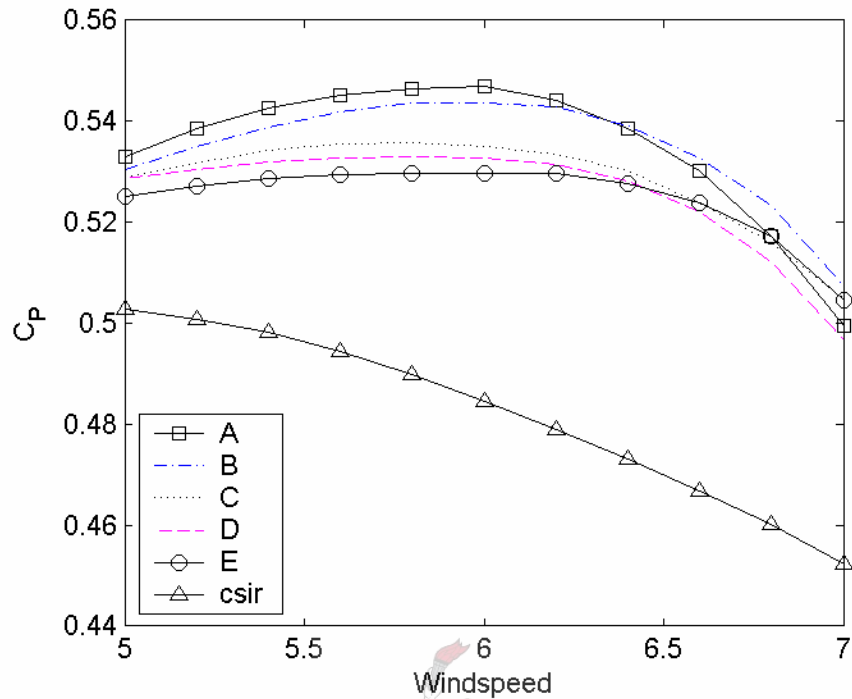


Figure 6.2.2: Top five designs compared to CSIR blade

Inspection of the chord distributions shows that the chord lengths of the CSIR blade at each radial station are much lower than those of designs A to H (Figure 6.2.3). Chord length has a direct influence on the Reynolds numbers used for analysis of aerodynamic performance. Generally, a higher Reynolds number will lead to higher values of lift-to-drag ratios for the profiles at each station. Furthermore, it should be noted that the CSIR design used the same profile for each station. The lift-to-drag ratios of this profile were on average much lower than the profiles used in this project. According to Figure 6.2.3, the chord lengths of designs A and B tend to follow the norm of the other designs. Since these are the top achievers,

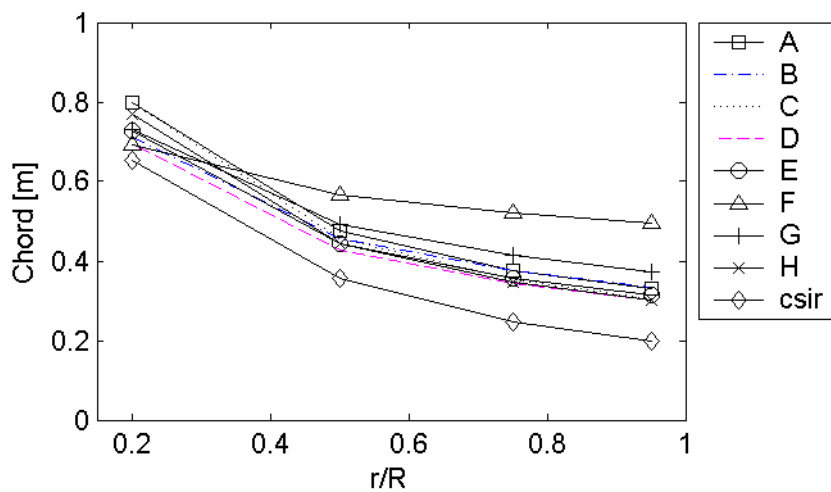


Figure 6.2.3: Chord distributions of designs A to H, including the CSIR design

their advantage must lie in the pitch angle distribution. Design F has much higher chord lengths at the mid, semi and tip stations. This is a result of the lack of constraint on the circulation. Recall that circulation around a blade element is directly proportional to the radius and the chord. For circulation to remain constant, as the radius increases the chord should decrease proportionally.

Figure 6.2.4 displays the pitch angle distributions of the design tasks, as well as that of the CSIR design. These generally decrease exponentially from root to tip, except for designs F and H. Here the pitch angles at semi and tip stations are higher than at mid. Design F did not have the circulation constraint. Furthermore, the initial pitch distribution also had the same trend - semi and tip pitch angles higher than those at the mid station. Such a pitch angle distribution causes discontinuity in the lift coefficients along the blade, and hence the circulation. Without a circulation constraint, design F had no incentive to attempt to correct the pitch angle distribution. During the progression of the optimisation, the difference between mid and semi pitch angles did diminish, but not completely. In the case of design H, the optimisation set-up and initial design variables were identical to those of design C, except that a step size of 0.05 instead of 0.1 was used. The SLP method forms a linearisation of the solution space, thus eliminating much detail. Without the larger step size used in task C, the optimiser converged to a local minimum within only seven iterations.

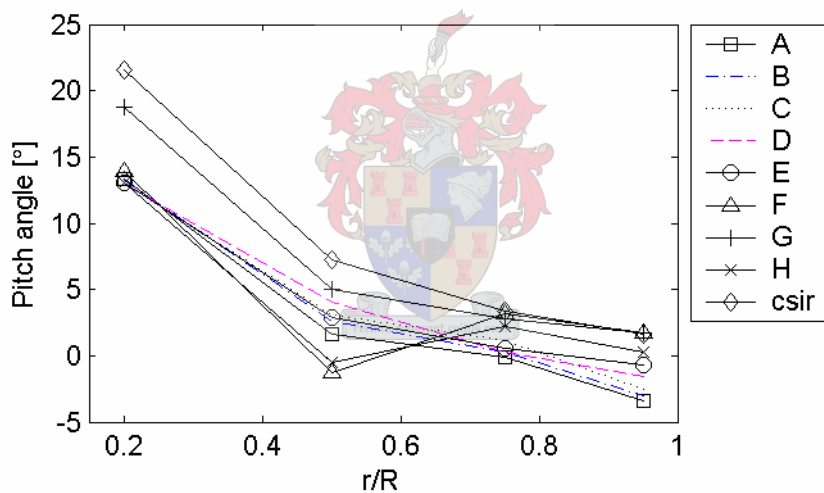


Figure 6.2.4: Pitch distribution of designs A to E, including the CSIR design

The adequacy of the pitch angle distribution is difficult to criticise since the rotor has been evaluated at more than one windspeed. As the windspeed changes from 5 to 7 m/s, the flow angles at each station increase. Thus, a pitch distribution designed for one windspeed might not be adequate for wind turbine operation at another windspeed. This is evident from the CSIR rotor. This rotor was specifically optimised for 5.5 m/s. The pitch angle distribution ensured that the profiles at each station would experience their optimal angles of attack, thus producing peak lift-to-drag ratios. Unfortunately, the windspeed changes cause the angles of attack to fall quickly out of this optimal range. Relative to the CSIR blade, the designs A to H sought to maintain their pitch angles much lower thus enabling these rotor designs to be adaptable to different windspeeds. A and B are the top designs and thus their pitch angle distributions should be considered best suited to the objective. With the exception of the mid station,

their values are generally lower than the other designs. Greater reference shall be made to Figure 6.2.4 in the analysis of lift-to-drag ratios in section 6.2.2.

6.2.2 Analysis of Lift-to-Drag Ratios

The previous section compared different rotor designs based on the performance indicator C_{Pobj} , as well as comparison of the C_p values over the chosen range of windspeeds. Since rotor performance is determined from the two-dimensional aerodynamic characteristics at each station, it is beneficial to examine these characteristics in the context of the three-dimensional design. Of particular interest are the lift-to-drag ratios. This section assesses how the optimiser took advantage of the high performance regions of the airfoil characteristics so as to achieve high performance on the rotor. The following four figures plot the lift-to-drag (L/D) ratios for the Weibull-weighted and CSIR designs at the root, mid, semi and tip stations. Quite remarkable is the comparison between the L/D ratios of the CSIR blade and the optimised blades. The CSIR blade maintains a flat L/D curve for most of the windspeed range and obtains very similar L/D ratios for all four rotor stations. Though the flow angles vary significantly across the windspeed range, the CSIR pitch angles are so chosen that the L/D ratios remain stable. When comparing the L/D versus angle of attack of the CSIR and optimised profiles, it was noted that CSIR tends to have less of a peak than the optimised profiles, thus a sustained average of 70.

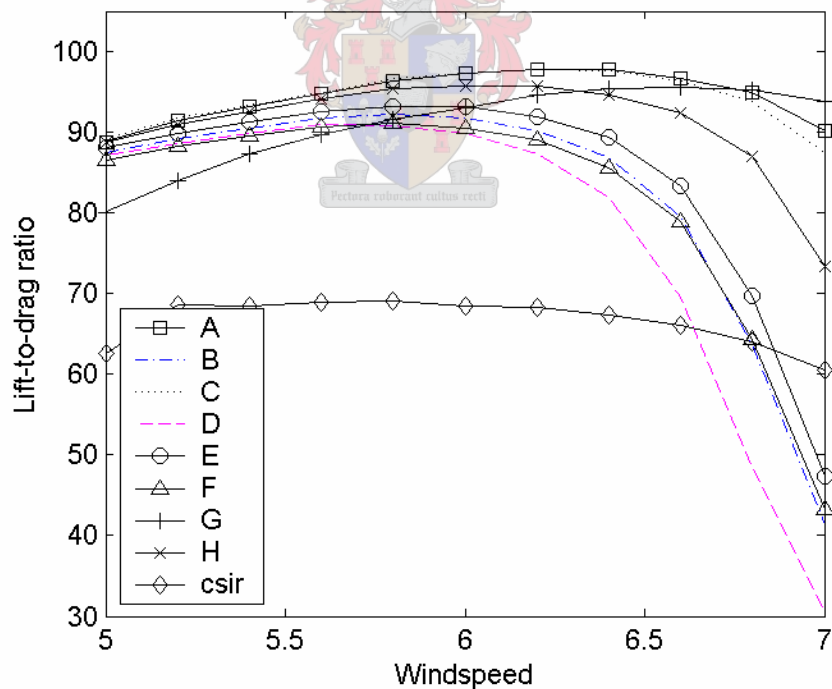


Figure 6.2.5: Lift-to-drag ratios for root station

In Figure 6.2.5, most designs maintain lift-to-drag ratios between 85 and 95 at low windspeeds, that gradually drop off after a windspeed of 6.4 m/s. Paying closer attention to individual designs, design A succeeds in maintaining the highest lift-to-drag ratios, with design C being the next most favourable

root design. Referring to Figure 6.2.3, these two designs have the largest chord length at the root. The root pitch angles of all the designs were similar, thus the success of designs A and C must be due to the greater chord length design.

Design G has a large pitch angle at the root, and consequently presents a different trend: the L/D ratio vs. windspeed profile is much flatter, and tends to have lower values at 5 m/s. The initial value for the root pitch angle of G was chosen much larger than the other designs, and this did not vary much through the optimisation iterations. Previous investigation of the solution space (appendix A.5) revealed that the pitch angle at the root had little influence on the C_p values. Thus, the optimiser places less priority on searching in this gradient direction.

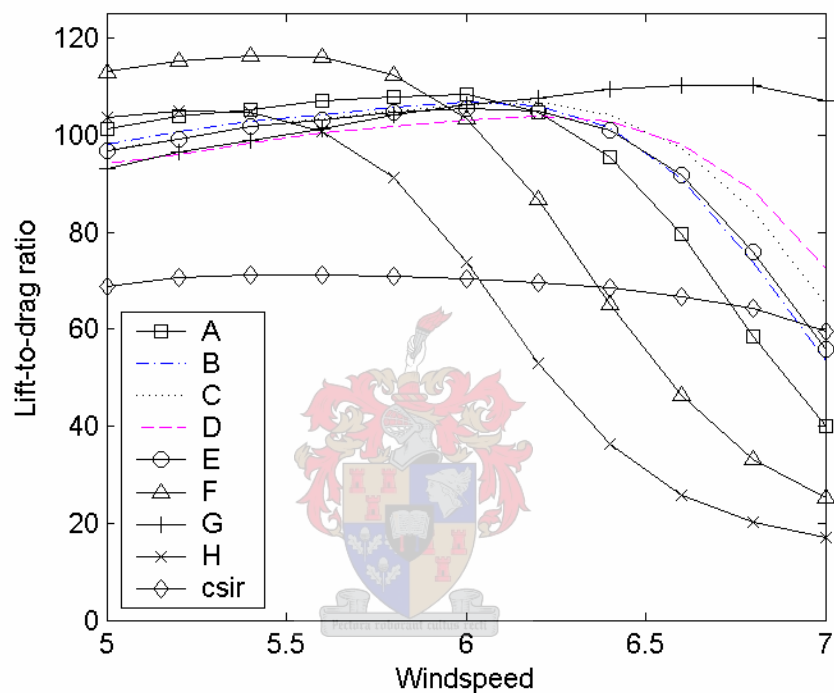


Figure 6.2.6: Lift-to-drag ratios for mid station

Figure 6.2.6 exhibits the lift-to-drag ratios at the mid station. The norm is here represented by designs B to E, which sustain an almost linearly increasing slope for windspeeds from 5 to 6 m/s, where after the lift-to-drag ratio values drop off significantly. The top scoring designs, A and B, follow the same inclination, however, design A has higher values from 5 to 6.2 m/s, where after they drop lower than B's values. Design A has a slightly greater chord length at the mid station, but a lower pitch angle. Design F has higher L/D values than both A and B at lower windspeeds (5 to 5.8 m/s) but these then rapidly decrease to much lower values at higher windspeeds. Recall that F had a dramatically larger chord and lower pitch angle at the mid station. Furthermore, design H also had one of the lower pitch angles at mid station, and consequently also exhibits the rapidly decreasing L/D trend of designs A and F. Unfortunately, design H does not have the benefit of a higher chord length to raise its L/D values. Conversely, design G had a large pitch angle at this station that resulted in its L/D trend maintaining a linearly increasing slope until 6.8 m/s.

Referring to Figure 6.2.7, it can be seen that the top five rotor designs, A to E generate high lift-to-drag ratios in the region of 115 at the semi station at windspeeds of 5 to 5.8 m/s. At the top end of the windspeed range, the lift-to-drag ratio values decrease. Rotor designs F, G and H start off with low values that steadily increase with windspeed. Designs A to E cater for low windspeed performance, and furthermore meet the design requirement which stipulates that the turbine experience slow transition to stall, as can be seen by the decreasing lift-to-drag ratios in the top end of the windspeed range. Considering the differences in pitch and chord distribution, designs F, G, and H have high pitch angles at the semi station, thus encouraging better aerodynamic performance at higher windspeeds, where the flow angles are larger. Also, designs F and G have larger chord lengths, thus amplifying the values at windspeeds greater 5.8 m/s.

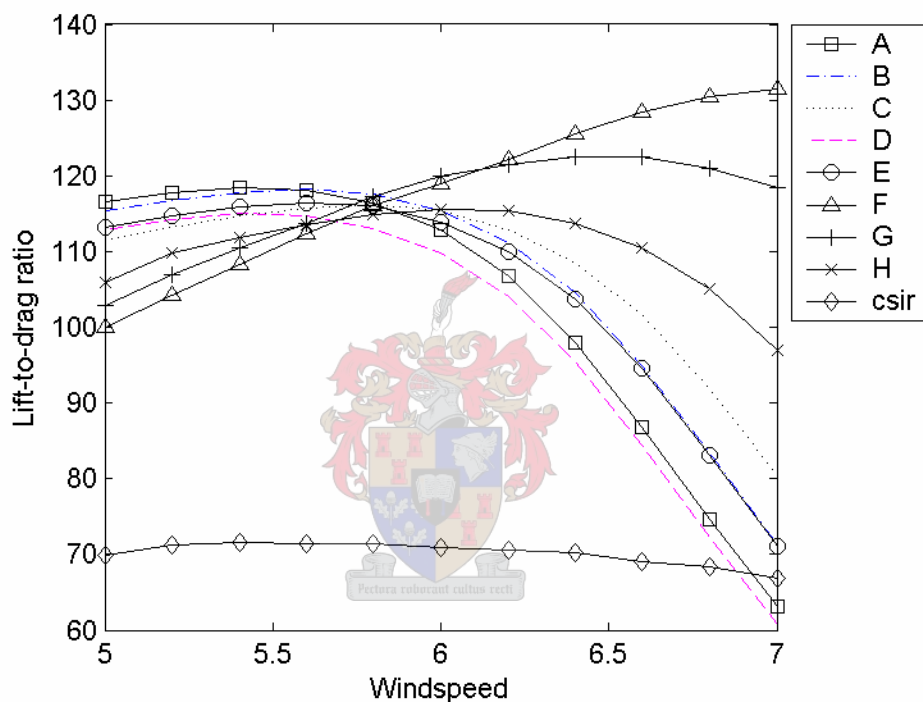


Figure 6.2.7: Lift-to-drag ratios for semi station

The rotor designs exhibit quite different characteristics at the tip station. See Figure 6.2.8. It must be taken into account that the optimised pitch angles were substantially diverse. The trends of designs A, B and C are in fact similar to their respective trends at the semi station, however the tip station L/D values tend to drop off more sharply. Designs A to D had the lowest pitch angles, in fact negative. In the case of designs E to H, their higher pitch angles enabled high L/D ratios for the tip station at windspeeds above 6 m/s. It is doubtful whether these designs will succeed as stall-regulated turbines. Designs F and G furthermore had greater chord lengths than the other designs.

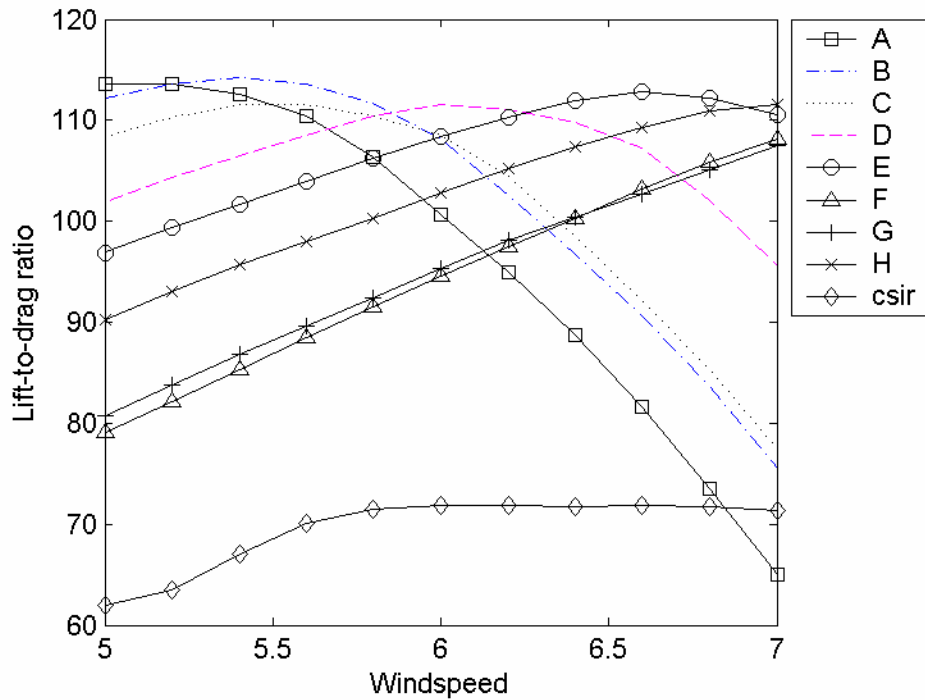


Figure 6.2.8: Lift-to-drag ratios for tip station

The aerodynamic characteristics of each design have been compared at each station. However, the question of whether or not the design has taken advantage of the power-producing potential of the two-dimensional profile still remains. The following figures plot the L/D ratios versus angle of attack for that range of Reynolds numbers encountered by the relevant profile. Indicated on the figures are the operating points for the design. The operating points are the same data contained in the previous figures, only represented differently. Each operating point corresponds with the L/D ratio of the blade profile at a certain windspeed, where the windspeed varies between 5 and 7 m/s, from left to right. Figures 6.2.9 to 6.2.16 offer a closer investigation of the lift-to-drag ratios of designs B and H. B has been rated as the best design, while H is considered the worst. It is a valuable exercise to compare these two designs.

In Figures 6.2.9 and 6.2.10, the Reynolds numbers vary from 300,000 to 500,000. The obvious optimum for the root profile exists at angles of attack between 5 and 10°. Comparing the design results in the two figures, design B has selected optimal lift-to-drag ratios for the lower end of the windspeed vector, while allowing these values to drop off at higher windspeeds. More points of design H are situated in the optimal region, however design B achieves greater performance at the lower end of the windspeed vector, therefore obtaining a higher C_{Pobj} value due to the nature of the Weibull weighting.

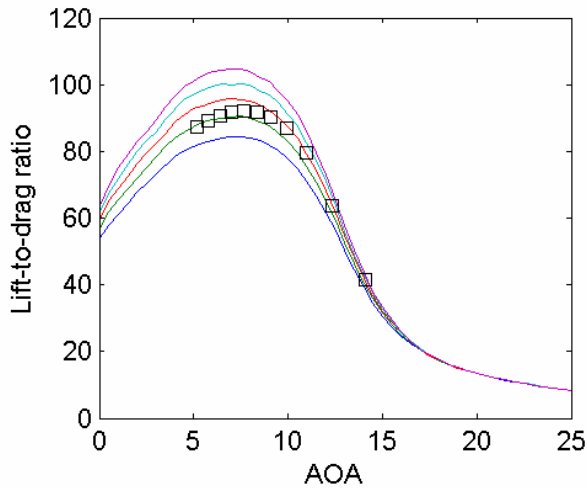


Figure 6.2.9: Design B, root station

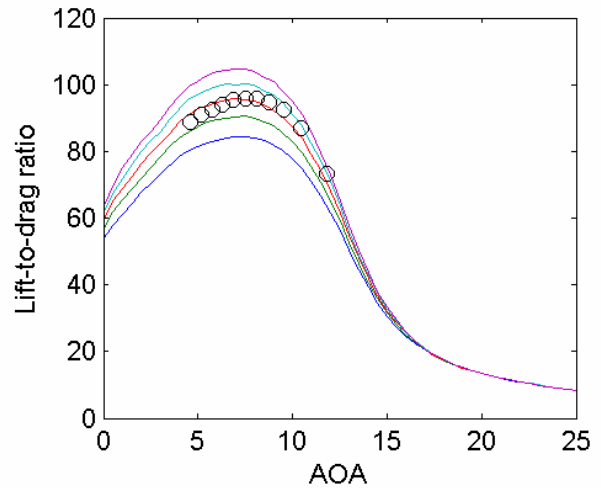


Figure 6.2.10: Design H, root station

The Reynolds numbers at the mid station - Figures 6.2.11 and 6.2.12 - vary from 400,000 to 500,000. Design B is more successful than H in maintaining optimal placement of its design points. Design H has only four points in the peak region of the lift-drag versus angle of attack curve. Design B preserves most of its low windspeed points (windspeeds of 5 to 6.4 m/s) in this peak region.

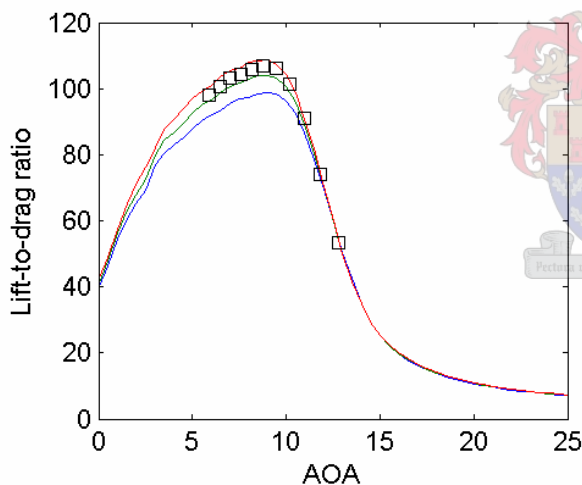


Figure 6.2.11: Design B, mid station

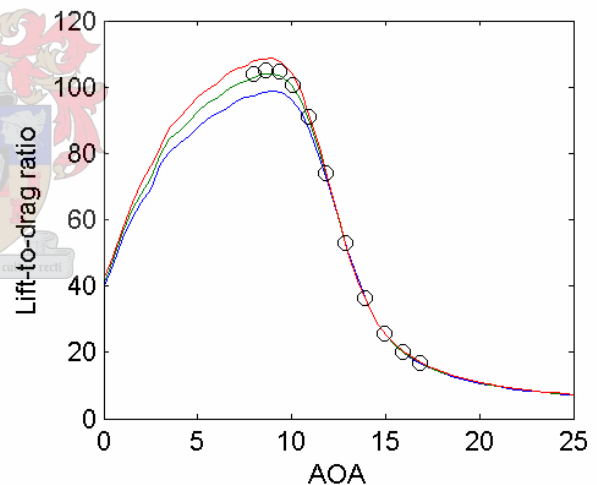


Figure 6.2.12: Design H, mid station

At the semi station - Figures 6.2.13 and 6.2.14 - design B maintains better optimal placement for its low speed values than design H, as in the case at the mid station. Design B's high windspeed operating points are positioned on the negative gradient of the slope (Figure 6.2.13), dropping to much lower L/D values than design H. However, as mentioned, this high-speed performance is of less worth. Since the semi profile peak region is smaller than the mid profile's, the design points are much closer together. Reynolds numbers range from 500,000 to 600,000.

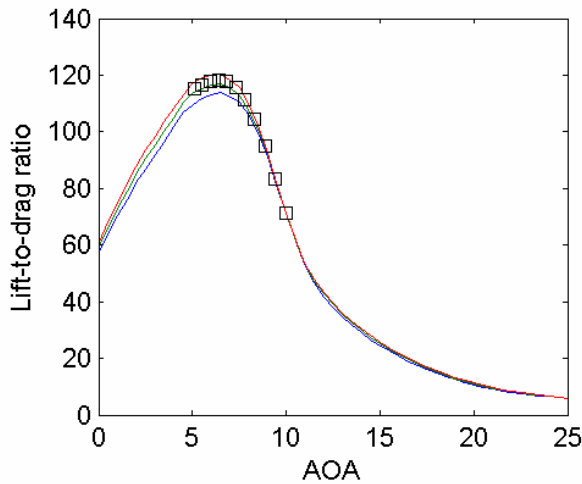


Figure 6.2.13: Design B, semi station

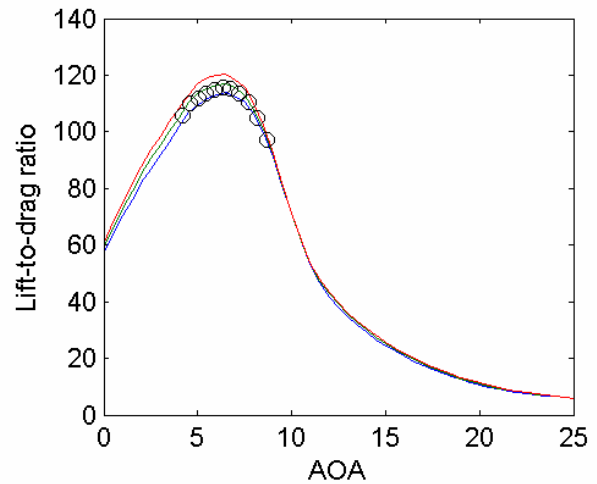


Figure 6.2.14: Design H, semi station

The tip profile has a sharp peak, thus a small optimal operating region (Figures 6.2.15 and 6.2.16). Design B has operating points that tend to slide down the slope, while design H's ascend it. As observed in the tip station lift-drag versus windspeed plot (Figure 6.2.8), this has the effect that design B has large lift-drag ratios which taper off at higher windspeeds. The opposite is true for design H. The Reynolds number range for design B is from 600,000 to 700,000, while design H's is lower - 500,000 to 600,000.

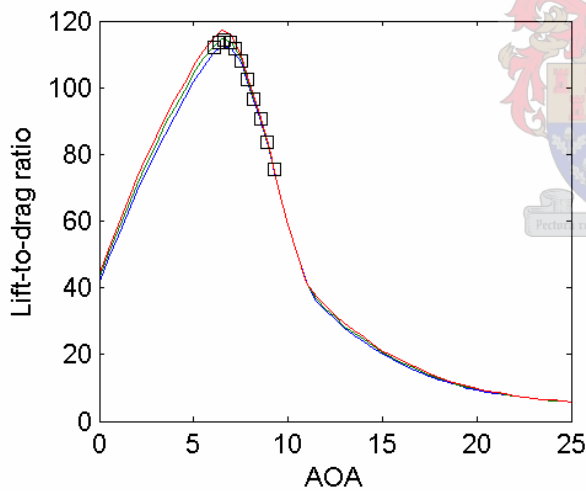


Figure 6.2.15: Design B, tip station

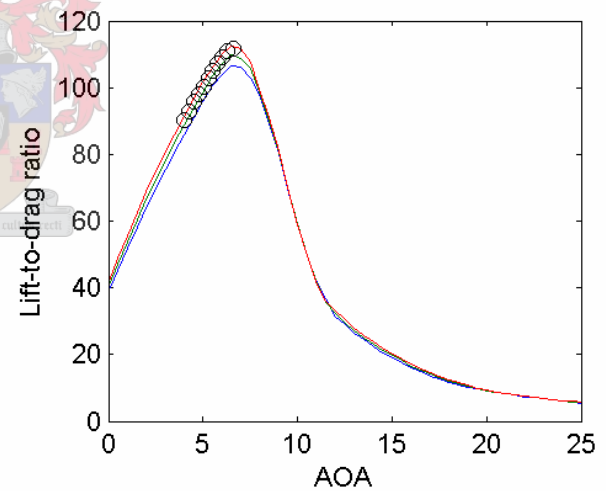


Figure 6.2.16: Design H, tip station

In summary, Figures 6.2.9 to 6.2.16 indicate that design B has ensured that its operating points in the region of 5 to 6 m/s are in the power-producing range of the relevant airfoil profile. Design H succeeds in maintaining its high windspeed operating points in this range. Since the low windspeed C_p values had a higher rating than those at higher windspeeds, design B thus achieved a greater C_{Pobj} value.

6.2.3 Non-selection Profiles

In section 6.2.1, designs A to H all made use of the same set profiles for each of the root, mid, semi and tip stations. These profiles were optimised in section 6.1. It was desired to test the dependence of rotor performance on the choice of airfoil profiles, thus new optimisation tasks were carried out using airfoil profiles which had been found unsuitable by the two-dimensional optimisation process in section 6.1. These profiles are displayed in Figures 6.2.17 to 6.2.20. The ah94w301 had low $C_{l_{max}}$ and L/D_{area} values and was thus ignored as a design variable during the root optimisation tasks. The naca 4415 exhibited prime aerodynamic qualities for the midfoil, however it did not feature in the midfoil optimisation due to geometric considerations. The sg6041 was too thin with too low a camber to benefit the semifoil optimisation and the mh106 also yielded L/D_{area} values which were too low for the tip profile optimisation.

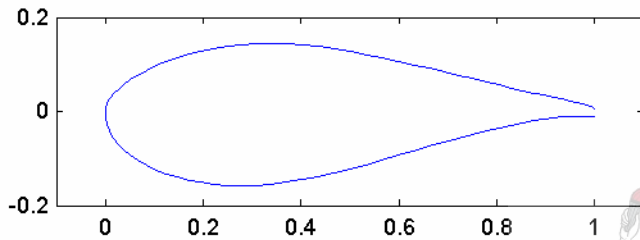


Figure 6.2.17: Rootfoil - ah94w301

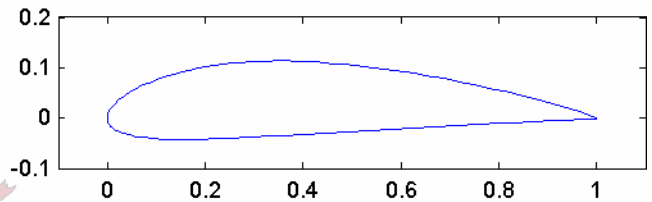


Figure 6.2.18: Midfoil - naca 4415

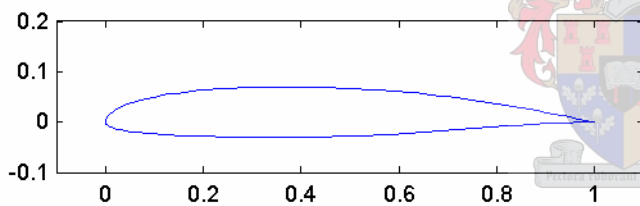


Figure 6.2.19: Semifoil - sg6041

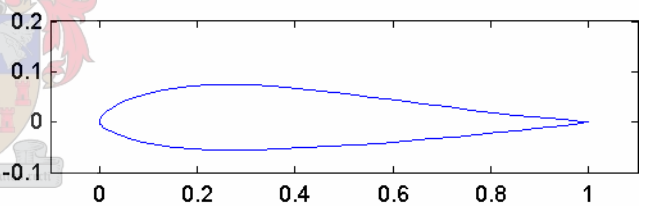


Figure 6.2.20: Tipfoil - mh106

The new rotor designs (K,L) are represented in Figure 6.2.21, together with designs A, B, and C. Though given the same analysis conditions, designs K and L converged with difficulty and only design L managed to mimic the Weibull trend significantly. Design K achieves extremely high C_p values at low windspeed. These rapidly drop off at higher windspeeds. Design L is less dramatic, but can be seen to follow a steadily decreasing trend of C_p values. The $C_{p_{obj}}$ values for designs K and L (table 6.2.1) place design L as the worst achiever while design K is only just lower than design F.

The chord length distribution of designs K and L are not vastly different to designs A to H. Considering the pitch angle distributions, design K has a root pitch angle almost twice the size of designs A and B, which explains the low windspeed performance. Design L's pitch angle distribution is too low to produce angles of attack in the optimal region of the station profiles.

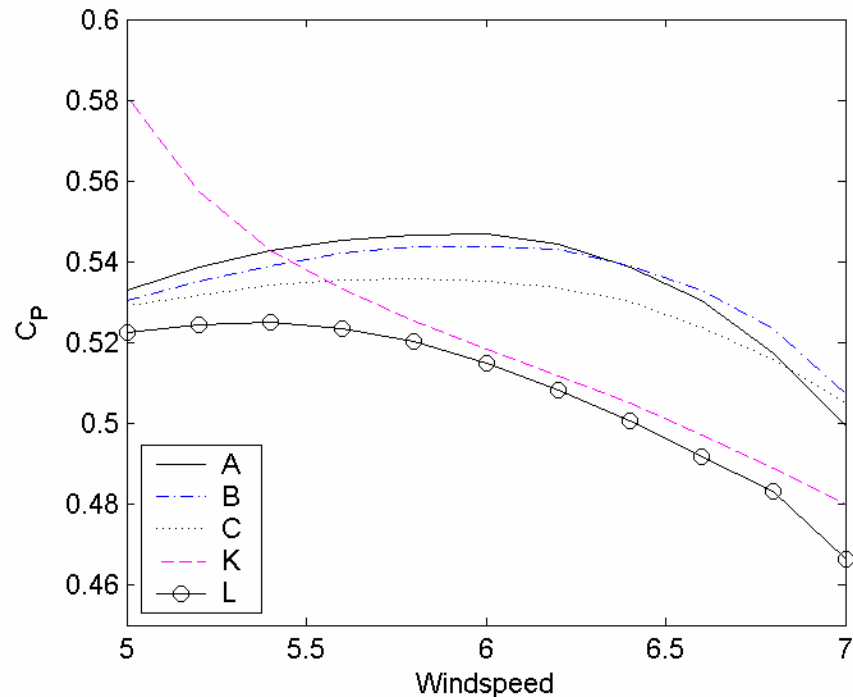


Figure 6.2.21: C_p distribution for designs A, B and C and designs using non-selection profiles

As mentioned, the two-dimensional profiles selected for the above designs did not necessarily obey all the design requirements. Compared to the optimised airfoils for each station, these profiles were not designed for maximum L/D_{area} values and did not necessarily obey the C_{lmax} constraints. As a result, it was difficult for the optimiser to maximise aerodynamic performance and maintain a constant circulation over the blade. This is certainly true in the case of design K. Design L did maintain more or less constant circulation, but to the detriment of the performance.

The profiles optimised for the Weibull designs were designed for sustained performance over a variety of windspeeds and angles of attack. In contrast, the non-selection profiles exhibit L/D ratios which peak and then drop over the operating regime. Furthermore, the maximum lift coefficients of the optimised profiles were set up such that there would be smooth transition from one station to next. As a result, designs K and L display decreased C_p values compared to the Weibull designs, even though these designs were subjected to the same rotor optimisation parameters. Thus it is clear that optimisation of a rotor design for sustained performance over a range of windspeeds is much aided by careful selection of airfoil profiles.

6.2.4 Off-Design Analysis

The wind rotor was optimised within the windspeed range of 5 to 7 m/s. However, the off-design characteristics of the optimised rotors need to be evaluated in the ranges of 4 to 5 m/s and 8 to 10 m/s. Figures 6.2.22 and 6.2.23 display the C_p versus windspeed trends for designs A to E, as well as the CSIR rotor. Below the specified windspeed range (refer to Figure 6.2.22) it is noted that designs C, D, and E

tend to pick up power sooner than designs A, B and CSIR. At 4 m/s, the useful C_p values in the region of 0.48 to 0.495 are produced.

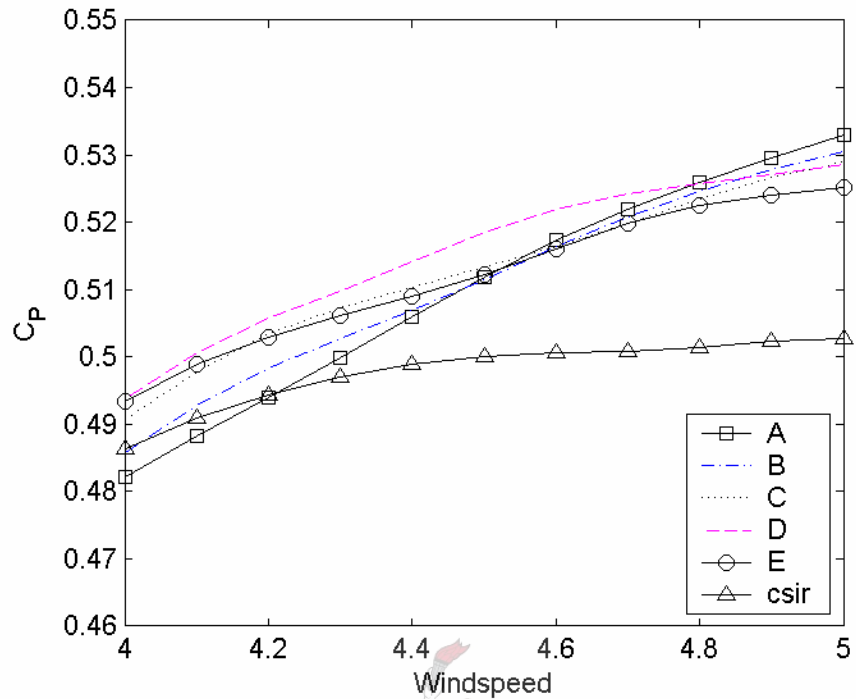


Figure 6.2.22: Top five performances below the design range

Figure 6.2.23 displays the C_p values above the specified windspeed range. Designs A, B, C and E differ only slightly in performance, while design D is lower than these. All the designs yield a steadily decreasing trend, such that at 10 m/s the average C_p value equals 0.31, compared to the average 0.54 C_p value of design B in the design range. The rotors experience a drop in their L/D ratio values and finally stall conditions as the windspeeds increase above their design range. The optimised rotors maintain C_p values approximately 20% higher than the CSIR values. Assuming that the rpm of the rotor is fairly constant and the windspeed increases much more rapidly, the incidence angles at the rotor will increase. The angles of attack experienced by the rotors in higher windspeed conditions are much greater than those angles experienced in the lower windspeed range. The airfoil profiles at root, mid, semi and tip station are in stall conditions for most of this higher windspeed range.

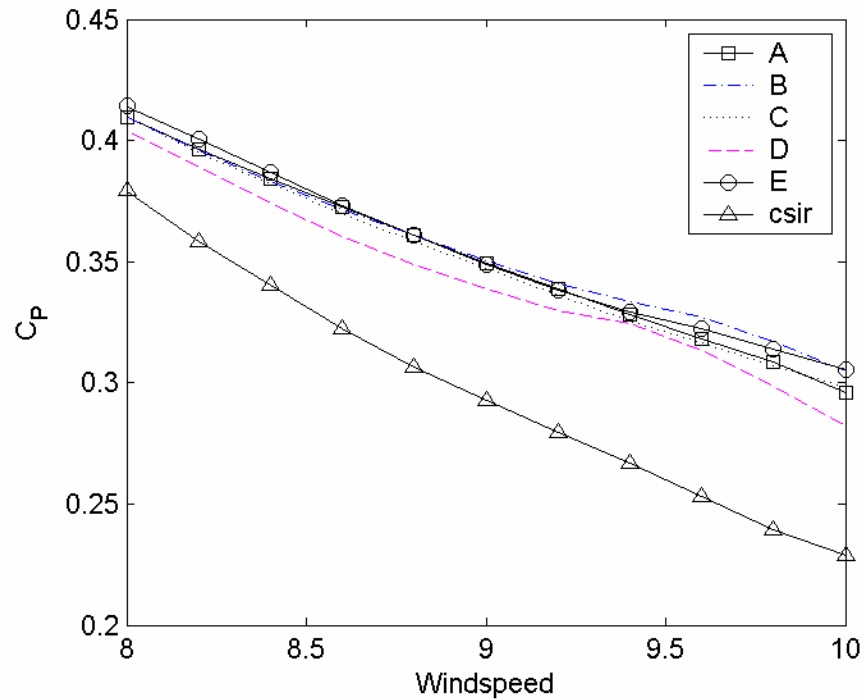


Figure 6.2.23: Top five performances above the design range

Considering the present discussion of higher windspeeds, and greater angles of attack, the influence of changes to the rotational speed of the rotor, should be mentioned. The design specifications prescribed that the rotor should operate at a fixed rotational velocity of 80 rpm. The design results exhibit rotor concepts optimised for this condition. However, post-examination of the rotor results has yielded the opinion that the rpm chosen was indeed too low. The struggle for this rotor optimisation has been the selection of a pitch angle distribution such that favourable angles of attack are experienced across the windspeed range. Given the rotational velocity of 80 rpm, an increasing windspeed causes the flow angles to increase at a certain gradient. However, given a higher rpm, the rate at which the flow angles increase across the windspeed range is lower. In hindsight, this would have been more favourable for the design requirement of sustained performance over a range of windspeeds. Nevertheless, the project goal of obtaining maximum utility from the available wind within certain design conditions has been successful, as evidenced by the rotor results displayed here. Revision of those design conditions would lead to an entirely different solution.

7 CONCLUSION

In this design project, an analytical design for a small-scale, stall-regulated horizontal axis wind turbine blade has been achieved. The challenge for this project was to apply mathematical optimisation methods such that the wind turbine blade would produce peak aerodynamic performance when subjected to the reference Weibull frequency distribution within the windspeed range of 5 to 7 m/s. Furthermore, the new design has been compared with an existing wind turbine blade designed by the CSIR for maximum C_p at a certain windspeed. The project has only given consideration to the aerodynamic design of the wind turbine. The final optimised wind turbine blade is displayed in Figure 7.1.

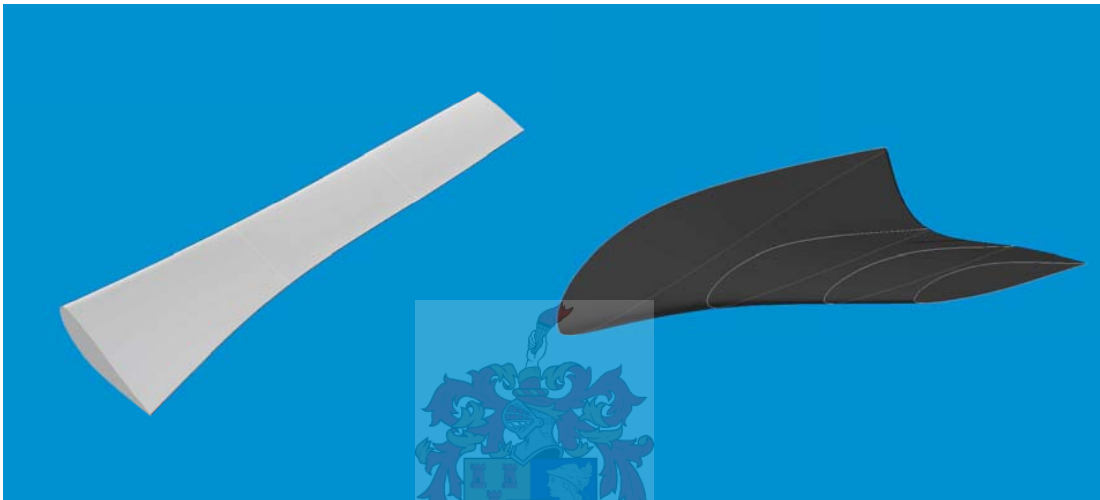


Figure 7.1: Three-dimensional model of the optimised wind turbine blade

In the literature review, the research conducted into the current trends of wind turbine design, with specific focus on the application of optimisation techniques and the difficulty of analysing the wind rotor flowfield, was presented. The research revealed the adequacy of using simplified models in wind turbine design and the priority of using robust analysis techniques in an automated optimisation design process. However, there is continuing progression in the utilisation of more complex analysis theory and applications. Based on the review and the resources available, it was decided to use BEM theory for determining the rotor performance and the viscous/inviscid program, XFOIL, for the two-dimensional analysis. The BEM theory was coded within Matlab and this together with XFOIL, was coupled to an off-the-shelf optimisation package, VisualDOC. The fundamental theories of rotor aerodynamics and optimisation are presented.

A brief outline of XFOIL explained the program's applicability within wind turbine design and the adaptation of XFOIL to the optimisation process. Since XFOIL is a component of an automated and iterative process controlled by the optimiser, VisualDOC, the airfoil generation and analysis functions had to be simplified to ensure successful operation of XFOIL. Though this is a compromise in the accuracy of the analyses, it affords consistency and computational economy to the optimiser. Assuming that the shortcomings of the analysis program are fairly constant, the inaccuracy becomes irrelevant within the optimisation process, since the nature of optimisation is that each design is improved relative to the next.

The design approach details the orchestration of a design model applicable within the optimisation process, to achieve the stated design project objective. The three-bladed wind rotor is simulated as a single blade with four radial stations. The solution strategy was to first optimise the four radial airfoil profiles, and then to consider the full three-dimensional blade. This resulted in five separate optimisation problems. The wind rotor design objective was translated into sub-objectives for each of the profile optimisation problems. The requirement on a broad operating region over a range of windspeeds was translated into the requirement of high lift-to-drag ratios over a wide range of angles of attack for the airfoil profile. The circulation over the blade was kept constant by stipulating a $C_{l_{max}}$ constraint at each radial station, starting with 1.8 at the root and decreasing to 1.2 at the tip. Slow transition to stall was enabled by constraining the nose-down pitching moment. The root station was given the specific requirement to produce high lift under start-up conditions, while the stall regulation function of the wind rotor was specifically catered for by the tip profile. The description of the geometry of the airfoils followed a simple strategy to aid the optimisation design process. New geometries were created by blending from five base airfoil profiles according to different blending fractions.

Solution of each optimisation problem required that the optimiser carry out a number of optimisation tasks. Each task represented a different optimisation method (SQP, MMFD, PSO) or a different optimisation set-up (step size, or initial design variables) and each presented a feasible solution for the problem.

7.1 Profile Optimisation

Four optimised profiles, their geometric and aerodynamic characteristics were presented in section 6.1. A selection of base profiles was provided for each radial station optimisation problem. These profiles were selected for their compliance with the respective objectives and constraints. Other profiles were included to add geometric diversity to the selection. The airfoil designs for each station were stipulated to maintain a decreasing $C_{l_{max}}$ constraint from the blade root to tip. Consequently it should be noted that the optimised airfoil maximum camber decreases from root to tip. The root profile is 50 to 60% thicker than the other optimised profiles for the purpose of generating high lift and as a benefit to the structural integrity of the blade. The mid and semi profiles were designed to have efficient operation over a large range of angles of attack, as is evident by their rounded noses. The tip airfoil has a sharper nose to ensure stall-regulation of the wind turbine blade.

Optimisation of the root profile resulted in a well-resolved solution space, since two tasks in this section that used different optimisation methods to one another resulted in similar optimum designs. The $C_{l_{max}}$ values of the task designs were below 1.8 and occurred at angles of attack of 12° to 13° . The sample of base profiles were quite diverse in shape, thus enabling the optimiser to conduct a more thorough examination of the solution space for the root profile. The optimised root profile constituted three airfoils. Foils 2 and 5 had their $C_{l_{max}}$ values in the region of 1.6 while the rest of the base foils were in the region of 1.3 to 1.4. The third profile, foil 6, had a low $C_{l_{max}}$ and the lowest L/D_{area} value however was favoured due to its reasonably high camber. Due to the need for a high-lift airfoil, it was found that the optimiser systematically isolated the lower-cambered foils from the various optimisation tasks.

Unfortunately, there was not substantial correlation between the optimisation tasks for the mid profile. Most of the final airfoils presented had varied percentage compositions of the base foils and it was difficult to decide upon the most influential design variables. There was only one particularly prominent base profile in three task solutions. This profile, foil 1 produced a high L/D_{area} value and adhered to the C_{lmax} constraint. The foil was quite bulky with high values for maximum thickness and maximum camber. For the optimised mid profile, foil 1 was blended with foils 3 and 5. Foil 3 similarly had a high L/D_{area} value and high maximum camber, but was thinner than foil 1. Foil 5 was the thinnest airfoil and its only favourable aerodynamic characteristic was its low pitching moment, which must have been beneficial for slow transition to stall. Only one optimisation task managed to maintain the C_{lmax} constraint of 1.4 and produce a good value for the objective. Better results for this section would have been obtained if more suitable base profiles had been selected.

The five tasks presented in the semi profile optimisation yielded objective values which were within 0.4% of one another. Their resultant lift coefficient and lift-to-drag ratio distributions were very much the same as well. The semi profile and mid profile design problems used the same base profiles except for the exchange of foil 3 and the absence of the mid profile's foil 6. Three tasks using different optimisation methods and initial conditions managed to converge to the same solution, thus providing confirmation of the final solution. Similar to the case of the mid profile, foil 1 featured strongly in the percentages of the final semi airfoils. In the optimised semi profile, the bulky foil 1 with maximum thickness and maximum camber was blended with the exchanged foil 3. Foil 3 was the thinnest airfoil and its aerodynamic characteristics were not considered the most suitable for the optimisation problem. Nevertheless, the combination of these two foils was the preferred blend in the semi profile optimisation problem. Similar to the mid profile optimisation problem, the remaining base profiles did not feature in the semi optimisation tasks.

Of notable interest in both the mid and semi optimisation tasks was the evidence of a particular base profile (foil 2) which had the most favourable aerodynamic characteristics, but received close to zero inclusion in the final design profiles. Though given a variety of initial percentages, foil 2 was simply not recognised by the optimiser as a suitable design variable. This was attributed to foil 2's lack of exceptional geometric features relative to the sample base of profiles.

The selection of base profiles for the tip profile optimisation problem were quite varied and thus the optimisation tasks yielded a good mixture of base profiles, with the optimised tip profile constituting four profiles - foils 1, 3, 5 and 6. Furthermore, the solution space was well resolved with three different tasks converging to a similar solution. Foils 3 and 5 had favourable L/D_{area} and constraint values and thus featured in all of the optimisation tasks. These foils had their positions of maximum camber and maximum thickness further back along the chord than the other base foils. At increased velocities and angles of attack this length breaks down the boundary layer on the upper surface and this aids stall regulation. Foils 1 and 6 did not maintain the C_{lmax} constraint, but did have a high average of L/D ratios in the angle of attack range. Base foils 2 and 4 were not significantly considered in any of the optimisation tasks. These foils had the lowest values for the aerodynamic objective. Examining the lift coefficient trend, the final optimised tip profile sustained a plateau equal to 1.2 after 10° angle of attack. For the objective of stall

regulation, it would be better to see the C_i values drop away after attaining 1.2, however this requirement was not designed into the objectives for the optimisation problem.

Though the method of blending applied in the profile optimisation problems was robust and easily adaptable to the automated optimisation process, the method did have one or two disadvantages. As a result of the blending process, the optimiser tended to favour the combination of airfoils with diverse geometric characteristics. This meant that the prime aerodynamic candidates would often share their influence in the final optimised airfoil with much less suitable base profiles, those with low objective values or non-adherence of the constraints. These were known as the diversity foils in the base profile selection and were selected for their geometric shape and not their aerodynamic characteristics. This phenomenon was most evident in the mid and semi optimisation problems. In the case of the root and tip optimisation problems, the base profiles were quite diverse. Consequently, the individual geometric characteristics related to a profile's aerodynamic performance were not lost in the blending method.

Another disadvantage of this method, was that the optimiser was not able to segregate the good and bad characteristics of the base profile, and then only use the good. A single weighting was applied to the entire airfoil shape and this shape then combined with another airfoil. Furthermore, the final product often lacked the uniqueness of the parent airfoils. Evidence of the predecessors individual features are still visible in the final product, however, these are much more subtle.

Nevertheless, the optimiser has succeeded in manipulating the blending method such that four airfoils have been optimised for operation at the root, mid, semi and tip stations. All of these airfoils outperform their sample of base foils.

7.2 Rotor Optimisation

Optimisation of the full three-dimensional rotor was the last of the five optimisation problems to be conducted. The airfoils optimised for operation at the root, mid, semi and tip stations were used during the rotor optimisation. In total there were ten optimisation tasks presented. These were the eight Weibull-weighted designs (designs A to H), and the designs using non-selection profiles (K and L). Firstly, the implementation of the Weibull wind distribution was successful. Those rotor designs with higher C_{Pobj} values showed a clear tendency to produce larger C_p values between the windspeeds of 5 and 6 m/s, and then lower C_p values between 6 and 7 m/s. This is a replication of the Weibull trend model.

Examination of the resultant chord length distributions showed only slight variation between optimised designs A to H. The chord length distribution was tightly constrained due to the requirement of constant circulation over the blade. This constraint was imposed to minimise losses at the hub and tip, and thus improve the wind rotor's capability to extract energy out of the available windstream. The only outlier in the chord length distribution plot was a design which did not have the constant circulation constraint. The pitch angle distributions displayed the characteristic exponential decrease from root to tip. Designs F and H which did not exhibit this trend, tended to yield unsatisfactory aerodynamic performance based on their C_p values. The pitch angle distribution tended to have a more remarkable influence over the final rotor performance than the chord length, as can be seen by the greater variation of the pitch angles among the eight rotor designs.

The lift-to-drag ratios vs. windspeed of each design were plotted at each radial station. Higher pitch angles at the root and mid stations yielded flatter L/D ratio vs windspeed profiles compared to those designs with lower pitch angles at these stations. Consistent L/D ratios were not evident at the semi and tip stations, since the regions of power-producing range of these airfoils are much smaller than at the root and mid stations. At the semi and tip stations, high pitch angles produced higher L/D ratios at the top-end of the windspeed range. The L/D plots of the top five designs did not differ much from each other at the root and mid stations. Differences between the designs were more evident at the semi and tip stations. Evidently, the best rotor designs gained their advantage over the other designs at the semi and tip stations. If a rotor design's L/D ratios at these stations replicated the Weibull trend, the rotor design achieved a higher C_{pobj} value.

Comparison between best design B and worst design H at each radial station proved that selecting the operating points at lower windspeeds to fall in the power-producing section of the airfoil profile improved the aerodynamic performance of the rotor design remarkably.

The optimisation tasks using non-selection profiles tended to converge with difficulty and did not conform to the Weibull trend very well. The optimiser was less successful in finding a high-performance rotor design using these profiles. Keeping the circulation constant along the blades turns out to be much more difficult when using airfoil profiles which have not been selected with the whole airfoil family performance borne in mind. Using these non-selection airfoils resulted in a discontinuous lift and drag coefficient distribution along the blade and a decreased performance over the range of windspeeds. The profiles optimised for the Weibull designs were designed for sustained performance over the operating regime. Since the non-selection profiles did not exhibit this same characteristic it was much more difficult to design the rotor for sustained performance. Airfoil profile selection is a crucial part of the wind rotor design process.

Examining the performance of the top five designs outside of the design windspeed region showed a decrease in aerodynamic performance "off-design". Below the design windspeed range, the C_p values were still quite useful and indicate the possibility of a cut-in windspeed of 4 m/s. Above the design windspeed range, the C_p values were much lower. At windspeeds greater than 7 m/s, the airfoil profiles at root, mid, semi and tip station begin to experience stall conditions.

The top five rotor designs, A to E, managed to improve on the performance of the CSIR design. When comparing the analytical analyses, designs A to E yielded C_p values approximately 7.5% higher than the CSIR design at low windspeeds, and 12.0% higher C_p values at windspeeds of 6 to 7 m/s. The reasons for the CSIR's lower aerodynamic performance were attributed to the smaller chord lengths existing at the radial stations, and the use of a single airfoil profile at all of the stations. Though the CSIR design exhibited a much larger pitch angle distribution than the rotor designs, this fact could not be assessed independently due to the difference in airfoil profiles. However, investigation into the lift-to-drag ratios revealed that the CSIR design maintained a level L/D ratio vs. angle of attack trend. This in itself is a good characteristic for consistent wind turbine operation, however, the average magnitude of the L/D ratios were too low to compete with the optimised rotor designs.

Post-examination of the rotor results has yielded the opinion that the rpm chosen should have been higher. The design specifications prescribed that the rotor should operate at a fixed rotational

velocity of 80 rpm. The design results exhibit rotor concepts optimised for this condition. The struggle for this rotor optimisation has been the selection of a pitch angle distribution such that favourable angles of attacks are experienced across the windspeed range. The flow angles increase rapidly at all four stations, as the windspeed increases. However, at a higher rpm, these flow angles increase less dramatically, thus allowing one pitch angle setting to be more effective at maintaining optimal angles of attack at the radial stations. The project goal of obtaining maximum utility from the available wind within certain design conditions has been successful, as evidenced by the rotor results displayed here. Revision of those design conditions would lead to an entirely different solution.

7.3 Optimisation Methodology

The Sequential Quadratic Programming (SQP) method yielded good designs within a short iteration time. SQP was much more successful at finding the global optimum than in the case of the Modified Method of Feasible Direction (MMFD) and Sequential Linear Programming (SLP) methods. This is evident by comparing optimisation tasks with the same initial design variables, but differing results. Optimisation tasks using these methods often converged to a local optimum, even when using more function evaluations than the SQP method. Furthermore, the tasks employing SQP methods were more likely to correlate with one another and the Particle Swarm Optimisation (PSO) tasks. PSO by far conducted the most thorough investigations of the solution space. This is the benefit of a large number of iterations.

Specifically in the case of the profile optimisation problems, the condition of the solution space was such that there were many local optima. Using gradient methods required careful selection of the relative step size such that local optima could be over-stepped and a more global solution found. Further evidence of these local optima was found when selecting trust parameters for the PSO tasks. Selecting a c_1 value greater c_2 leads to greater trust in the particle self. The optimisation task was more likely to converge to a local optimum in these cases.

7.4 Recommendations for Future Work

- When new airfoils are generated by blending shape functions, it is advisable to include basic shapes, such as triangles, amongst the airfoils. This allows the optimiser to conduct localised changes to the new airfoil, as opposed to the entire foil being altered.
- An investigation of the solution space for the profile optimisation (similar to what was done for the rotor optimisation in Appendix A.5) enables the user to understand the influence of each design variable on the optimisation objective and thus understand the progress of the optimiser during each iteration. This aids the user to select realistic design variables for the optimiser to use. Furthermore, the solution space provides insight into the most suitable optimisation methods to be used.

- The present method of optimising four separate radial profiles, and thereafter the rotor, actually constricts the optimiser. A much more complete optimisation project would be to optimise the entire wind rotor with the airfoil profiles as design variables, thus optimising the profiles and the rotor at the same time. This becomes a much more complex project requiring careful consideration of constraints and airfoil design variables, nevertheless it should produce a globally optimised rotor.
- The flow field surrounding a wind turbine can be improved by careful selection of the fixed rotational speed. Using a faster rotational speed, increases the range of favourable flow angles experienced at the radial stations. This allows a single pitch angle selection to provide advantageous angles of attack for the airfoil profile.
- It is not advisable to use XFOIL 6.94 in an automated design process. The program responds better to user prompts as opposed to a generic input file. In this project, the analyses of the airfoils had to be simplified so as to produce repeatable results. Furthermore, wind turbine airfoils are designed to operate at the maximum lift-to-drag ratios which are at or near stall. XFOIL 6.94 is not adept at solving airfoils in this region. Optimisation design using Computational Fluid Dynamics (CFD) as the flow solver increases the accuracy of the design process, however the analyses become much more time-consuming. Another version of XFOIL, called RFOIL, is specifically adapted to account for rotational effects and may be better suited to wind turbine airfoil design.
- Build and test the wind turbine model. Experimental data is extremely useful as a verification tool. This was noted when analysing the experimental data from the CSIR and NWU projects.

8 REFERENCES

- Akmandor, I.S., Ekici, K., "Airfoil Analysis for Horizontal Axis Wind Turbines," *AIAA Journal*, 98-0020
- Benini, E., Toffolo, A., "Optimal Design of Horizontal-Axis Wind Turbines Using Blade-Element Theory and Evolutionary Computation," *Journal of Solar Energy Engineering*, Vol. 124, Nov 2002, pp. 357-363
- Bermúdez, L., Velázquez, A., Matesanz, A., "Viscous-inviscid method for the simulation of turbulent unsteady wind turbine airfoil flow," *Journal of Wind Engineering and Industrial Aerodynamics* 90 (2002) pp. 643-661
- Bermúdez, L., Velázquez, A., Matesanz, A., "Numerical Simulation of Unsteady Aerodynamics Effects in Horizontal-Axis Wind Turbines," *Solar Energy* Vol. 68, No. 1 (2000), pp. 9-21
- Bruining, A., Timmer, W.A., "Airfoil Characteristics of Rotating Wind Turbine Blades," *Journal of Wind Engineering and Industrial Aerodynamics* 39 (1992) pp. 35-39
- Bosman, J.J., "The Aerodynamic and Structural Design of a 1kW Wind Turbine Blade," *WWEA Conference Paper*, 2003.
- British Wind Energy Association, "Wind Energy for the Eighties," Peter Peregrinus Ltd., Stevenage UK and New York, 1982.
- Buhl, M.K. Jnr., Wright, A.D., Tangler, J.L., "Wind Turbine Design Codes: a Preliminary Comparison of the Aerodynamics," National Renewable Energy Laboratory, CP-500-23975, 17th ASME Wind Energy Symposium, Jan 1998
- Butterfield, C.P., Scott, G., Musial, W., "Comparison of Wind Tunnel Airfoil Performance Data With Wind Turbine Blade Data," *Journal of Solar Energy Engineering*, Vol. 114, May 1992, pp. 119-124
- Chaviaropoulos, P., Bouras, B., Leoutsakos, G. and Papailiou, K.D., "Design of Optimised Profiles for Stall-Regulated HAWTs Part1: Design Concepts and Method Formulation," *Wind Engineering*, Vol. 17, No. 6, 2001, pp. 275-287
- Chattot, J.J., "Optimization of Wind Turbines Using the Helicoidal Vortex Model," *Journal of Solar Engineering*, Vol. 125, Nov 2003, pp 418-424
- Craig, K.J., Venter, P.J., de Kock, D.J., Snyman, J.A., "Optimisation of structured grid spacing parameters for separated flow simulation using mathematical optimisation," *J. Wind Eng. Ind. Aerodyn.* 80 (1999) pp. 221-231
- Denton, T.S.A., "STEP Report: A Wind Turbine for South Africa," CSIR Research Report, December 2003.
- Devinant, Ph, Laverne, T., Hureau, J., "Experimental Study of Wind-Turbine Airfoil Aerodynamics in High Turbulence," *Journal of Wind Engineering and Industrial Aerodynamics* 90 (2002) pp. 689-707
- Drela, M., "XFOIL: An Analysis and Design System for Low Reynolds Number Airfoils," MIT Dept. of Aeronautics and Astronautics, *Lecture Notes in Engineering*, No. 54, 1989, pp.1-12
- Drela, M. "Pros and Cons of Airfoil Optimisation," Chapter in *Frontiers of Computational Fluid Dynamics*, ISBN 981-02-3707-3, 1998
- Drela, M., "XFOIL 6.94 User Guide," MIT Aero & Astro, Harold Youngren, Aerocraft, Inc., 10 Dec 2001
- Drela, M., "Integral Boundary Layer Formulation for Blunt Trailing Edges," *AIAA Journal*, 89-2166-CP
- Du, Z., Selig, M.S., "The Effect of Rotation on the Boundary Layer of a Wind Turbine Blade," *Renewable Energy* 20 (2000) pp. 167 - 181

- Du, Z., Selig, M.S., "A 3D Stall-Delay Model for Horizontal Axis Wind Turbine Performance Prediction," *AIAA Journal*, 98-0021
- Foussekis, D., Fraunié, P. and Béguier, C., "Steady and Unsteady Separated Flows Around a Profile. Application on the Wind Turbines," *Journal of Wind Engineering and Industrial Aerodynamics* 39 (1992) pp. 41-49
- Fuglsang, P., and Madsen, H.A., "Optimization Method for Wind Turbine Rotors," *Journal of Wind Engineering and Industrial Aerodynamics* 80 (1999) pp. 191-206
- Giguère, P., Selig, M.S., Tangler, J.L., "Blade Design Trade-offs using Low-Lift Airfoils for Stall-Regulated HAWTs," *ASME Wind Energy Symposium*, Jan 1999.
- Goliger, A.M., Retief, J.V., "Identification of Zones of Strong Wind Events in South Africa," *Journal of Wind Engineering and Industrial Aerodynamics*, 90 (2002) pp. 1227-1235
- Habali, S.M., and Saleh, I.A., "Design and Testing of Small Mixed Airfoil Wind Turbine Blades," *Renewable Energy*, Vol. 6, No. 2, 1995, pp. 161 - 169
- Hansen, A.C., and Butterfield, C.P., "Aerodynamics of Horizontal Axis Wind Turbines," *Annual Review of Fluid Mechanics*, Vol 25, March 1993, pp. 115-149
- Hansen, M.O.L., "Aerodynamics of Wind Turbines," James & James (Science Publishers) Ltd., London, UK, 2000
- Hicks, R.M., Vanderplaats, G.N., Murman, E.M., King, R.R., "Airfoil Section Drag Reduction at Transonic Speeds by Numerical Optimisation," NASA Center for AeroSpace Information (CASI) SAE PAPER 760477, Apr, 1976, 13p
- Huyer, S.A., Simms, D. and Robinson, M.C., "Unsteady aerodynamics associated with a horizontal-axis wind turbine," *AIAA Journal*, Vol. 34, No. 7, July 1996, pp. 1410-1419
- Jackson, K.L., Migliore, P.G., "Design of Wind Turbine Blades Employing Advanced Airfoils," WestWind Industries Inc., 1986
- Malcolm, D.J., Hansen, A.C., "WindPACT Turbine Rotor Design, Specific Rating Study," NREL/SR-500-34794, Nov 2003
- Magnusson, M., "Near-wake behaviour of Wind Turbines," *Journal of Wind Engineering and Industrial Aerodynamics* 80 (1999) pp. 147-167
- Massardo, A., Satta, A., Marini, M., "Axial Flow Compressor Design Optimisation: Part II - Throughflow Analysis," *Journal of Turbomachinery*, July 1990, Vol. 112 pp. 405 - 410
- Parkinson, G.V., "A Tolerant Wind Tunnel for Industrial Aerodynamics," *Journal of Wind Engineering and Industrial Aerodynamics* 16 (1984) pp. 293-300
- Patterson, G.N., "Ducted Fans: Design for High Efficiency," *Australian Council for Aeronautics*, Report ACA-7, July 1944
- Peng, G., Shuliang, C., Masaru, I., Hayama, S., "Design Optimisation of axial flow hydraulic turbine runner: Part II - multi-objective constrained optimisation method," *International Journal for Numerical Methods in Fluids*, 2002; 39:533-548.
- Quinn, G., Venter, G., Ozen, M., "Geometry Optimization of a Chemical Vapor Deposition Reactor," Vanderplaats Research and Development, Colorado Springs, CO.
- Ronsten, G., "Static Pressure Measurements on a Rotating and a Non-rotating 2.375m Wind Turbine Blade. Comparison with 2D Calculations," *Journal of Wind Engineering and Industrial Aerodynamics* 39 (1992) pp. 105-118

- Selig, M.S., and Coverstone-Carroll, V.L., "Application of a Genetic Algorithm to Wind Turbine Design," *Transactions of ASME*, Vol. 118, March 1996, pp. 22-28.
- Selig, M.S., and Maughmer, M.D., "Generalised Multipoint Inverse Airfoil Design," *AIAA Journal*, Vol. 30, No. 11, 1992, pp. 2618-2625.
- Selig, M.S., and Maughmer, M.D., "Multipoint Inverse Airfoil Design Method Based on Conformal Mapping," *AIAA Journal*, Vol. 30, No. 5, 1992, pp. 1162-1170.
- Somers, D.M., and Maughmer, M.D., "Theoretical Aerodynamic Analyses of Six Airfoils for Use on Small Wind Turbines," NREL/SR-500-33295, June 2003
- Sørensen, N.N, Hansen, M.O.L., "Rotor Performance Predictions Using A Navier-Stokes Method," *AIAA Journal*, 98-0025
- Spera, D.A., "Wind Turbine Technology, Fundamental Concepts of Wind Turbine Engineering," *ASME Press*, USA, New York, 1995
- Stork, C.H.J., Butterfield, W., Holley, W., Madsen, P.H., Jensen, P.H., "Wind Conditions for Wind Turbine Design Proposals for Revision of the IEC 1400-1 Standard," *Journal of Wind Engineering and Industrial Aerodynamics* 74-76 (1998) pp. 443-454
- Tangler, J.L., "The Nebulous Art of using 2D wind tunnel results for 3D performance prediction, " *NREL/CP-500-31243*, Jan 2002
- Timmer, W.A., van Rooij, R.P.J.O.M., "Summary of the Delft University Wind Turbine Dedicated Airfoils," *Transactions of ASME*, Vol. 125, Nov 2003, pp. 488-496
- Timmer, W.A., van Rooij, R.P.J.O.M., "Thick Airfoils for HAWTs," *Journal of Wind Engineering and Industrial Aerodynamics* 39 (1992) pp. 151-160
- Tuncer, I.H., Wu, J.C., Wang, C.M., "Theoretical and Numerical Studies of Oscillating Airfoils," *AIAA Journal*, Vol. 28, No. 9, Sep 1990
- Vanderplaats, G.N., "Efficient Algorithm for Numerical Airfoil Optimization," *Journal of Aircraft*, Vol. 16, No. 12, Dec 1979, pp. 842-847
- Vanderplaats, G.N., "Numerical Optimisation Techniques for Engineering Design," Vanderplaats Research & Development Inc., Third Edition, Fourth Printing, Colorado Springs, 2001
- Venter, G., Sobieszcanski-Sobieski, J., "Multidisciplinary Optimization of a Transport Aircraft Wing using Particle Swarm Optimization," *AIAA Journal*, 2002-5644
- Voutsinas, S.G., Rados, K.G., Zervos, A., "On the Effect of the Rotor Geometry on the Formation and the Development of its Wake," *Journal of Wind Engineering and Industrial Aerodynamics* 39 (1992) pp. 283-291
- White, F.M., "Fluid Mechanics, " McGraw Hill International Editions, 4th Edition, Singapore, 1999
- White, F.M., "Viscous Fluid Flow, " McGraw Hill International Editions, 2nd Edition, Singapore 1991
- Wilson, R.E., and Lissaman, P.B.S., "Applied Aerodynamics of Wind Power Machines," *National Science Foundation*, Oregon State University (May 1974)
- Wood, D.H., "Some Effects of Finite Solidity on the Aerodynamics of Horizontal-Axis Wind Turbines," *Journal of Wind Engineering and Industrial Aerodynamics* 26 (1987) pp. 255-273
- Wright, A.K., Wood, D.H., "The Starting and Low Wind Speed Behaviour of a Small Horizontal Axis Wind Turbine," *Journal of Wind Engineering and Industrial Aerodynamics* 92 (2004) pp. 1265-1279

APPENDICES

A.1 Generation of New Airfoils

XFOIL has an inbuilt function, INTE, which interpolates two source airfoil shapes into an “intermediate” shape. The user supplies the coordinate files of the two airfoils and a weighting factor or blending fraction. In order to conduct the interpolation accurately, both source airfoil coordinates are translated to a reference set of coordinates and thereafter combined with the specified weighting factor. Thus, the interpolated airfoil's x coordinates at a given normalized spline parameter are a weighted average of the two source airfoil x coordinates at the same normalized spline parameters. This normalized spline parameter runs from zero at the leading edge to one at the trailing edge on both upper and lower surfaces of the profile. This same process occurs with the y coordinates. The summation of these translated coordinates result in the interpolated airfoil:

$$M = (1 - b)X + bY \quad (\text{A.1.1})$$

M is the interpolated airfoil. X and Y are the source airfoil coordinates and b is the weighting factor. Extrapolation as opposed to interpolation, occurs when the weighting factor is greater than one.

As mentioned, the interpolation function only combines two source airfoils at a time. However, the generation of an airfoil within the optimisation process requires the blending of five base profiles according to the following function:

$$Y = a_1Y^1 + a_2Y^2 + \dots + a_nY^n \quad (\text{A.1.2})$$

The Y^n define the shape functions which represent the base airfoil profiles. a_1, \dots, a_n apply percentage weightings to the shape functions. In order to blend five profiles, the INTE command is carried out in four stages. Each stage after the first, interpolates a source airfoil with the previously blended airfoil. To apply this staggered method of blending, the percentage weighting of each source airfoil is algebraically transformed into a suitable blending ratio for XFOIL to use. The blending ratios were calculated according to equation (A.1.3). A to C are the base profile coordinate files. a to c are the respective percentage weightings of each base profile. r_1 to r_2 are the blending fractions calculated for input into XFOIL.

$$aA + bB + cC + \dots = [(1 - r_1)A + r_1B](1 - r_2) + r_2C \dots \quad (\text{A.1.3})$$

As a demonstration of XFOIL's interpolation function, two source airfoils were blended for three different blending fractions - 0.8, 0.2, 1.8. The source airfoils are the RAF-6D and the NACA 4412 profiles. The blended airfoil in Figure A.1.1 constitutes 20% of the RAF-6D and 80% of the NACA 4412. The blended airfoil resembles the NACA 4412 much more closely than the RAF-6D. In Figure A.1.2, the blending fraction is switched to 0.2. The result is that the geometry of the interpolated airfoil tends more towards the RAF-6D shape, while only representing 20% of the NACA 4412.

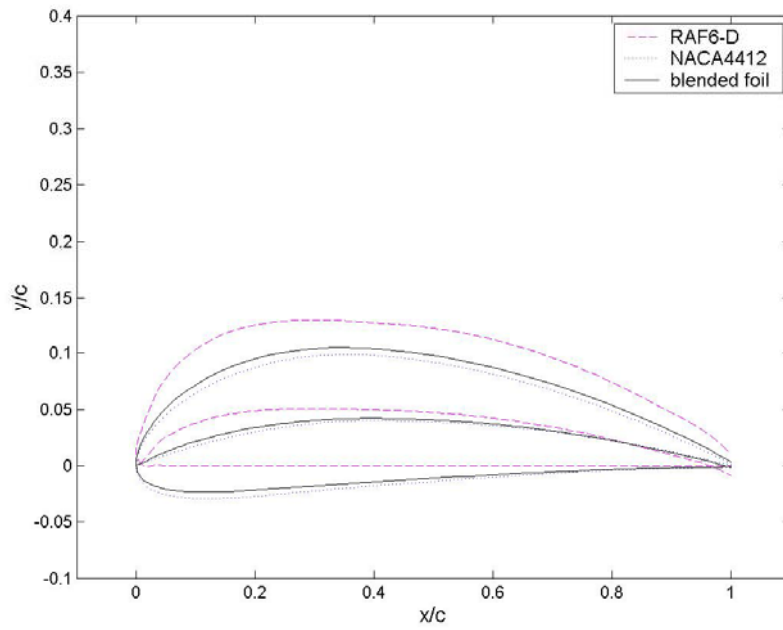


Figure A.1.1: Interpolation using a blending fraction of 0.8

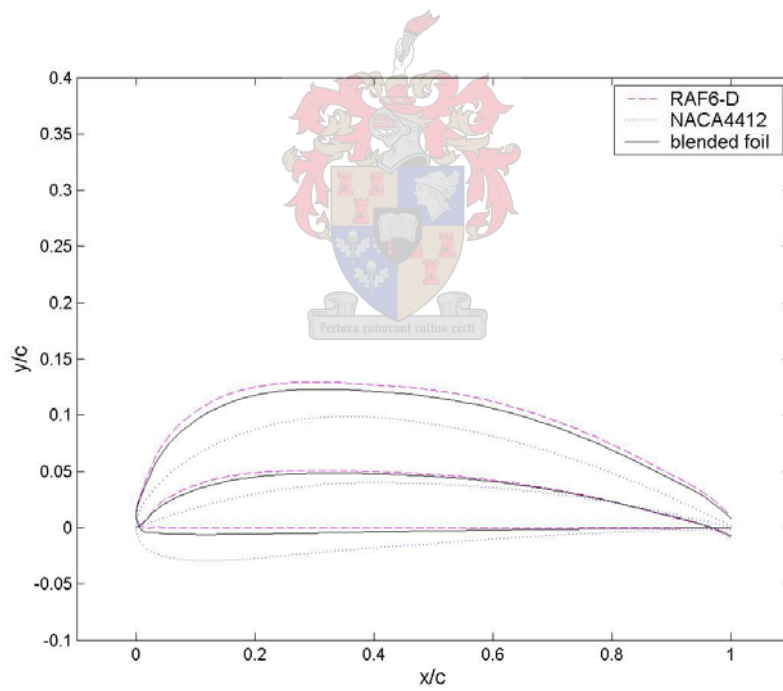


Figure A.1.2: Interpolation using a blending fraction of 0.2

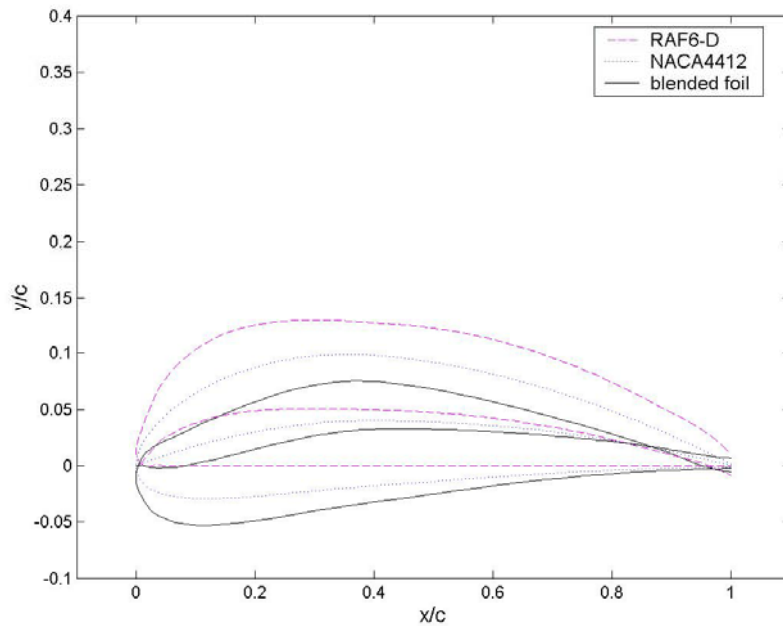


Figure A.1.3: Extrapolation using a blending fraction of 1.8

The above Figure, A.1.3, shows the source airfoils and the interpolated foil resulting from a blending fraction of 1.8. Here it is evident that extrapolation has occurred. The NACA 4412 coordinates are multiplied by a factor of 1.8 while those of the RAF-6D are multiplied by -0.8 (refer to equation A.1.2). The resultant blended foil is unconventional and will certainly cause convergence problems during analysis. For this reason, the blending fractions were maintained below the value of one.

There are other methods for airfoil modification. One of these is contained within the GDES (Geometry Design Routine) menu of XFOIL. GDES employs direct manipulation techniques which enable the user to set the leading edge radius, trailing edge gap, maximum thickness, maximum camber, and positions of maximum thickness and camber. GDES allows the user to directly change specific attributes of a profile, by setting dimension for the leading edge radius, or maximum camber, etc. However, using the INTE command will cause a change of the entire geometry of the airfoil, since the coordinates of one airfoil are blended with another. Though using the GDES command would have been preferable, it was not possible to set this up in a robust automation process.

Table A.2.1: Root profile

Profile	Area	Max thickness	@ x/c	Max camber	@ x/c	r _{LE}	$\Delta\theta_{TE}$ [°]
foil 1	0.1062	0.1700	0.2770	0.0301	0.3760	0.0211	9.55
foil 2	0.0685	0.1002	0.3230	0.0555	0.4970	0.0153	5.22
foil 3	0.1880	0.3010	0.3080	-0.0133	0.0840	0.0395	25.58
foil 4	0.1527	0.2265	0.3390	0.0344	0.4020	0.0245	55.32
foil 5	0.1400	0.2200	0.2940	0.0808	0.3960	0.0578	8.54
foil 6	0.1756	0.2713	0.3370	0.0463	0.2530	0.0356	26.94
foil 7	0.1543	0.2659	0.2880	0.0284	0.7960	0.0276	1.66
optim foil	0.1238	0.1914	0.3160	0.0633	0.3880	0.0286	11.69

Table A.2.2: Mid profile

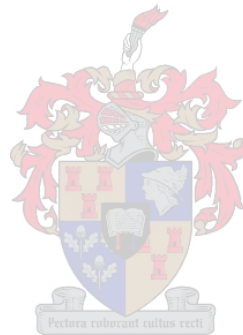
Profile	Area	Max thickness	@ x/c	Max camber	@ x/c	r _{LE}	$\Delta\theta_{TE}$ [°]
foil 1	0.116	0.176	0.371	0.044	0.435	0.021	2.080
foil 2	0.103	0.150	0.304	0.040	0.404	0.025	19.560
foil 3	0.070	0.130	0.235	0.060	0.315	0.036	7.340
foil 4	0.137	0.212	0.339	0.031	0.402	0.027	32.790
foil 5	0.070	0.100	0.362	0.020	0.387	0.008	7.340
foil 6	0.140	0.220	0.294	0.081	0.396	0.058	8.540
optim foil	0.100	0.158	0.303	0.048	0.370	0.025	5.370

Table A.2.3: Semi profile

Profile	Area	Max thickness	@ x/c	Max camber	@ x/c	r _{LE}	$\Delta\theta_{TE}$ [°]
foil 1	0.116	0.176	0.371	0.044	0.435	0.021	2.08
foil 2	0.103	0.150	0.304	0.040	0.404	0.025	19.56
foil 3	0.057	0.091	0.311	0.038	0.401	0.008	3.50
foil 4	0.137	0.212	0.339	0.031	0.402	0.027	32.79
foil 5	0.070	0.100	0.362	0.020	0.387	0.008	7.34
optim foil	0.096	0.147	0.352	0.042	0.422	0.014	3.46

Table A.2.4: Tip profile

Profile	Area	Max thickness	@ x/c	Max camber	@ x/c	r _{LE}	$\Delta\theta_{TE}$ [°]
foil 1	0.063	0.097	0.339	0.028	0.371	0.007	1.410
foil 2	0.081	0.131	0.274	0.010	0.266	0.006	8.610
foil 3	0.134	0.210	0.394	0.026	0.472	0.025	7.510
foil 4	0.154	0.266	0.288	0.028	0.796	0.028	1.660
foil 5	0.074	0.121	0.309	0.046	0.309	0.006	108.100
foil 6	0.096	0.129	0.129	0.053	0.053	0.010	39.320
optim foil	0.104	0.160	0.365	0.033	0.365	0.011	14.280



A.3 Calculations

A.3.1 Structural Verification

When considering the structural design of a wind turbine, it is necessary to design for the worst case. This would be the extreme windspeed. The extreme windspeed is calculated from the IEC 50 year model for wind turbines within wind class IV (Spera, 1995). Calculations are made for the wind turbine parked.

The extreme windspeed experienced by a wind turbine is calculated at a certain elevation relative to the height of the turbine rotor. For this wind turbine $R = 3.7$ m and it is assumed that $h_{hub} = 10$ m.

$$\begin{aligned} h &= h_{hub} + \frac{2}{3}R \\ &= 10 + \frac{2}{3}(3.7) \\ &= 12.467\text{m} \end{aligned} \tag{A.3.1.1}$$

The extreme windspeed, v_{2s} , is calculated according to the following expression:

$$\begin{aligned} v_{2s} &= v_b k_t \left(\ln \frac{h}{z_o} + 3 \right) \\ &= (27)(0.17) \left(\ln \frac{12.467}{0.01} + 3 \right) \\ &= 46.489\text{m/s} \end{aligned} \tag{A.3.1.2}$$

where the following constants are applied (Hansen, 2000):

v_b is the basis wind speed = 27 m/s

k_t is the terrain factor related to the roughness length = 0.17

z_o is the roughness length = 0.01

Therefore, the dynamic pressure in the windstream is calculated as follows:

$$\begin{aligned} q_{2s} &= \frac{1}{2} \rho v_{2s}^2 \\ &= \frac{1}{2} (1.0303) (46.489)^2 \\ &= 1113.341\text{Pa} \end{aligned} \tag{A.3.1.3}$$

The axial loading is calculated using a force coefficient, $C_f = 1.5$, obtained from the Danish standard for wind turbines (Spera, 1995).

$$\begin{aligned} p(r) &= q_{2s} C_f c(r) \\ &= (1113.341)(1.5)c(r) \\ &= 1670.012c(r) \end{aligned} \tag{A.3.1.4}$$

The loading is calculated in terms of $c(r)$ which is the chord length distribution relative to the span of the blade.

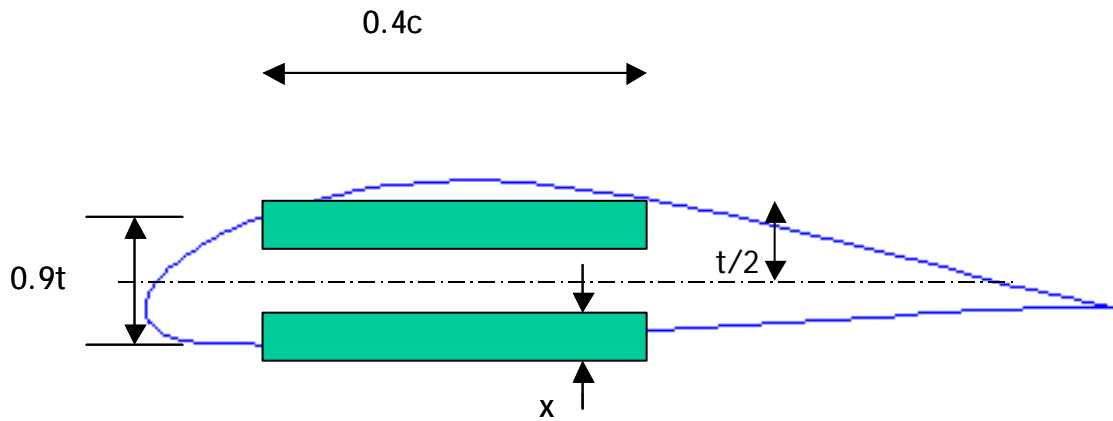


Figure A.3.1.1: I-beam model of airfoil

The bending moment is calculated according to standard beam theory and is calculated for the hub:

$$\begin{aligned}
 M &= \int_{r_{hub}}^R rp(r)dr \\
 &= \frac{1}{2}1670.012c_{hub}(R^2 - r_{hub}^2) \\
 &= Ac_{hub}
 \end{aligned}
 \tag{A.3.1.5}$$

Where A is a temporary constant substituted to simplify the expression.

Furthermore, it is known that:

$$\begin{aligned}
 \sigma &= \frac{M \frac{t}{2}}{I} \\
 I_{hub} &= \frac{M \frac{t}{2}}{\sigma} = \frac{Ac_{hub}t}{2\sigma}
 \end{aligned}
 \tag{A.3.1.6}$$

The moment of inertia can be calculated directly from Figure A.3.1.1:

$$\begin{aligned}
 I &= \frac{2}{3}(0.4c)\left[\frac{t^3}{2} - \left(\frac{t}{2} - x\right)^3\right] \\
 &= \frac{4}{15}c\left[\frac{t^3}{2} - \left(\frac{t}{2} - x\right)\left(\frac{t^2}{2} - tx + x^2\right)\right] \\
 &= \frac{4}{15}c\left(2\frac{t^2}{2}x - \frac{t}{2}x^2 + \frac{t^2}{2}x - 2\frac{t}{2}x^2 + x^3\right) \\
 &= \frac{4}{15}c\left(3\frac{t^2}{2}x - 3\frac{t}{2}x^2 + x^3\right) \\
 &= \frac{4}{15}c\left(\frac{3}{4}t^2x - \frac{3}{2}tx^2 + x^3\right)
 \end{aligned}
 \tag{A.3.1.7}$$

Equating (A.3.1.6) and (A.3.1.7) results in a polynomial expression for the thickness, t .

$$\begin{aligned} \frac{Ac_{hub}t}{2\sigma} &= \frac{4}{15}c_{hub}\left(\frac{3}{4}t^2x - \frac{3}{2}tx^2 + x^3\right) \\ 0 &= \frac{3}{15}xt^2 - \left(\frac{2}{5}x^2 + \frac{A}{2\sigma}\right)t + \frac{4}{15}x^3 \\ \{t &= \frac{-b \pm \sqrt{b^2 - 4ac}}{2a}\} \\ t &= \left[\frac{2}{5}x^2 + \frac{A}{2\sigma} \pm \sqrt{\left(\frac{2}{5}x^2 + \frac{A}{2\sigma}\right)^2 - 4\left(\frac{3}{15}x\right)\left(\frac{4}{15}x^3\right)} \right] \left(\frac{15}{2(3x)}\right) \end{aligned} \quad (A.3.1.8)$$

Taking the maximum bending stress for E-glass to be $\sigma = 220(10^6)\text{Pa}$ and the skin thickness $x = 0.01\text{ m}$, the minimum thickness for the hub profile can be calculated from equation (A.3.1.8):

$$\begin{aligned} A_{root} &= \frac{1670.012}{2} \left(3.7^2 - (0.2 \times 3.7)^2 \right) \\ &= 10973.98 \\ t_1 &= 0.02765\text{m} \\ t_2 &= 0.00482\text{m} \end{aligned}$$

Therefore, the minimum thickness allowed for the root profile is 27.65 mm.

The constraints on the chord length allows it to have a maximum of 0.8 m and a minimum of 0.2 m. Using the minimum constraint for the chord length, the absolute minimum thickness-to-chord ratio can be determined:

$$\begin{aligned} \frac{t}{c_{min}} &= \frac{0.02765}{0.2} \\ &= 0.138 \end{aligned}$$

The optimised root profile is satisfactorily above this limit. Refer to table A.3.1.

A.3.2 Weibull Wind Distribution

For an annual average windspeed of 6.26 m/s at a height of 9.1 m over level terrain, the reference Weibull frequency distribution is represented by the following function:

$$f_U = \left(\frac{8.760}{C}\right) k \left(\frac{U}{C}\right)^{k-1} \exp\left[-\left(\frac{U}{C}\right)^k\right] \quad (A.3.2.1)$$

where C and k are scaling constants specific to the terrain, and U is the windspeed. From the reference distribution, $C = 7.07\text{ m/s}$ and $k = 2.29$ and $U = [5:0.2:7]\text{ m/s}$.

The normalised frequency distribution is described by equation A.3.2.2.

$$nf_U = \left(\frac{C}{8.760}\right) f_U \quad (A.3.2.2)$$

A.4

Program Code

A.4.1 BEM program

```

% *****
% Evaluation of performance of rotor blade:
% INPUTS: R = constant
%         rpm = constant
%         a,b = factors for chord distribution, des variable
%         pitch L's = twist distribution, des variable
% OUTPUT: CP(1:11) for each windspeed
%         ratio root(1:11), ratio mid(1:11), ratio semi(1:11), ratio tip(1:11)
%         chord (1:4) - calculated from a,b
%         CP_obj
%         variance(1:11)
% *****

function [RESP]=designperf(DVAR)
close all
ac = 0.25;
R = DVAR(1); % 3.7
rpm = DVAR(2); % 80
bb = DVAR(3);
aa = DVAR(4);
pitchvec = DVAR(5:8);
B = 3; % no of blades
visc = 15.69e-06;
rho = 1.0303;
w = rpm*pi/30; %rad/s
Vo = 5:0.2:7;
tpsd = w*R./Vo;
loop = length(Vo);
% Radius distribution along span of blade, r is the ratio r/R
r=[0.2,0.500,0.750,0.95];
chord = aa.*r.^bb;
r = r.*R; % radius distribution in [m]
rhub = 0.1*R;
dr(1) = (r(2)+r(1))/2 - rhub; % delta r from one station to next
for i = 2:3
    dr(i) = (r(i+1)+r(i))/2-(r(i)+r(i-1))/2;
end
dr(4) = R-(r(3)+r(4))/2;
% *****
% Initialise matrices/vectors for calculations
% *****
rmat = zeros(4,loop);
chordmat = zeros(4,loop);
Vmat = zeros(4,loop);
ax = zeros(4,loop); at = zeros(4,loop);
RE = zeros(4,loop);
rmat(1,:) = r(1); rmat(2,:) = r(2);
rmat(3,:) = r(3); rmat(4,:) = r(4);
chordmat(1,:) = chord(1); chordmat(2,:) = chord(2);
chordmat(3,:) = chord(3); chordmat(4,:) = chord(4);
alfmat = zeros(4,loop); flowLmat = zeros(4,loop);
pitch = zeros(4,loop);
pitch(1,:) = pitchvec(1); pitch(2,:) = pitchvec(2);
pitch(3,:) = pitchvec(3); pitch(4,:) = pitchvec(4);

```

```

clmat = zeros(4,loop); cdmat = zeros(4,loop);
tolat = zeros(4,loop); tolax = zeros(4,loop);
axnew = zeros(4,loop); atnew = zeros(4,loop);
CT = zeros(4,loop);
ratio = zeros(4,loop);
Fmat = zeros(4,loop);
drmat = zeros(4,loop);
drmat(1,:) = dr(1); drmat(2,:) = dr(2);
drmat(3,:) = dr(3); drmat(4,:) = dr(4);
% *****
% Initialise induction factors using analytical formulae
% *****
for jj = 1:4          %no radial stations
    Vmat(jj,:) = Vo;
    for j = 1:loop    % 11
        x = w*r(jj)./Vo(j);
        c = 3*x^2-9;
        d = 1-x^2;
        coeff=[-16 24 c d];
        z = roots(coeff);
        z = sort(z);
        ax(jj,j) = z(2);
        at(jj,j) = (1-3.*ax(jj,j))./(4.*ax(jj,j)-1);
    end
end
iter = 1;
axmat = cell(1,5);
axmat{1} = ax;
atmat = cell(1,5);
atmat{1} = at;
while iter < 5
    % *****
    % Calculate ANGLES OF ATTACK
    % *****
    flowLmat=atan((1-ax).*Vmat./((1+at).*w.*rmat));
    flowLdeg = flowLmat*180/pi;          % in degrees
    alfmat = flowLdeg-pitch;
    % *****
    % Calculate Reynolds no
    % *****
    Vrot = w.*rmat.*(1+at);
    Vax = Vmat.*(1-ax);
    Vrel = sqrt(Vrot.^2 + Vax.^2);
    RE = chordmat.*Vrel/visc;
    RE = round(RE);
    remin = min(RE)/100000;          % gives the min RE at station for windspd range
    remax = max(RE)/100000;
    remin = floor(remin)*100000;    % gives the max RE at station for windspd range
    remax = ceil(remax)*100000;
    % *****
    % Interpolate CL and CD from xfoil data
    % First interpolate values at true alpha for RE data files
    % Then interpolate true RE between vectors created above
    % *****
    for i = 1:4
        rerange = remin(i):50000:remax(i);    %data files only have Re in 50000 increments
        tempcl = zeros(length(rerange),loop);
        tempcd = zeros(length(rerange),loop);
        if i==1
            nam=['c:\OPT\polars\optim_foils\rootfoil-RE'];

```

```

end
if i==2
    nam=['c:\OPT\polars\optim_foils\midfoil-RE'];
end
if i==3
    nam=['c:\OPT\polars\optim_foils\semifoil-RE'];
end
if i==4
    nam=['c:\OPT\polars\optim_foils\tipfoil-RE'];
end
for j = 1:length(rerange)
    filenam = [nam num2str(rerange(j)) ' Type1'];
    sol = dlmread(filenam, ',', 12, 0);
    tempcl(j,:) = spline(sol(:,1),sol(:,2),alfmat(i,:));
    tempcd(j,:) = spline(sol(:,1),sol(:,3),alfmat(i,:));
end
for n = 1:loop
    clmat(i,n)=spline(rerange,tempcl(:,n),RE(i,n));
    cdmat(i,n)=spline(rerange,tempcd(:,n),RE(i,n));
end
end
% *****
% Full blade calculations using BEM
% *****
circ = 0.5*w.*rmat.*clmat.*chordmat;
variance = var(circ); % constraint on variance of circulation over blade
f = B/2*(R-rmat)./(rmat.*sin(flowLmat));
F = 2/pi.*acos(exp(-f)); % Prandtl's tip loss factor
solid = chordmat*B./(2*pi.*rmat);
cn = clmat.*cos(flowLmat)+cdmat.*sin(flowLmat);
ct = clmat.*sin(flowLmat)-cdmat.*cos(flowLmat);
% *****
% Recalculate induction factors
% *****
atnew = (4.*F.*sin(flowLmat).*cos(flowLmat)./(solid.*ct) - 1).^ -1;
k = 4*F.*sin(flowLmat).^2./(solid.*cn);
for i = 1:loop
    for ii = 1:4
        if ax(ii,1) <= ac % Glauert's correction for high values of ax induction factor
            axnew(ii,i) = (k(ii,i) + 1)^ -1;
        else
            axnew(ii,i) = 0.5*(2+k(ii,i)*(1-2*ac)- sqrt(((k(ii,i)*(1-2*ac)+2)^2 + 4*(k(ii,i)*ac^2-1))));
        end
    end
end
tolax = abs(ax - axnew);
tolat = abs(at - atnew);
ax = axnew; % Start next iteration using ind factor from previous
at = atnew;
iter = iter+1;
axmat{iter} = ax;
atmat{iter} = at;
end
% *****
% Calculate coeff of power according to Euler's turbine equ
% *****
x = w.*rmat./Vmat;
dx = w.*drmat./Vmat;
CT = (1-axnew).^2.*cn.*solid./(sin(flowLmat).^2);

```

```

Ft=0.5*rho*Vrel.^2.*chordmat.*(clmat.*sin(flowLmat)-cdmat.*cos(flowLmat));
dM=rmat*B.*Ft.*drmat;
dP=w.*dM;
P=sum(dP);
CP=sum(dP)./(0.5*rho*pi*R^2*Vo.^3);
CP_obj=weight(Vo,CP);
ratio = clmat./cdmat;
RESP(1:11) =CP;
RESP(12:22) = ratio(1,:);
RESP(23:33) = ratio(2,:);
RESP(34:44) = ratio(3,:);
RESP(45:55) = ratio(4,:);
RESP(56:59) = chord;
RESP(60) = CP_obj;
RESP(61:71) = variance;

```

A.4.2 XFOIL code

```

load C:\OPT\foils\sg6043.dat
pane
gdes
cadd

pane
oper
Type
1
iter
100
visc
RE
400000.
vpar
n 6
vacc 0.001

PACC
C:\OPT\outputfiles\output

ASEQ 0 15 1

QUIT

```

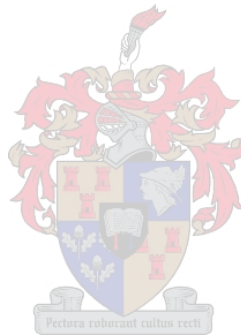


Figure A.4.2.1: Typical input file for XFOIL

Figure A.4.2.1 displays the characteristic input file used during the automated design process. This particular input file loads the SG6043 airfoil, whose coordinate file is contained in the specified directory. The input file then designates certain operations to be carried out. The following is a brief explanation of these operations:

PANE - sets the current-airfoil panel nodes to a default of 140. The panel nodes are based on the curvature of the airfoil.

GDES - opens the geometry design routine menu of XFOIL.

CADD - If the airfoil coordinates have excessively coarse point spacing, additional points are added with this command. CADD enforces point addition at those locations where excessive corner angles between panels exist.

OPER - this is the menu for direct airfoil analysis.

Type 1 - specifies the type of analysis. Type 1 specifies a fixed chord and velocity, while varying the angles of attack.

iter - sets the viscous solution iteration limit. A converged solution must be found before the number of iterations reaches the limit.

visc - toggles the viscous/inviscid analysis mode

RE - sets the Reynolds' no.

vpar - Allows one to change the boundary layer parameters, such as the transition criterion 'n' and the viscous acceleration parameter 'vacc'. This parameter has an influence on the convergence rate of the viscous solution. It sets the minimum viscous acceleration to be considered in the calculation.

PACC - auto point accumulation of the active polar. This provides an output file with C_l , C_d , C_m , top and bottom transition points for each alpha/angles of attack.

ASEQ - prescribes a sequence of angles of attack.

If strong separation bubbles are present in the viscous solution it is important to have good panel resolution in the region of the bubbles. This can be altered by changing the panel density along the surface of the airfoil. In the case of this project, the airfoil generation and analysis is automated so it is not possible for the user to interrupt the program by tweaking the panel density distribution. The default panel density of 140 panels is used.



A.5 Investigation of Solution Space

The objective of this project is to discover a rotor configuration, which allows a small-scale, stall-controlled wind turbine to extract as much energy from the wind as possible, over a range of windspeeds. The rotor configuration is defined by various design variables such as the local pitch angle and chord length at a station along the length of the blade. A change in one of these design variables equates to a change of the rotor configuration, which causes the wind turbine to exhibit a different performance. There are a number of design variables available, with the combinations of these able to generate a large number of possible solutions. The area within which these possible solutions are found, is known as the solution space. To gain insight into this solution space, it is advisable to investigate the influence of each design variable separately. The following section studies the effect of varying a single design variable while keeping the rest constant. Though it will be seen that each case has a maximum C_p at a certain design variable, it is to be noted that these are only local maximums and do not necessarily indicate the global maximum for the design problem. Of importance in this investigation is to discover the extent of influence each design variable has on the C_p and C_{pobj} values. Below is a table of the design variables considered in the analysis of the blade. To simplify the analysis, the RAF-6D profile was used at all four radial stations. As with the rotor optimisation, the rotational speed is constant at 80 rpm.

Table A.5.1: Design variables considered in analysis

Design Variable	Description
V_0	windspeed
p_r	pitch angle at 20% span
p_m	pitch angle at 50% span
p_s	pitch angle at 75% span
p_t	pitch angle at 95% span
b	form factor for chord distribution
a	magnitude factor for chord distribution

A.5.1 Pitch angle at root station

The root pitch angle is allowed to vary between 13° and 25° . The limitations upon the pitch angle range have been selected such that the local angles of attack should not fall below zero nor too far into the stall region of the profile. As can be seen in the three-dimensional surface plot in Figure A.5.1.1, the performance of the blade increases with increasing windspeed. The maximum C_p value is approximately situated at a windspeed of 6.6 m/s and at pitch angles in the range of 18° to 24° , as demonstrated by the plateau in the upper right hand corner of the contour plot in Figure A.5.1.2. The dip in C_p values at high windspeed and between 13° and 16° pitch angles is an indication of the root station being in stall. As the windspeed increases, so do the flow angles. Given a low pitch angle, the root station experiences stall and adversely affects the performance of the rest of the blade. Above 16° , the C_p versus windspeed trend changes only slightly and root pitch angle changes do not have a great effect on the blade performance.

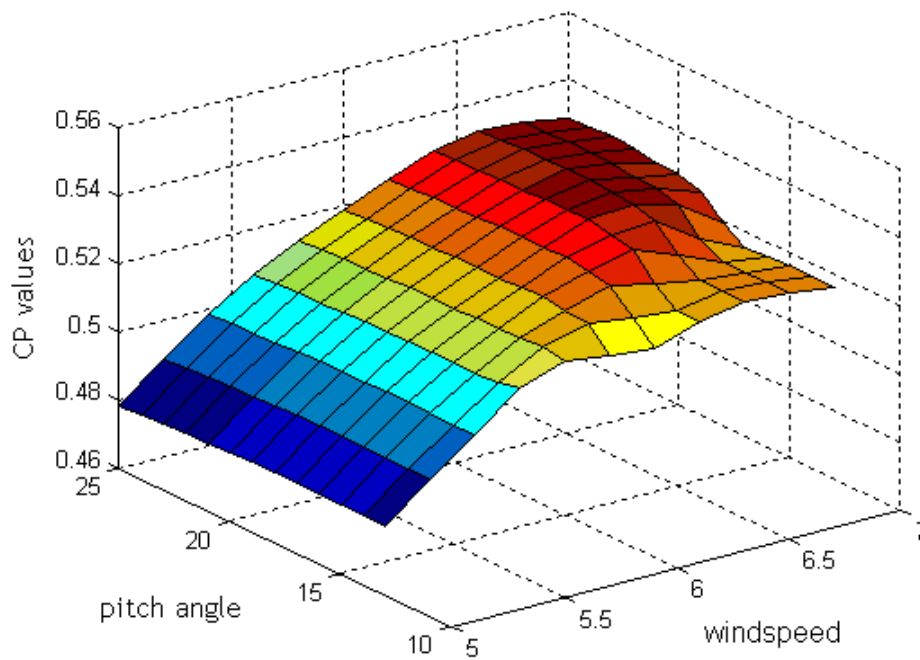


Figure A.5.1.1: Three-dimensional surface plot of C_p versus windspeed and the pitch angle at 20% span

In Figure A.5.1.3, the C_p weighted objective is plotted versus the pitch angle at the root station. While the root pitch angles are low, C_{Pobj} rises steadily reaching an optimum of 0.514 at 20° . For pitch angles greater than this, the C_{Pobj} values barely change. For a two degree increase in the root pitch angle, C_{Pobj} changes by 0.08%. As other parameters in the rotor configuration change, it can be expected that this optimum point will change in magnitude and position.

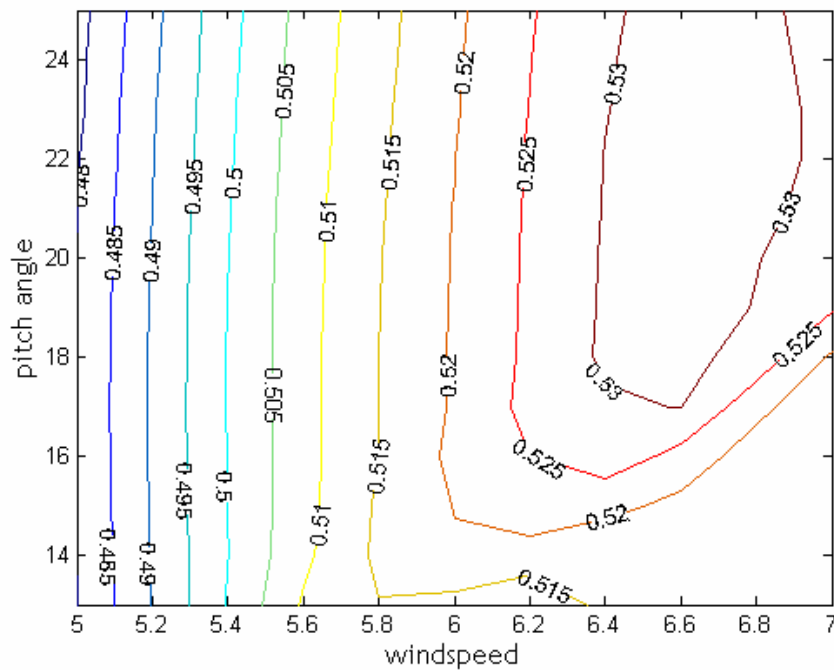


Figure A.5.1.2: Contour plot of C_p values

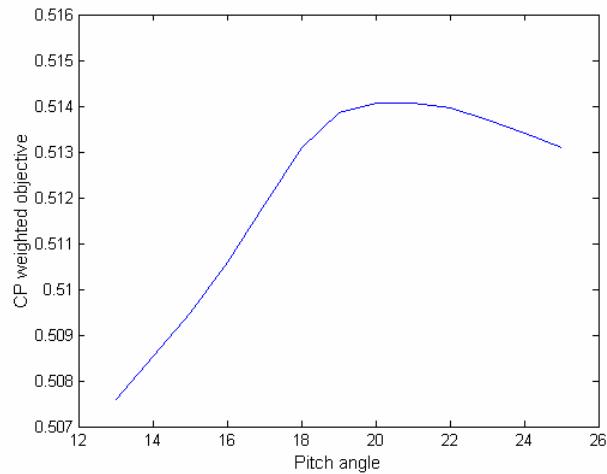


Figure A.5.1.3: The C_p objective function in relation to the pitch angle

A.5.2 Pitch angle at mid station

The mid station pitch angle is allowed to vary between -5° and 11° . Similar to the case where the root pitch angle is varied, the C_p values are seen to increase with increasing pitch angle and windspeed. The contour plot of Figure A.5.2.2 shows that the area of maximum performance is much smaller than in the previous case. Clearly good performance occurs within a narrow margin for the mid pitch angle. The maximum performance appears to lie between 2° and 5° at a windspeed of approximately 6.6 m/s. At low pitch angles, the mid station experiences stall and has a considerable effect on the blade performance.

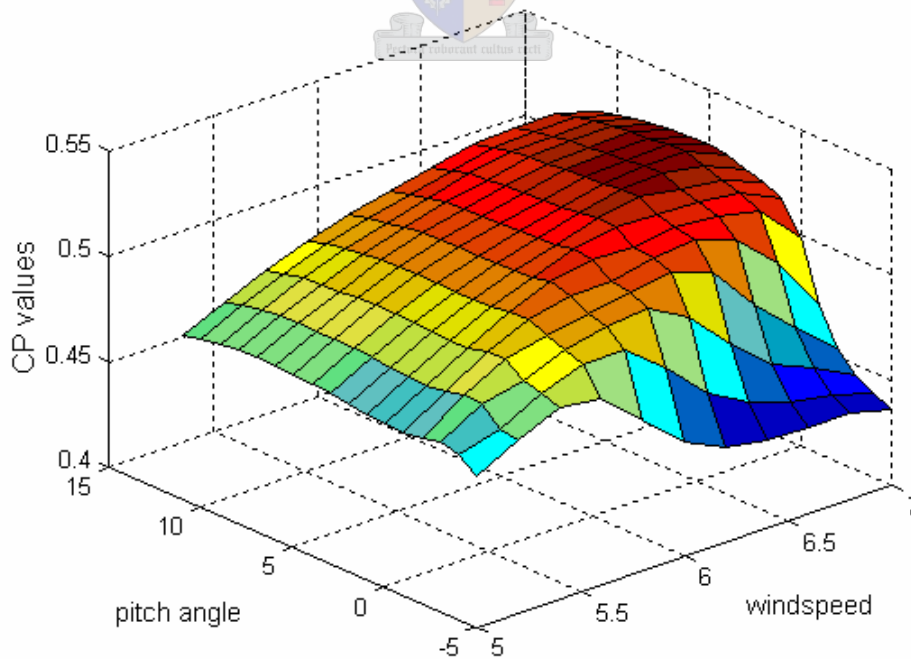


Figure A.5.2.1: Three-dimensional surface plot of C_p versus windspeed and the pitch angle at 50% span

The C_p weighted objective in Figure A.5.2.3 seems to be less peaky than in the case where the root pitch angle was varied. Here, C_{pobj} rises sharply and then maintains a plateau of 0.516. A two degree variance at this plateau produces a 0.19% difference in C_{pobj} values. Thus the mid station pitch angle has a greater influence on the objective than in the case of the root pitch angle variable.

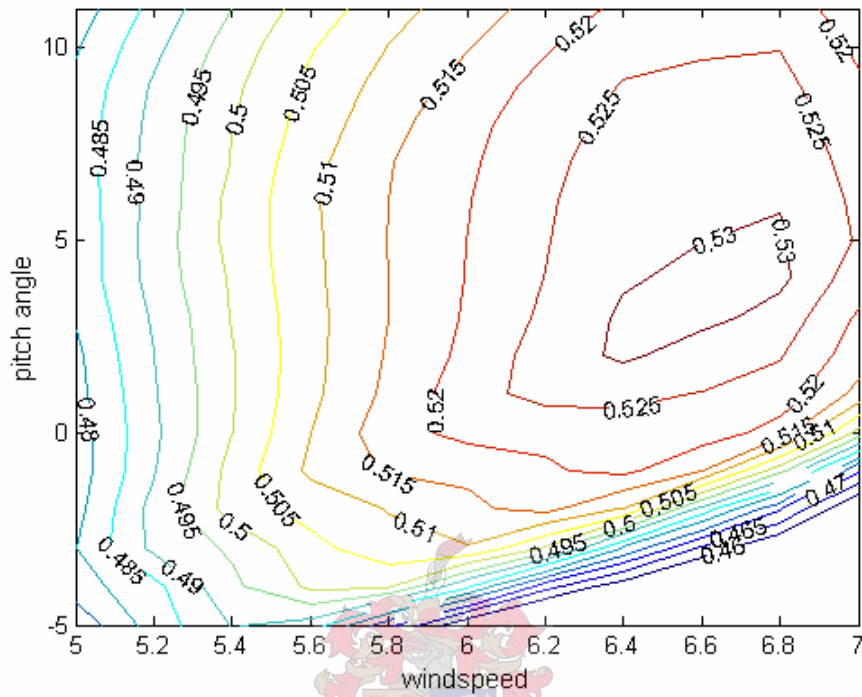


Figure A.5.2.2: Contour plot of C_p values

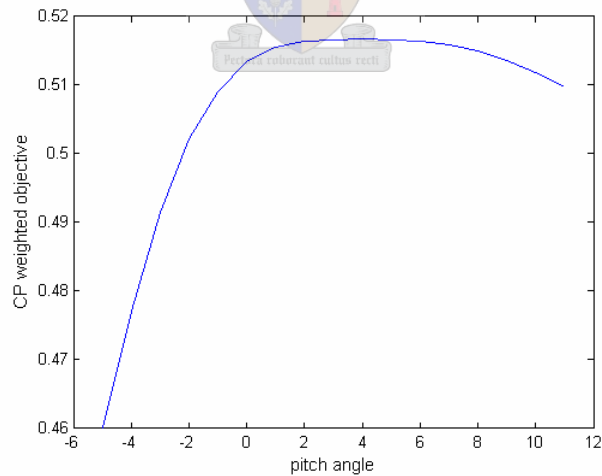


Figure A.5.2.3: The C_p objective function in relation to the pitch angle

A.5.3 Pitch angle at semi station

The pitch angle at the semi station is allowed to vary between -8° and 7° . As the pitch angle increases, the semi station drives the rotor to achieve maximum performance between -2° and 6° pitch angle, at a windspeed of 6.5 m/s. The C_p target area is quite large with the low C_p contours bunched

together at the outskirts of the plot in Figure A.5.3.2. Compared to the mid station, the semi pitch angles allow a larger margin for good rotor performance. Furthermore, the C_p values on average are higher. The stall region at low pitch angles and high windspeed is not as dramatic as in the case of the mid station. However, if the pitch angle range was selected to be lower than -8° , the same dramatic stall affects would have been seen.

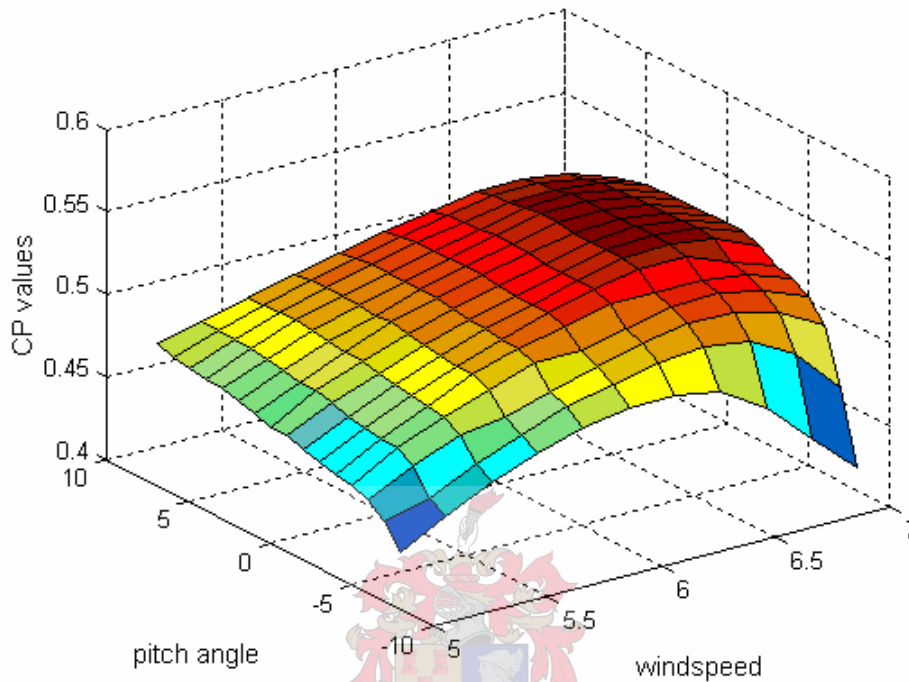


Figure A.5.3.1: Three-dimensional surface plot of C_p versus wind speed and the pitch angle at 75% span

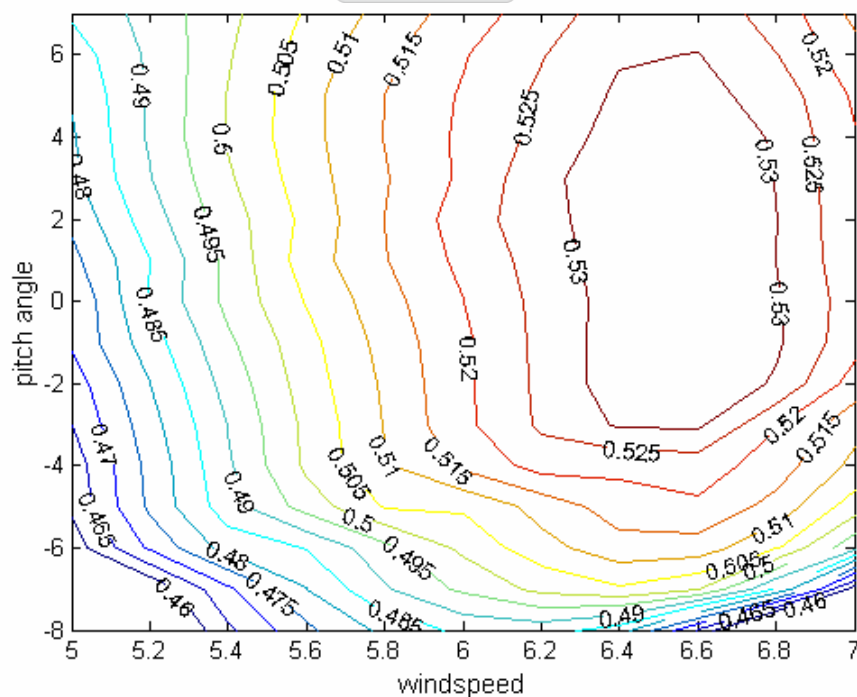


Figure A.5.3.2: Contour plot of C_p values

The overall C_p weighted objective obtains an optimum of 0.517 at approximately 3° . Should the semi pitch angle vary by 2° , the percentage difference to the optimum is 0.58%. The C_{pobj} values remain high for most of the pitch angles in the selected range.

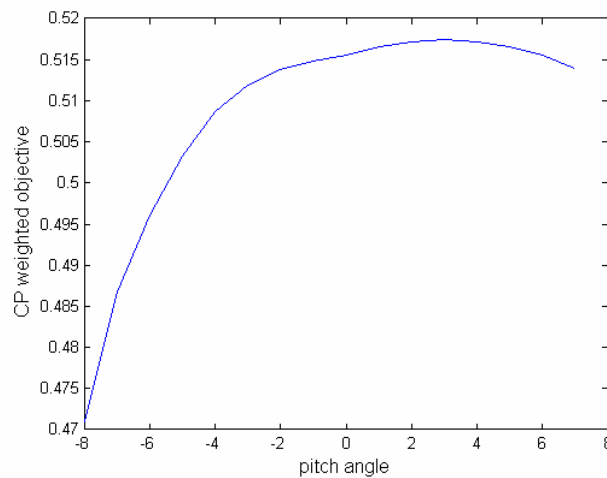


Figure A.5.3.3: The C_p objective function in relation to the pitch angle

A.5.4 Pitch angle at tip station

The range for the pitch angles at the tip station is between -11° and 10° . From Figure A.5.4.1, the C_p values are observed to rise gradually with increasing windspeed and increasing pitch angle. Exception to this occurs at the three visible corners of the surface plot. When the pitch angle is a low negative, -11° , and the windspeeds are 5 and 7 m/s, the tip station exhibits stall conditions due to the angle of attack being high. At higher pitch angles, 10° , the tip station experiences a high performance at a lower angle of attack. This is surprising and could be due to a discontinuity in the analysis of the profile. Nevertheless, it illustrates that the forces at the tip station have a major effect on the rest of the blade due to the location's large moment arm. This also explains why the C_p values are much higher than in the previous cases. Judging by Figure A.5.4.2, the area for best performance lies between 4° and 8° at a windspeed of 6.5 m/s.

In Figure A.5.4.3, the overall performance of the blade (C_{pobj}) increases steadily as the pitch angle is increased. As the pitch angle increases, conditions at the tip station become more and more favourable. Thus, the blade's performance is ever on the increase. Considering the requirement of a stall-regulated turbine, the lift produced at the tip would have to be limited to prevent turbine run-away. The C_{pobj} values reach much higher values in this tip station analysis, than in the other station analyses. After the first inflection point on the curve, a two degree variation in pitch angle produces a 1.16% difference in C_{pobj} . This is the largest difference gain measured at all four stations, proving that the tip station does hold the most influence in determining the blade's performance.

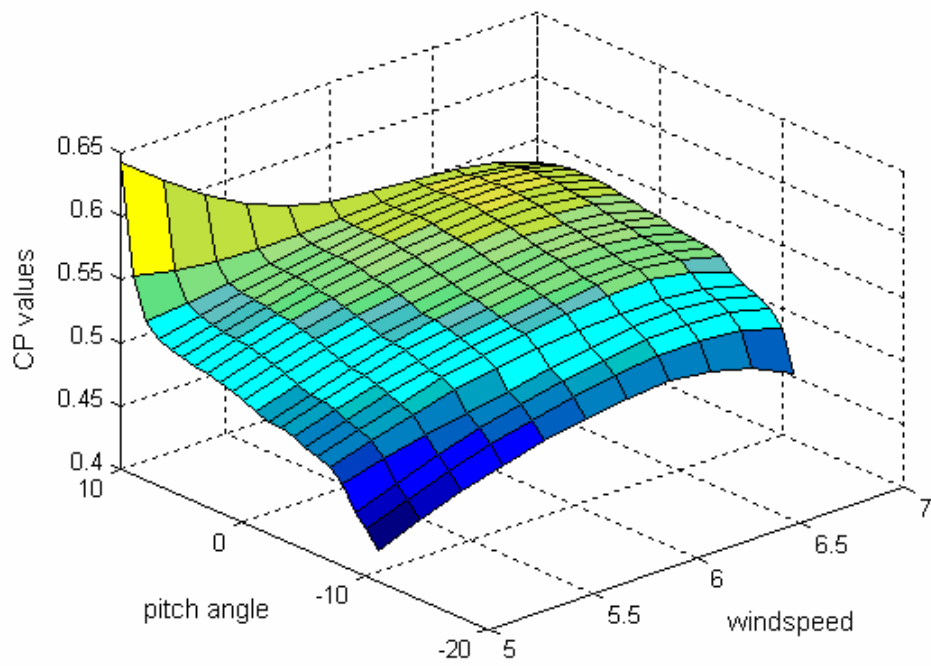


Figure A.5.4.1: Three-dimensional surface plot of C_p versus wind speed and the pitch angle at 95% span

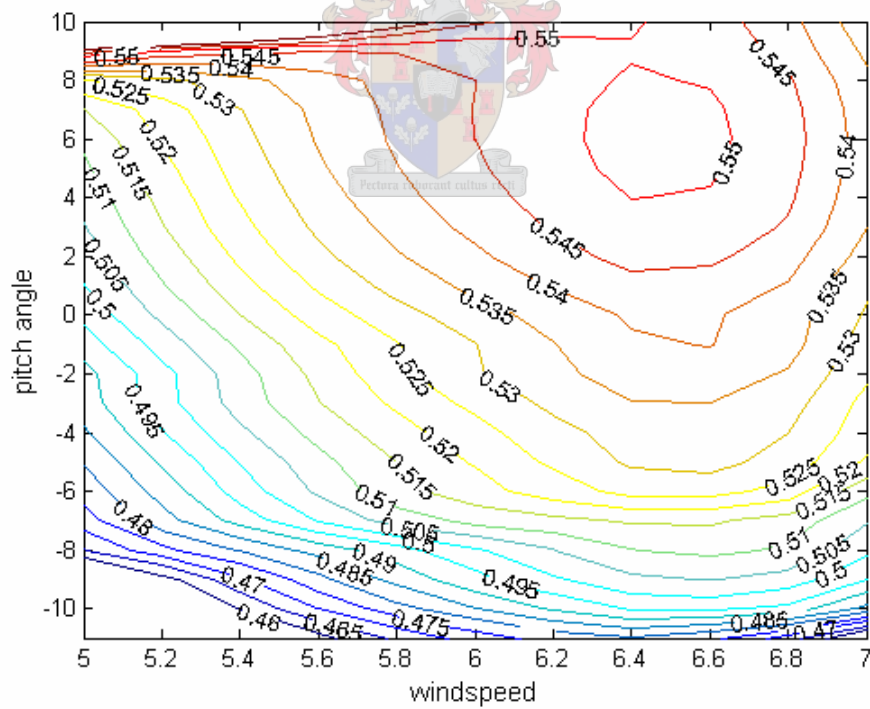


Figure A.5.4.2: Contour plot of C_p values

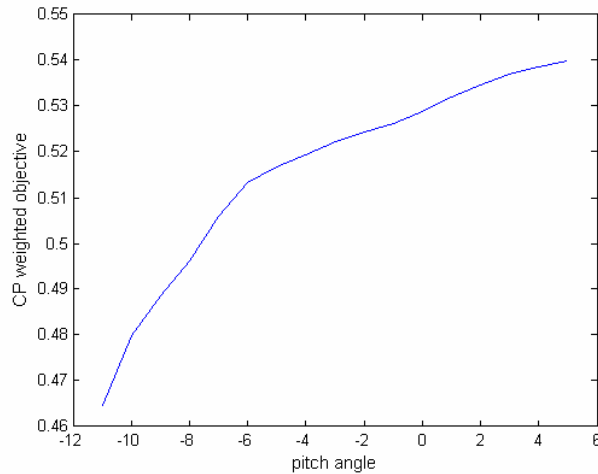


Figure A.5.4.3: The C_p objective function in relation to the pitch angle

A.5.5 Chord length variation

In this design project, the chord length varies exponentially along the length of the blade. The chord is defined by the following function:

$$\text{chord} = a \times \left(\frac{r}{R}\right)^b$$

a controls the magnitude of the chord, whereas b defines the shape along the length of the blade. a and b are the variables used in the optimisation. Figure A.5.5.1 displays the chord distribution for b values ranging from -0.2 to -0.9. Similarly, Figure A.5.5.2 displays the chord distribution for a values. These figures are included to demonstrate chord variability. The chord defines both the length of the profile as well as its thickness. To realistically constrain the optimiser, there are constraints imposed upon these chord lengths. These constraints ensure that the chord is no less than 0.2 m and no greater than 0.8 m. This is confirmed in the figures below.

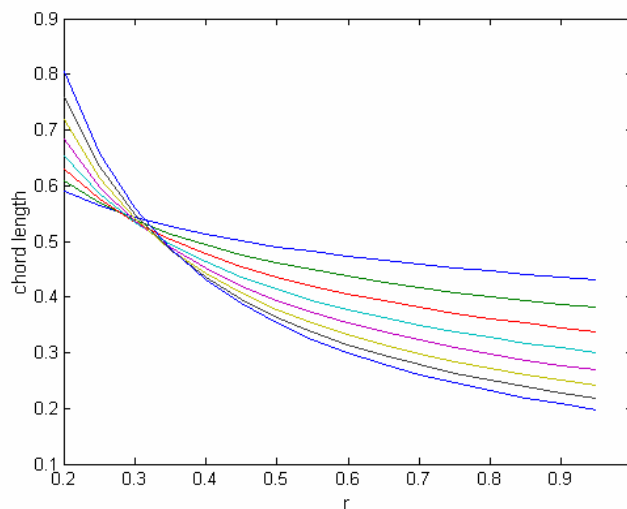


Figure A.5.5.1: Chord distribution for different b values along the length of the blade

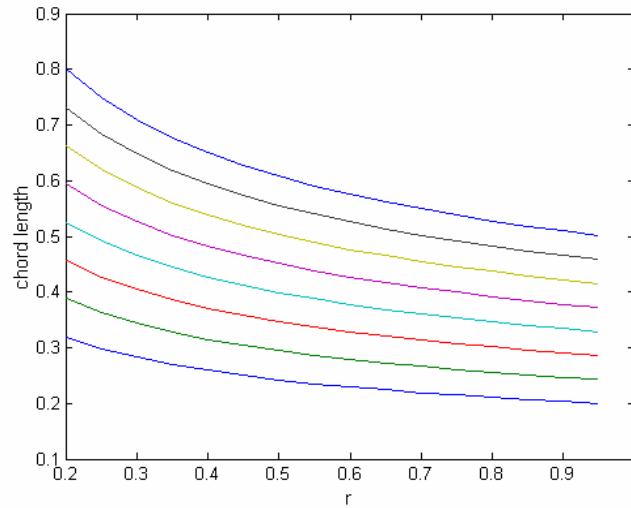


Figure A.5.5.2: Chord distribution for different a values along the length of the blade

Variable b

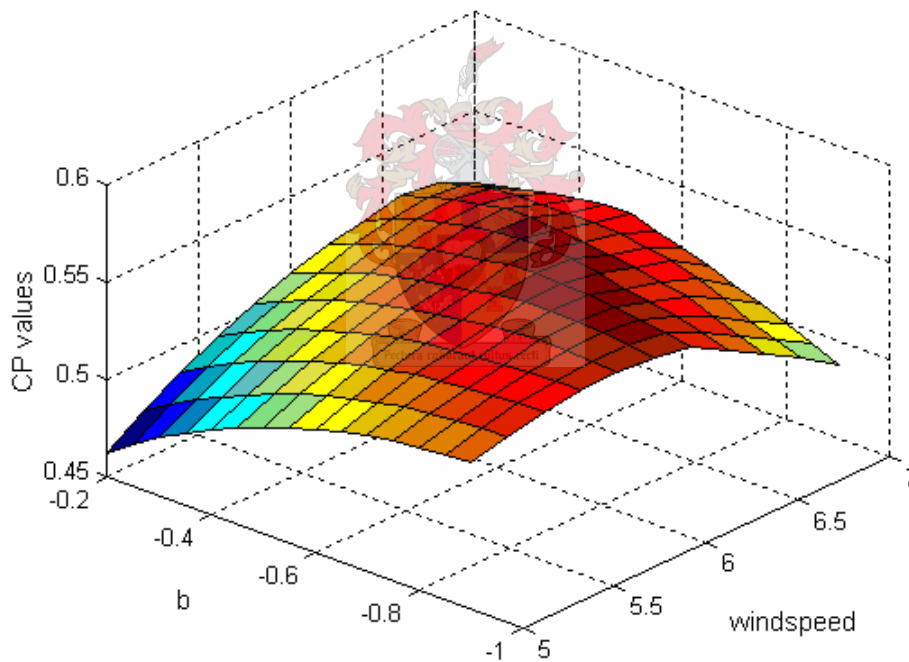


Figure A.5.5.3: Three-dimensional surface plot of C_p versus windspeed and b

Referring to Figures A.5.5.3 and A.5.5.4, as b values increase, the C_p values increase to a maximum. This occurs at a b value of -0.7 and a windspeed of approximately 6.2 m/s. Assuming all other variables constant, varying the b values tends to allow large contour areas of high C_p values. In comparison to when the pitch angles at each station were separately varied, the contour map here is on average much higher. The C_p values are seen to increase in proportion with b .

In Figure A.5.5.5, the C_{Pobj} peaks at a b value of -0.64 . Note that the C_{Pobj} values are higher than those encountered in the previous analyses. The b variable has the ability to increase the overall

performance of the blade considerably. Obviously, the lower values of b are preferred for higher wind rotor performance. Thus, a steeper chord distribution is expected along the blade.

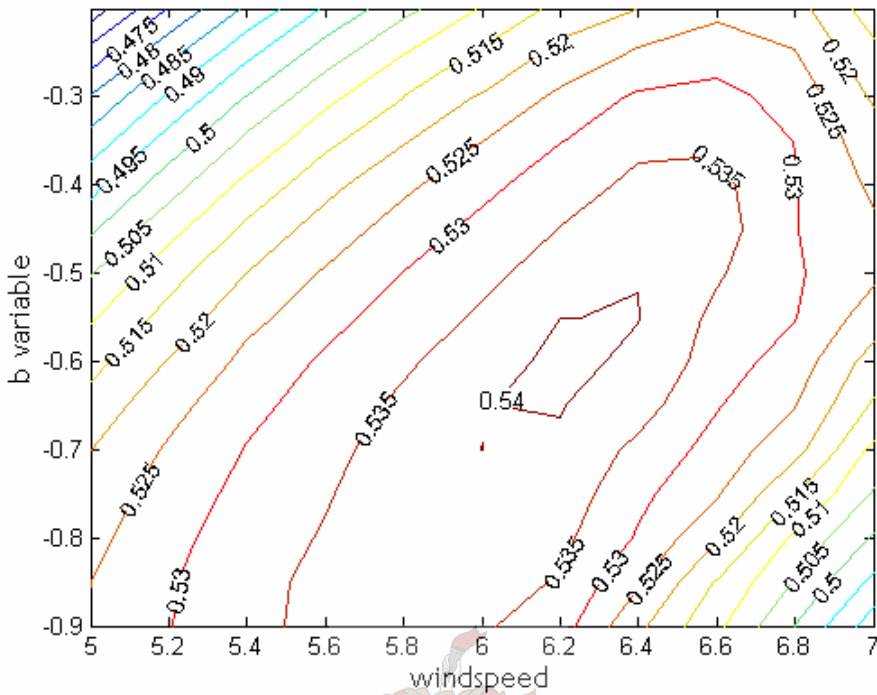


Figure A.5.5.4: Contour plot of C_p values

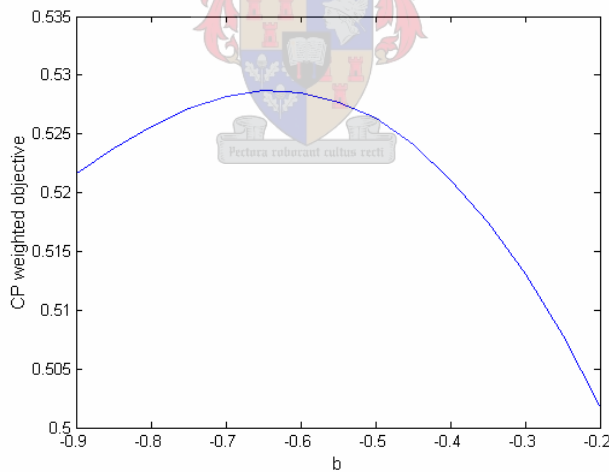


Figure A.5.5.5: The C_p objective function versus b

Variable a

The following graphs represent data composed from different values of a . The form factor b was kept constant at -0.3 which creates a fairly flat chord distribution along the blade (Figure A.5.5.1). Reference to the previous case where only the form factor was varied shows that the peak performance value for -0.3 was 0.53 at a windspeed of 6.6 m/s. Figures A.5.5.6 and A.5.5.7 verify that the C_p value of 0.53 occurs at a windspeed of 6.6 m/s. It is evident that for high and low values of a , the performance of

the blade changes radically with windspeed. For example, the a value of 0.1969 has a C_p of 0.51 at a windspeed of 5 m/s, but this drops to 0.4 at 7 m/s. In Figure A.5.5.8, it is confirmed that the high and low a values produce C_{pobj} values much lower than those obtained using the middle range a values. The peak C_{pobj} values occur in only a small range of a values.

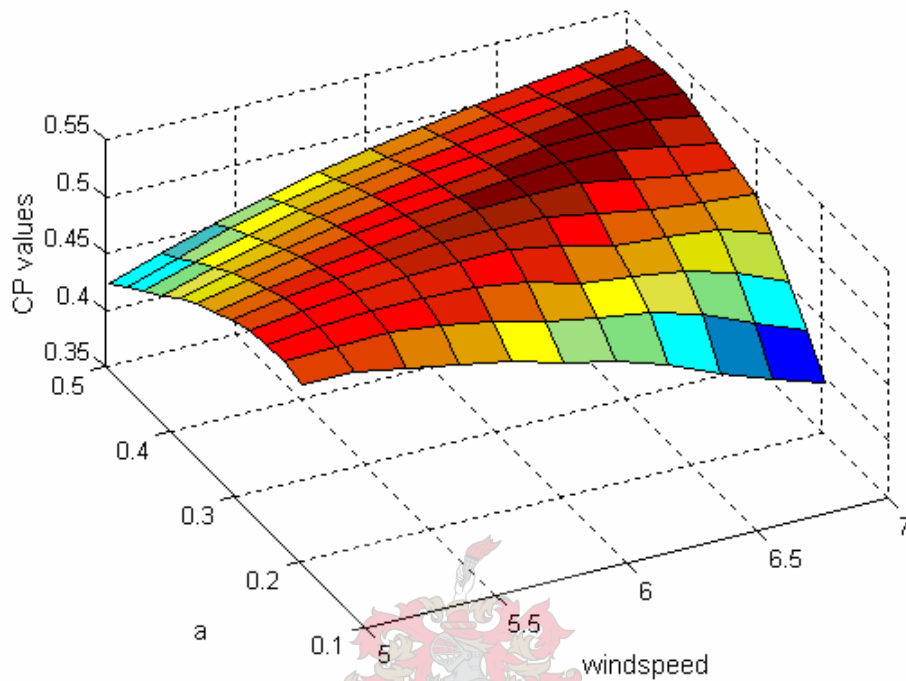


Figure A.5.5.6: Three-dimensional surface plot of C_p versus windspeed and a

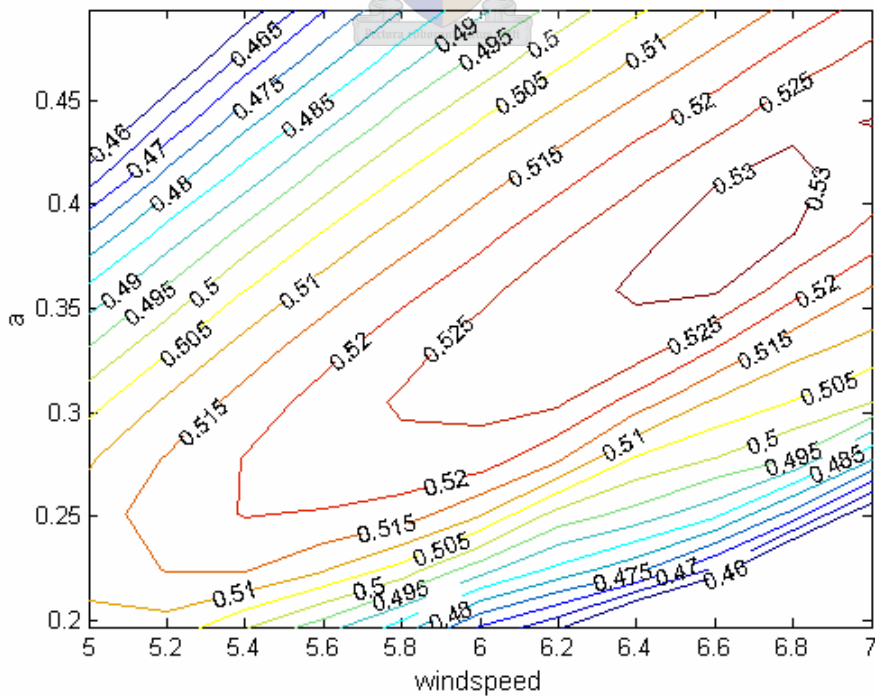


Figure A.5.5.7: Contour plot of C_p values

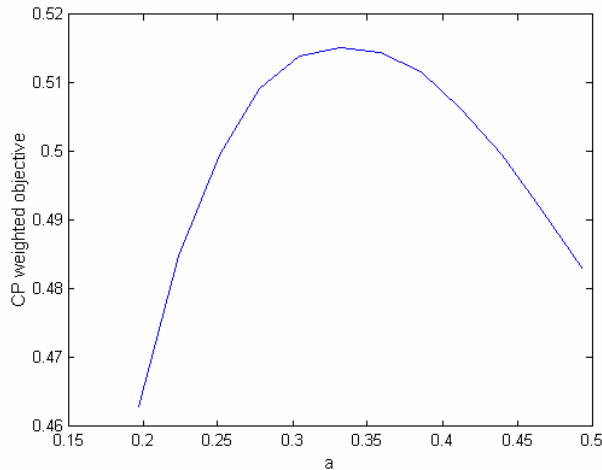


Figure A.5.5.8: The C_p objective function versus a

A.5.6 Discussion of Results

In this chapter, the solution space for the rotor optimisation has been investigated. Each of the six design variables used to describe the rotor was individually varied, while keeping the rest constant. The resultant performance of the wind rotor for the windspeed range was calculated in the form of the C_p and C_{pobj} values. This investigation has given insight into how the rotor performance is affected by a single design variable.

Certain design variables were more influential than others. The pitch angle at the tip station proved to have the most design influence of the pitch angles at the other stations. Even small design variable changes were measured to have a substantial influence on the performance of the blade. The root station pitch angle was the least influential. The rotor performance was on average low, and the response to the design variable changes was sluggish. The mid station allowed better performance response, but nevertheless the optimal area was quite narrow. The pitch angle at the semi station allowed a larger area for good rotor performance, with the C_p values being on average higher than in the case of the mid and root stations. Of course, the tip station pitch angle demonstrated the greatest influence of the pitch angles.

The effect of the chord length design variables a and b were also investigated. Design variable b drives the rotor to values of C_p as high as those obtained in the semi pitch angle analysis. However, the C_{pobj} high performance region is more narrow. Design variable a does not produce particularly high C_p values and the peak C_{pobj} values occur in only a small range of a values.

When single analysis performed varying only one design variable and maintaining the other variables at constants, these constants were chosen arbitrarily. Should all the above analyses be repeated with different constants chosen, the solution space would be slightly different, however the influence of the significant design variable would remain the same. In other words, should the analysis using a variable root station pitch angle be repeated, using different constants for the pitch angles at other stations, the resultant surface plot would show the same trend. However, the optima displayed in the figures are likely

to change. Nevertheless, this study of the solution space allows one to understand the drivers for change considering all the variables in optimisation of the full rotor.

